POLITECNICO DI MILANO
DEPARTMENT OF CHEMISTRY, MATERIALS AND CHEMICAL
ENGINEERING "GIULIO NATTA"
DOCTORAL PROGRAM IN MATERIALS ENGINEERING

VIBRATIONAL AND COMPUTATIONAL INVESTIGATION OF ADSORPTION AND TRIBOLOGY OF ORGANIC FRICTION MODIFIERS INTERACTING WITH STEEL SURFACES

Doctoral Dissertation of:
Nicolò Simone Villa

Supervisor:
Prof. Andrea Lucotti, Lucia Bonoldi (Eni S.p.A)

Tutor:
Prof. Matteo Tommasini

The Chair of the Doctoral Program:
Prof. Chiara Bertarelli

XXXV Cycle

Abstract

Friction plays a major role in contributing to global energy consumption and reducing it would bring about major economic and environmental advantages. Organic friction modifiers (OFMs) are cost-effective and environmentally friendly additives that are included in lubricant packages to improve performance. Their friction-reducing properties are connected to their adsorption state on steel surfaces. This study applies Infrared Reflection Absorption Spectroscopy (IRRAS) to probe the OFM tribofilm on microscopic areas of the sample (micro-IRRAS). The recorded spectra are interpreted by density functional theory (DFT) calculations and provide important information about the effect of the tribological phenomena on the adsorption state and molecular orientation of the friction modifier. The OFM molecules chemisorb on the surface forming monodentate, bridging bidentate, and bridging chelate configurations on the iron atoms, arranged in self-assembled monolayers (SAM). The IRRAS data combined with the DFT models show that under the effect of friction, the molecules tilt towards the steel surface. DFT-MD simulations revealed that the broad bands found in the micro-IRRAS spectra are caused by the molecular disorder occurring due to temperature. Energy calculations from the DFT models were combined with classical Molecular Dynamics (MD) to reveal that a strong packing of the OFM molecules is crucial in governing friction performances, as well as the temperature range of effectiveness of the friction modifiers, which is determined by the temperature at which the Gibbs' free energy of packing of the SAM is negative. Finally, the MD models revealed how the mechanism by which OFMs reduce friction includes collective tor-

sional motions of the alkyl chains, which are enabled by the strong packed state of the monolayer. This study enlightens the principles of the action of OFMs in reducing friction and provides guidelines for the development of new OFMs exhibiting better performances. The results obtained pave the way for a software-assisted design of new OFMs, as well as the development of machine learning models for the prediction of friction performances, with the knowledge of the OFM structure as the only requirement.

Summary

Environmental and Economic considerations have been brought by a plethora of different regulations and different approaches in the development and research of new products. This is especially true in the automotive field, where emissions of a multitude of materials that are toxic to the environment must be limited. Focusing on the automotive industry, many changes have been done to prevent hazardous emissions which range from the filtering of exhaust gases to the reduction of the fuel consumption of the vehicle itself. The latter, not only reduces the level of toxic emission of the vehicle but also hugely impacts the whole natural resources industry.

One action that can be taken to reduce the energy consumption of the vehicle is to limit the energy loss induced by tribological phenomena. This is the focus of an immense slice of research in the automotive industry, where most of the efforts are directed toward the development of high-performance lubricants. A lubricant is in itself composed of a package of additives introduced in a base oil. The additive package aims at increasing the lubricant performance, extending the engine lifespan, and reducing the energy loss caused by the tribological phenomena, in compliance with the latest environmental requirements.

Friction modifiers are one key additive present in lubricant formulations, as it is its job to reduce the friction coefficient between the sliding part of the engine in tribological contact. At the same time, the friction modifier mustn't contain toxic compounds that can be released into the environment or compounds that can severely damage the structure of the engine. Organic friction modifiers seem to respond very well to these demands, there-

fore they are nowadays at the center of lubricant research across the whole automotive industry. It is key to understand how these friction modifier act to reduce friction, however, although recent research has already put a lot of effort into this topic, there are still questions to answer about the adsorption mechanisms and the link between the molecular structure of the organic friction modifier and the performances of the resulting lubricant.

Computational Chemistry appears to be a suitable tool to study the molecular structures, adsorption geometry, and adsorption energies of friction modifiers adsorbed on steel surfaces, as well as providing interpretational aid to the experimental techniques that start to show limitations at such a small scale, such as IRRAS - Infrared Reflection Absorption Spectroscopy, which is a remarkably useful tool to probe the adsorption state of molecules on surfaces and to understand their adsorption chemistry but presents the difficulty of interpreting its results. Molecular Dynamics, on the other side, is a well-established tool to gain insights into the evolution of dynamic systems, providing answers to the molecular behavior of organic friction modifiers under tribological conditions.

This Ph.D. collaboration is a joint effort between the Eni S.p.A DOWN-STREAM group, The Department of chemistry, materials, and chemical engineering Giulio Natta of Politecnico di Milano, and the Theoretical Chemistry group of the IMM - Institute for molecules and materials of Radboud University. The aim of this collaboration, which culminated in this work was to combine computational and experimental work to further increment the understanding of the adsorption of organic friction modifiers on the steel surface and understand what is the underlying reason for their friction reduction performances, providing precious insights for faster development of powerful lubricants. The specific areas of expertise of each collaborating group were fundamental to reaching this aim. The present work was divided into three steps: Firstly, the spectroscopic study of organic friction modifiers adsorption and tribological investigations were carried out in the laboratories of the Eni S.p.A DOWNSTREAM group. Secondly, the density functional theory models were performed in Politecnico di Milano. Finally, the molecular dynamics and DFT-MD models were performed at Radboud University, which required a visiting stay of 6 months. The large size of the computational work also required HPC (High-Performance-Computing) resources at both the Cineca and Snellius supercomputers.

The present work is divided into seven chapters:

- The **first chapter** focuses on reviewing the recent literature regarding tribological phenomena in the automotive industry, as well as provid-

ing a general picture of modern lubricant composition, to then focus on the recent advances in the understanding of the working mechanisms of organic friction modifiers discussing both experimental and computational tools.

- The **second chapter** lays down the foundation of the present work. All the materials and experimental and computational techniques will be explained in specific detail how they have been employed for this work.

- The **third chapter** focuses on the IRRAS investigation of friction modifiers adsorbed on steel surface, and on the validation of this technique as a suitable tool to probe competition phenomena occurring in complex lubricant formulations

- The **fourth chapter** takes in the information brought by the IRRAS experimental work and interprets the results via DFT and DFT-MD models to understand the adsorption mechanism of organic friction modifiers. Moreover, the approach described in this chapter will also be exploited to understand the adsorption state of the organic friction modifier after the tribological phenomena occur.

- The **fifth chapter** further deepens the computational investigation of organic friction modifiers' adsorption and tribological behavior, analyzing in depth the link between adsorption properties of organic friction modifiers and tribological friction coefficient performances.

- The **sixth chapter** shows the results of molecular dynamics simulations in light of the findings of the previous chapters.

- The **seventh chapter** summarizes the most critical results of the thesis and proposes a behavior model for organic friction modifiers, as well as using the results to provide insights and directions on future development.

Contents

Contents

Current Understanding of Lubrication

Lubricants are very important in any industrial sector and are especially widely employed in the automotive industry. Friction is one of the main causes of energy waste worldwide, from industrial processes to common household appliances. Saving this energy - besides constituting a great economic relief for the end users - would have a significant impact on the environment. In relatively recent literature, It has been accounted that around 23% of the global energy consumption is wasted from overcoming tribological phenomena, highlighting the energetic relevance of friction beyond the automotive industry. Moreover, it has been estimated that research efforts in the science of lubrication could significantly impact the economy, with long-term (15 years) cost savings amounting to 1.4% of the GDP annually, and a total reduction of costs of $\sim$ 55%, 40%, 25%, and 20% in the trasportation, power generation, manifacturing and residential sectors, respectively [1] This issue cannot be overlooked, and it shows the widespread impact of lubricant research, which currently is an important branch in tribology studies. [2] Nowadays, lubricants are comprised of a mix of additives that are used for a diverse range of purposes. [3–7] Among this plethora of additives, friction modifiers are substances that interact with the surfaces of the mechanical pieces that are in tribological contact, and

considerably reduce the friction coefficient of the sliding contacts. In the case of this study, the behavior of friction modifiers for the specific case of the automotive industry are investigated. Hence, before discussing the details of the research, it is worth providing a brief introduction to specific and collateral topics.

1.1 Lubrication Phenomena in Automotive Engines

For what concerns the inner working of an automotive vehicle, surely the most important point to take into account is the tribological phenomena that occur in a thermal engine (or any kind of engine system that revolves around the sliding of mechanical parts in contact with each other). The most sensitive part of an engine to tribological issues are the pistons. These are the mechanical parts that ultimately allow vehicles to move, and a significant amount of energy can be wasted here due to friction. Moreover, friction can cause the parts to deteriorate and fail. However, friction is not a simple quantity and grasping its behavior may be challenging. In the specific case of lubrication by liquid-based lubricants, friction greatly depends on a large set of variables. As in any phenomenon that involves liquids, there are regimes in which a different phenomenology characterizes the resulting friction coefficient. The onset of different regimes depends on a quantity, called Hersey's number [8]:

$$H = \frac{\eta v}{P} \tag{1.1}$$

Where η is the dynamic viscosity of the lubricant, v is the speed at which the lubricant is entering the interface of the sliding part, and P are the normal pressure per length on the tribological contact. As ideally the viscosity of the lubricant and the load on the tribological contact can be supposed constant on purposefully designed lubricants and engines. Four main regimes are distinguished at varying values of the speed v (Fig. 1.1).

- Boundary Lubrication;

- Mixed Lubrication;

- Elasto-Hydrodynamic Lubrication (EHL);

- Hydrodynamic Lubrication (HL).

EHL and HL regimes are characterized by the presence of a thick layer of lubricant that prevents the sliding surfaces from coming into contact. Here,
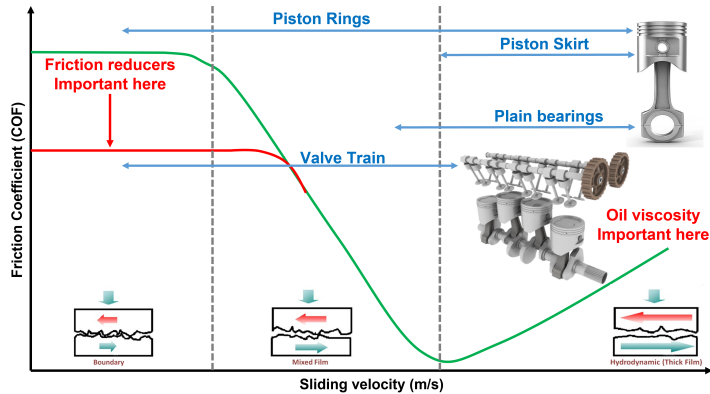
Figure 1.1: *Stribeck friction coefficient curve and the lubrication regimes occurring in liquid lubrication.*

the determination of the friction coefficient follows common hydrodynamic laws and is ultimately dependent on the viscosity of the lubricant. [9, 10] In boundary lubrication regimes, the two surfaces can come into contact through asperities since the thickness of the lubricant layer is not sufficient to prevent it. Therefore, the load is supported by the contact points between the asperities. [11] In the mixed lubrication regime, the thickness of the lubricant layer is slightly increased, preventing some of the asperities - but not all - to come into contact. [12] Here the load is supported both by the contacts and the lubricant layer. In both boundary and mixed lubrication, hydrodynamic laws do not work, and here is where lubricant additives really come into play. In this regime, which can be unified and called Boundary-Mixed lubrication (BML), the friction coefficient depends on the type of materials in contact and on the chemical formulation of the lubricant (i.e. the composition of the base oil and the additives in it included). Although friction modifiers can indeed play a role in the EL and EHL regimes, for example in cases where the lubricant viscosity is low enough that the film thickness becomes very low allowing for some contact between the surfaces (although here we would fall again into the BML regime), their intended action is majorly observable in the BML regime. Therefore, the investigation will be focused on this regime.

1.2 Automotive Lubricant Formulations

Automotive lubricant formulations are very complex. Their functions mainly reside in the reduction of wear on the mechanical parts, the reduction of

friction, and the maintenance of a clean interface between the moving parts. Generally, a lubricant formulation is composed of around 70-80 % of the base lubricant, 4-15 % of viscosity modifiers, pour-point depressants, corrosion inhibitors, and extreme-Pressure Additives, and the remaining 3-20 % is composed of the additive package. The additive package itself is composed of roughly 50 % dispersants, 0.5-1 % by friction modifiers, and the remaining is composed of anti-oxidants, anti-wear, and detergents (ranges provided by Eni S.p.A). A detailed account of each component of the lu-

TOTAL LUBRICANT FORMULATION
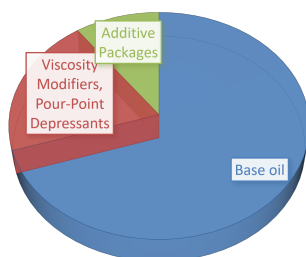
ADDITIVE PACKAGE
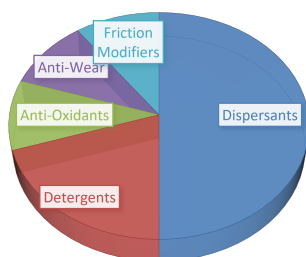
Figure 1.2: *Section of a thermal engine for automotive vehicles (ranges provided by Eni S.p.A).*

bricant can be found in the literature and on which our understanding of lubricant formulations relies. [3–6] Here, only a brief description of the main aspects of each component will be provided:

Base Oil

The base oil has the main functions of maintaining a film of lubricant during the operations of the mechanical parts and being stable under the thermal solicitation. This translates into specific viscosity and heat capacity characteristics. Besides this, the base oil is the matrix in which all the additives are embedded. Therefore, it has to be chosen so that the additives are sol-

uble in it. [6, 8] The main Base Oils used in the automotive industry are commonly belonging to two categories [5]:

- Mineral oils;

- Synthetic oils.

Mineral oils are produced during the refinement process of petroleum crude oil, these are long-hydrocarbons, mainly paraffines, naphthenic oils, and aromatic oils. [13] The American Petroleum Institute (API) divides these oils into three classes depending on viscosity, saturation, and sulfur concentration. Synthetic oils on the other side of the spectrum, are chemically synthesized as mineral oil substitutes, and as such allow a greater degree of freedom in their design to achieve specific properties. The API divides them into two categories: Poly-α-olefins (PAO) and in the second category all other types - commonly silicon derivates and organohalogens.

Viscosity Modifiers, Pour-Point depressants, Corrosion Inhibitors, and Extreme-Pressure Additives

Extreme-pressure additives are used to aid in the context of boundary lubrication. Their function is to react to the surface to prevent wear due to the adhesion of the sliding surfaces. Extreme-pressure additives are Organosulfur and organo-phosphorus compounds, such as organic polysulfides, phosphates, dithiophosphates, and dithiocarbamates. [6] Corrosion inhibitors protect the surface from deterioration due to corrosive reactions with oxygen, water, acids, bases, and salts in the environment. Common corrosion inhibitors are chemical species that include organic compounds containing nitrogen, boron, sulfur, and phosphorus atoms. [6] Viscosity modifiers are added to modify the overall viscosity of the base oil. Common acids include alkylbenzene sulfonic acids, alkylphenols, and fatty carboxylic acids. [6,14] Pour-point depressant additives aim at tuning the temperature at which the lubricant can flow as a liquid, preventing the formation of crystalline networks and allowing oil to flow at low temperatures. Common pour-point depressants include wax-alkylated naphthalenes and phenols, polymethacrylates, and styrene-ester copolymers. [6]

Dispersants, Detergents, Anti-oxidants, and Anti-wears

Detergents and dispersants, together with anti-oxidants, belong to a particular portion of a lubricant package called stabilizers or deposit control

agents. Their main goal is to prevent the deposit on the surface of unwanted entities and keep them suspended in the lubricant layer. Deposit precursors such as hydroperoxides and radicals are extremely detrimental to the maintenance of a good lubrication layer as they can attack the hydrocarbon-based oil and additives, forming sludges, resins, and hard deposits. [3, 4] Anti-oxidants reduce the formation of deposit precursors, and prevent the degradation of the base oil by oxidation. Common antioxidants include oil-soluble organic and organometallic antioxidants such as sulfur compounds, phosphorus derivatives, aromatic amine compounds, phenol derivatives, organo-copper compounds, and boron derivatives. [15–18] Detergents and dispersants keep the deposit precursors suspended in the base oil, and carry them away from the tribological contact. Common detergents possess a micellar structure made of an alkaline core surrounded by surfactant chains. [19] Recently, detergents made by calixarenates have been introduced. [20] Common dispersants are organic compounds with a polar head and a hydrophobic tail. [19] Succinimides such as PIBSI (polyisobutylene succinimide) are the most used. Anti-wear additives are mixed in the lubricant formulation with the purpose of reducing the amount of material scraped from the lubricated metal due to the tribological contacts by forming a protective layer on the surface of the steel. The main anti-wear agents employed in lubricants are ZnDTPs (zinc-dithiophosphates) and MoDTCs (molybdenum-dithiocarbamates). [6]

Friction Modifiers

In the EHL and EL lubrication regimes friction can be reduced simply by lowering the viscosity of the lubricant being careful to guarantee a good enough lubricant stability so that the regime is maintained. However, to reduce friction in the boundary-mixed regime, friction modifiers are added in lubricant formulations. [2] Among the several types of friction modifiers, there are four types that gained the most success and are of common use nowadays:

- Organo-molybdenum compounds;

- Functionalized polymers;

- Dispersed nanoparticles;

- Organic friction modifiers.

Organic friction modifiers are today one of the most used additives in lubricant manufacturing, due to their reduced environmental impact, low cost, as

well as ease of manufacture. [2,21] They are the object of this study and will be described in more depth in the next section. Organo-molybdenum compounds, such as MoDTCs and MoDTPs (molybdenum-dithiophosphates), before becoming more widely used as friction modifiers agents, were initially proposed as strictly anti-wear agents. However, it has been found that they do provide friction reduction properties as well and found success as friction modifiers. Functionalized polymers have been widely used as viscosity modifiers. As they can be tailored to attach on specific sites of polar surfaces, guaranteeing stable adsorption, they have been a point of focus of research as friction modifier additives. However, their large molecular weight (i.e., size) makes it problematic to form densely packed layers on surfaces. Colloidal dispersed nanoparticles have recently been captivating interest in research, as there are several advantages that would make them favorable with respect to all other types of friction modifiers [2]:

- Can be dispersed in lubricants although being insoluble in non-polar lubricants;

- Mechanical film formation, which allows them to avoid requiring strong reactive chemistry, plus being able to form layers on a wide array of surfaces;

- Less interactive with the other components of the lubricants;

- High-temperature resistance.

1.3 Organic Friction Modifiers (OFMs)

Organic Friction Modifiers were first introduced in the early 1900s, when it was observed that fatty acids, contrarily to the belief that only the viscosity of the lubricant was the main actor in determining friction reduction [9], could reduce friction beyond what predicted only by the viscosity of the lubricant. [2] This phenomenon of further friction reduction was ascribed to "oiliness" back in the early days of the observation of this phenomenon. [22] It was soon after described by Langmuir that fatty acids can deposit as monolayers on glass surfaces reducing friction and Hardy demonstrated the relationship between increasing chain length and friction reduction, leading to the proposition that fatty acids reduce friction by forming monolayers of vertically oriented molecules, introducing the concept of boundary lubrication, and starting the field of research in Organic Friction Modifiers. [23,24] Organic Friction Modifiers are amphiphilic molecules, constituted by a polar head and an alkyl chain, terminated by a non-polar group (or tail - in

almost all cases this is the CH_3 group that terminates the alkyl chain). In general, OFMs are mainly carboxylic acids, amides, amines, imides, glycerides, and their derivatives. At the current state of the art, the general understanding is that OFMs form dense, vertically oriented self-assembled monolayers (SAMs) on the surface of steels, which are supported by Van der Waals interactions among the molecules in the film, which prevents direct metal-metal contacts, therefore facilitating the sliding of the mechanical parts separated by the lubricant film and reducing friction. [25, 26] This interpretation has been supported thoroughly through experimental techniques such as X-ray Photoelectron Spectroscopy (XPS), Atomic Force Spectroscopy (AFM), ellipsometry, Surface-Force Apparatus (SFA), Sum Frequency Generation (SFG), and Quartz Crystal Microbalance. [27–33] However, the understanding of the behavior of OFMs shows some dark spots. For example, it is not yet clear how adsorption is achieved on the surface, whether by physisorption or by chemisorption. This is reflected in the fact that although it has been observed that OFMs do show a temperature limit above which the friction reduction properties decrease, different interpretations are suggested for each adsorption modality. For physisorption, it has been proposed that the temperature limit of OFMs corresponds to the desorption temperature, whereas if chemisorption occurs, this has been proposed as the melting point of the soap formed on the surface. [34, 35] Moreover, although different OFMs show different friction coefficients, it is not yet clear where this difference in behavior comes from. A study by Koshima et al. [36], tried to identify molecular descriptors of a variety of OFMs that would allow producing a relationship between friction reduction and specific molecular characteristics in a QSPR (Quantitative Structure-Property Relationship) approach. This hinted at describing friction reduction acted by OFMs as a result of a mix of factors such as adsorption, electronic, and geometrical properties of the molecules.

Self-assembled monolayers of OFMs have been extensively studied experimentally. The insights collected generally regard film thickness, friction coefficient, parameters such as the length of the OFM chain, the saturation degree, humidity, and the effect of different surfaces such as steel and DLC (diamond-like carbon). However, little progress has been achieved in revealing the type of adsorption of OFMs. Recently though, the use of vibrational spectroscopy (IR and Raman) started to reveal this type of interaction. It has been suggested by PM-IRRAS (Polarization modulation-infrared reflection-adsorption spectroscopy) for example, that fatty carboxylic acids do adsorb on the surface through the formation of carboxylate that interacts with the polar sites of the surface. [34] Although some information

about the state of the adsorption before and after the application of the mechanical stress could be inferred, the main experimental difficulty that hinders OFM adsorption investigations during and post friction tests is the very small size of the sample area affected by the mechanical stress in most tribological instrumentations compared with the sample area measured by typical IRRAS instrumentation. This makes it unfeasible for the current IRRAS equipment to provide information only from the region which was affected by the mechanical stress during the tribological tests. [37] Nevertheless, IRRAS is an infrared technique widely used for the analysis of thin films [34, 38–41], which is possible thanks to the grazing angle detection configuration. Remarkably, IRRAS is selective with respect to those vibrational modes associated with transition dipoles that are oriented perpendicularly with respect to the surface: the modes which imply a variation of the electric dipole moment perpendicular to the surface will be more intense in the spectrum. This feature of IRRAS makes it appropriate also for analyzing the orientation of molecules adsorbed on surfaces. [42, 43] Another main challenge of experimental investigations on OFM films, in general, is the study of the behavior of the films in situ, during the tribological test. In this case, vibrational spectroscopy with IR and Raman spectroscopy has shown promising results due to its potential applicability in this setting. In this frame, however, the bulk of the lubricant, represents the biggest challenge, as it can completely hide the signal of the friction modifier, making it extremely difficult to get information coming from the friction modifier only. [44–48]

In recent years, to tackle specifically the aspects of OFMs adsorption and in situ investigation of OFMs behavior during tribological stress computational techniques found rising application. Specifically, ab-initio quantum mechanical calculations and classical Molecular Dynamics are powerful tools for investigating adsorption processes and dynamic behavior under tribological stress, respectively. [49, 50] Molecular Dynamics studies have provided a great number of insights on the dynamic behavior of OFM films adsorbed on surfaces on tribological contacts. [51–53] The alkyl chains of OFMs were found to tilt in the direction of the friction force due to contact sliding. [52] Also, the coverage seems to affect the structure of the tribofilm and the predicted friction performances. [54, 55] Longer alkyl chains were also found to result in lower friction coefficients. [56] A benchmark study has also demonstrated that AA (all-atom) force fields are crucial in order to correctly predict the flow and friction behavior of OFMs on steel. [57] One of the main challenging aspects of the use of classical MD models is the description of the chemical reactivity with the solid surface. Classical

MD simulations rely on the use of empirical force fields which generally do not take into account reactivity. [50] However, the introduction of reaxFF force-field might in the future allow investigation of this aspect. [58] Nevertheless, ab-initio methods can come into play here. Ab-initio density functional theory has seen extensive use for the investigation of problems in a variety of fields, and only recently has its use been extended to the study of lubricants on solid surfaces. Less computationally demanding tools such as Tight Binding calculations have been performed on the theme of the adsorption of carboxylic acids on iron oxides, corroborating the idea that carboxylic acids do chemisorb on the surface, no matter the length of the alkyl chain. [59] However if the surface is composed of iron hydroxide, they are mostly physisorbed. [59, 60] Moreover, the adsorption of model friction modifiers such as hexanoic acid, hexanoic amide, and glycerol mono hexanoate has been investigated by Density Functional Theory, focusing on the effect of coverage on their adsorption state. [61] However, Density Functional Theory allows for the calculation of vibrational IR and Raman spectra of these species in their adsorbed state and consequently provides a direct tool for interpreting experimental results. To the best of the author's knowledge, this approach has not been attempted in this specific case yet.

To conclude, the aim of this work is to combine infrared spectroscopy and computational techniques (DFT and Molecular Dynamics) to provide answers to the unsolved questions that do not find an answer yet in the literature. Specifically, our goal is to understand how OFMs adsorb on the surface of steel, providing a definite answer using spectroscopic evidence, through the interpretation of DFT calculated infrared spectra. At the same time, we aim at understanding the processes at the microscopic level that occur during tribological processes on SAMs made by OFMs through combining DFT calculations and molecular dynamics simulations, with the intent of gaining important insights about the characteristics of OFMs that determine the resulting friction coefficient and tribological properties.

CHAPTER *2*

Materials and Methods

2.1 Materials

Lubricant packages comprise a wide variety of additives embedded in a base lubricant oil. In our study, squalane (Chemical structure provided in Fig. 2.1) was used as the base oil. Squalane is the hydrogenated derivative of squalene. Due to its properties, it is used as a common reference model for the base oil in tribology applications. ETROIV (Petronas Lubricants) is a commercial base oil product. It is a heavy hydrotreated paraffinic distillate, and as such, it is a complex mixture of hydrocarbons, with traces of aromatic components. In this study, 3 model OFMs were taken into consideration, plus 2 other OFMs, one being a commercial product under the name XTJ785, and one which has been developed at the UPSTREAM lab at Eni S.p.A., which is named PC21. The three model friction modifiers are:

- Oleic acid (OA);

- Oleic amide (OAm);

- Glycerol monooleate (GMO).

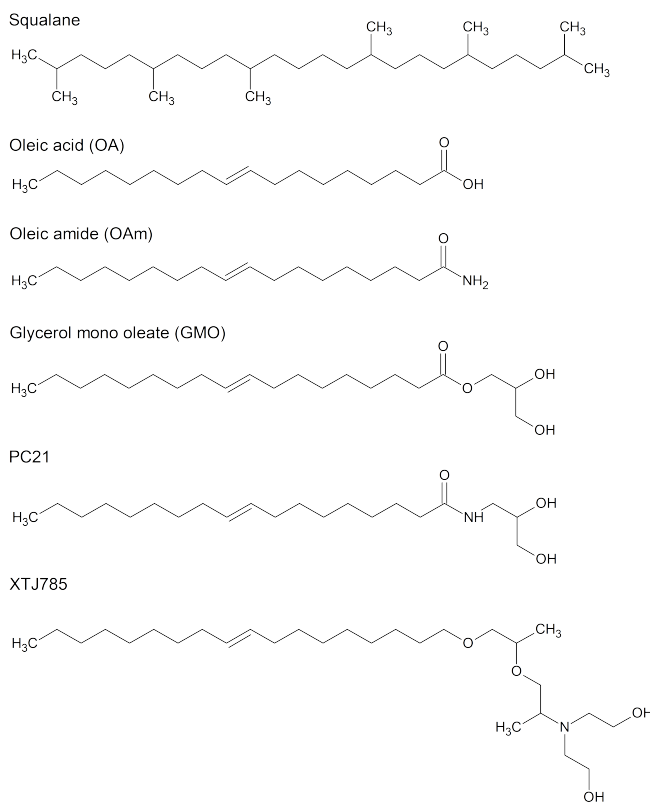The structures of all these OFMs are depicted in Fig 2.1. The other ad-

Figure 2.1: *Chemical structures of the base reference oil squalane and the OFM molecules investigated in this study.*

ditives that found application in this study, are those present in lubricant formulations that show some kind of affinity on the surface of the steel, competing with the OFMs in the adsorption. BB22 is an anti-wear that belongs to the family of Zinc di-thiophosphates (ZNDTPs) (structure in Fig. 2.3). This compound acts by depositing a protective layer of phosphate on the surface of the metal, which aids in reducing wear. Detergents and dispersants also compete at the surface forming deposits. The detergent used in the formulations investigated, (named here XCA03 - Fig. 2.2), possesses a core composed of calcium carbonate, which tends to deposit on the surface. As for the dispersants, here we used two dispersant additives, PIBSI XD23, and XD18. The numbers 23,18 represent the molecular weight of the PIB section of the molecule (Fig. 2.3).
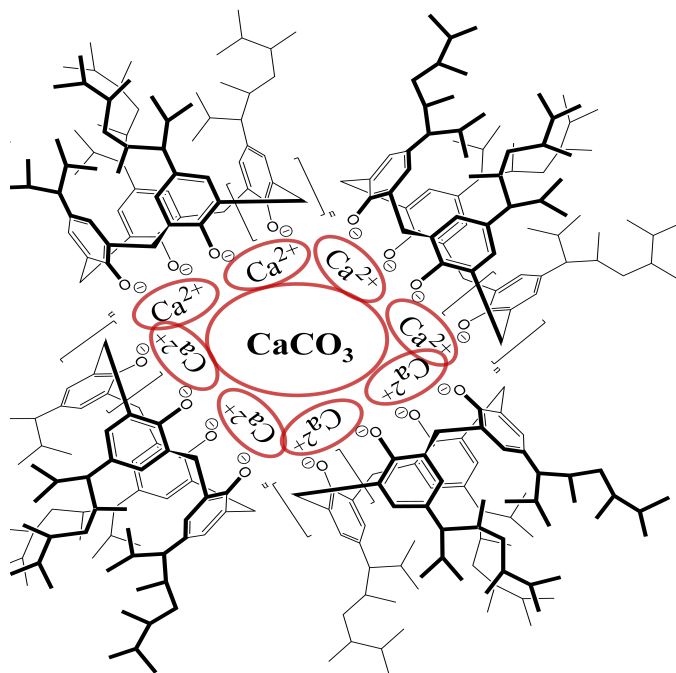
Figure 2.2: *Chemical structure of the calixarene molecule (XCA03) investigated in this study.*
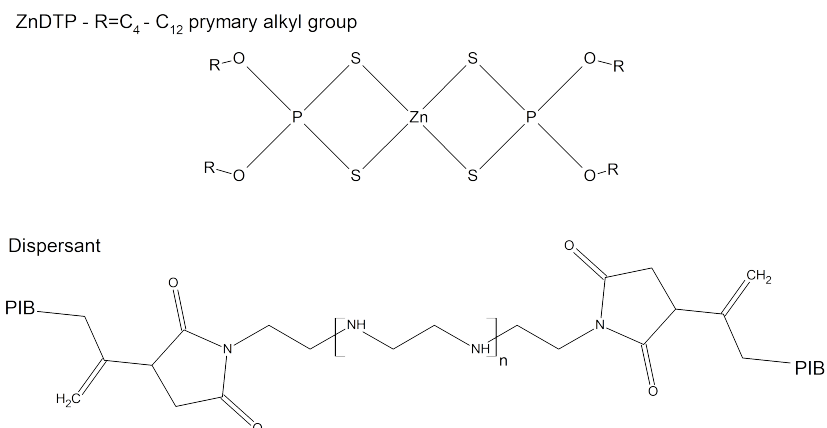

Figure 2.3: *Chemical structures of the Anti-wear (ZnDTP - BB22) and the Dispersants investigated in this study.*

2.1.1 Preparation of Lubricant Packages for Tribological and Spectroscopical Characterization

The organic friction modifiers described above need to be embedded into the lubricant base oil in order to be used for tribological and spectroscopic characterization. The lubricant mixtures used vary in complexity as more additives are added to the mix:

- Binary: Base oil + FM;

- Ternary: Base oil + FM + another additive;

The binary mixtures were used for tribological and spectroscopic characterization in order to study the adsorption states of the OFM molecules and use the computational techniques to find a structure-property correlation that would give insight into the mechanisms by which OFMs reduce friction. The tertiary mixtures were employed to investigate the competition phenomena occurring at the surface among different additives that adsorb on steel surfaces.

2.2 Tribological Characterization

Tribological characterization regarded the measurement of the Stribeck friction coefficients (SFC[1]) of metallic samples immersed in the lubricant mixtures. An AISI52100 steel mini-traction machine (MTM) sample (Fig. 2.4) is sent for tribological friction coefficient measurement on a PCS instruments MTM tribometer. The instrument mounts a chamber in which the lubricant mix is contained. A ball of the same material as the MTM sample is immersed in the lubricant mix and fixed on a rotating axis. The ball is then put in contact with the MTM sample. The instrument is then turned on and the measurement starts. The friction coefficient was measured at three temperatures: 45, 120, and 150 °C. This is a standardized procedure used to produce a tribofilm for spectroscopic analysis which is consistent with the testing protocols carried out at ENI and representative of the working conditions of the lubricant oil inside a motor engine.

The content of OFM and other additives in the lubricant oil is crucial for the results of the tribological and spectroscopic characterization and it was carefully tuned in the Eni laboratories to represent the actual composition that would be present in a commercial lubricant mixture. In the case of Binary mixtures, the concentration of the OFM was set at 1% wt. Regarding

---

[1]SFC: Stribeck Friction Coefficient

Figure 2.4: *Picture of the AISI52100 standard MTM sample.*

ternary and quaternary mixtures, their content is described in Table 2.1. Before spectroscopic analysis, the samples are washed with n-heptane to remove any trace of the base oil. This is a procedure already proven to be effective in literature. [34]

Table 2.1: *Lubricant mixtures investigated by tribological and spectroscopic characterization*

Mixture name	Type	Composition (remaining % wt ETROIV)
MIX 1	Ternary	1% OA -1% BB22
MIX 3	Ternary	1% PC21 - 1% BB22
MIX 4	Ternary	1% OA - 1% PC21
MIX 5	Ternary	1% OA - 1% XCA03
MIX 6	Ternary	1% PC21 - 1% XCA03
MIX 7	Ternary	0.5% PC21 - 6% XD23
MIX 8	Ternary	0.5% PC21 - 5.13% XD18
MIX 9	Ternary	0.5% XTJ785 - 6% XD23
MIX 10	Ternary	0.5% XTJ785 - 5.13% XD18

2.3 Micro-Infrared Reflection Adsorption Spectroscopy (micro-IRRAS)

Infrared Reflection-adsorption spectroscopy (IRRAS) is a widely used technique for the investigation of thin films on metallic surfaces. Like Fourier Transform Infrared Spectroscopy (FT-IR), this technique is non-destructive and allows to gain relevant information about the chemical, structural and conformational configuration of a sample in the form of a spectrum in

which each peak corresponds to a molecular vibration, enabling the identification of specific chemical groups. [62] However, even with all the qualities of FT-IR spectroscopy, this technique has detection and sensitivity issues when the thickness of the sample is lower than 500 Å. IRRAS uses a grazing angle IR radiation to bounce off metallic surfaces (the reflectivity of a metallic surface is necessary) to penetrate a thin film for a much longer path length compared with $90°$ incidence techniques. Traditionally, IRRAS is a macroscopic measurement. In fact, the size of the infrared radiation spot during an IRRAS measurement is usually in the order of 10-100 mm^2. Therefore, this methodology is not suited for surface analysis of OFM tribofilms, because the currently used instrumentation for the tribological testing of friction coefficient, such as mini-traction machines (which is also what was used in this study for the tribological characterization), produces wear tracks with a width of the order of $\approx 200 \mu m$. In this study, a Bruker Hyperion Spectrometer mounting a micro-GIR (Grazing Incidence IR) objective was used. The micro-GIR objective (Fig. 2.5a) can perform IRRAS measurements, using a set of mirror lenses to obtain a grazing-angle reflection on a microscopic scale (the working scheme of the apparatus is given in Fig 2.5b). The wear track can be optically inspected also by the microscope objective of the IRRAS equipment, which allows recording the micrographs of the sampled surface, as the one reported in Fig. 2.6. The maximum size of the area probed by the IRRAS measurement is $\approx 160 \mu m \times 160 \mu m$, which is well inside the width of the wear track etched on the MTM sample during the tribological measurements (Figure 2.6). In the micro configuration, the disturbance from H_2O and CO_2 signals is much less significant than in a transmission IR setup or a classical IRRAS setup because the path length of the IR beam in the air is much shorter. However, it must be noted that it is not still a factor to neglect when interpreting a micro-IRRAS spectrum. Furthermore, the spatial resolution of the micro-IRRAS setup offers the advantage of measuring the signal of the tribofilm that has been subjected to the tribological test, and of comparing it with the spectrum of the film outside of the wear track, which has not been subjected to the mechanical stress. This method also allows for to assessment of the molecular orientation of adsorbed species on metallic surfaces. When bouncing off the metal surface, the component of the electric field parallel to the surface is zero. Therefore, only the perpendicular component of the transition dipole moment of the vibration is detected. The format of such information is rather complex, but it is possible to judge orientational differences by comparing the relative intensities of the vibrational peaks observed in the spectra. In the interpretation of the

micro-IRRAS data, the thickness of the oxide layer is assumed to be thin enough so that its dielectric constant does not play a major role in determining IRRAS relative intensities. [63]

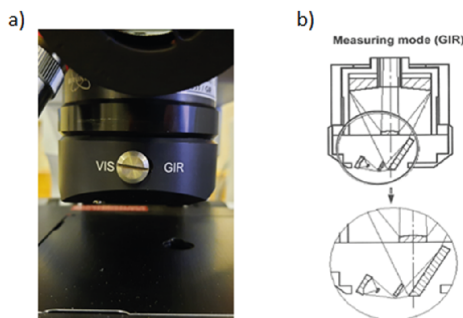

Figure 2.5: *a) Picture of the grazing incidence reflectance (GIR) objective. b) Scheme showing the working principle of the GIR objective. Scheme by courtesy of Bruker.*
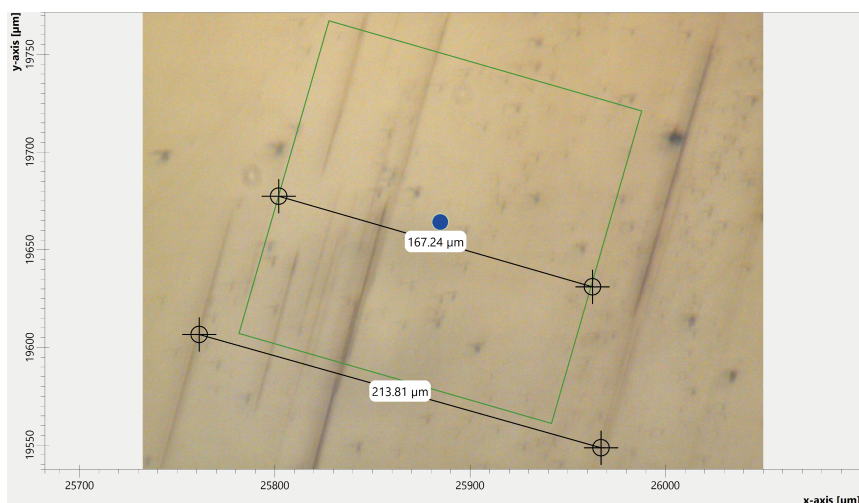

Figure 2.6: *Snapshot of the wear track under the GIR objective. The green box corresponds to the measured spot which is on an area of around 160 × 160 μm^2. The width of the wear track is about 200 μm.*

2.4   Density Functional Theory and DFT-MD methods

Density Functional Theory (DFT[2]) is a widely used computational method to perform calculations on many-body systems at the molecular scale. In DFT, the properties of such systems are calculated using energy functionals, as for the Hohenberg and Kohn theorem the true electronic density of the system minimizes the Energy potential $E[\rho(r)]$, where $\rho(r)$ is the electron density. The Energy functional in the scheme of Hohemberg and Kohn is defined as:

$$E[\rho] = E_{ne}[\rho] + T[\rho] + E_{ee}[\rho] = \int \rho(r)V_{ext}(r)dr + F_{HK}[\rho] \quad (2.1)$$

The functional includes the electron-nuclei interaction $E_{ne}[\rho]$, the electron-electron interaction $E_{ee}[\rho]$, and the kinetic energy term $T[\rho]$. $F_{HK}[\rho]$ is the Hohemberg -Kohn functional which is defined as:

$$F_{HK}[\rho] = T[\rho] + E_{ee}[\rho] = \langle \Psi | \hat{T} + \hat{E}_{ee} | \Psi \rangle \quad (2.2)$$

This is an exact functional. However, it is unknown. DFT uses an approximated functional to describe this term (and in particular the kinetic term) via an effective potential with an exchange-correlation (XC[3]) term that was introduced by Kohn and Sham. The idea is to compute the kinetic energy of a fictitious system S of independent particles that possess the same density as the real system. The resulting kinetic energy is not the true one but it is a good approximation of it. The effective Kohn-Sham potential is given by:

$$V_{eff}[\rho] = V_{ext}[\rho] + \int \frac{\rho(r)}{|r - r'|} dr' + V_{xc}[\rho(r)] \quad (2.3)$$

Where for a molecular system, $V_{ext}[\rho(r)]$ is at minimum the electron-nuclei interaction, and:

$$V_{xc} = \frac{\delta E_{xc}[\rho(r)]}{\delta \rho(r)} \quad (2.4)$$

By minimizing F_{HK} with respect to $[\rho]$, the problem is then reduced to satisfying the Kohn-Sham equation:

$$\left[-\frac{1}{2}\nabla^2 + V_{eff} \right] \psi_i(r) = \epsilon_i \psi_i(r) \quad (2.5)$$

---

[2]DFT: Density Functional Theory
[3]XC: exchange-correlation

Under the orthonormality constraint:

$$\langle \psi_i | \psi_i \rangle = \delta_{ij} \tag{2.6}$$

Among the practical aspects of the execution of a DFT calculation, one has to choose a suitable functional which defines the exchange-correlation terms. Several types of functional can be used to perform DFT calculations and they all vary in their level of theory (i.e. the level of approximations made) and performance. Hence one has to choose one that is suitable for the system that is being investigated. The main classes of DFT functionals are:

- LDA (local density approximation) functionals, where the XC functional is defined from considering locally uniform electron densities;

- LSD (local spin density approximation) functionals, similar to the LDA approximation. However, it considers electrons with spins of different directions;

- GGA (generalized gradient approximation) functionals, where the non-homogeneity of the electron density is taken by considering terms depending on the gradient of the density;

- Hybrid DFT-HF (Hartree-Fock) functionals, that introduce the HF exchange term to exploit opposite systematic errors that cancel out.

Another crucial aspect in DFT calculation is the choice of suitable basis sets. A basis set is a set of functions used to approximate the orbitals $|\psi_i\rangle$ as linear combinations of functions ϕ_j such as:

$$|\psi_i(r)\rangle = \sum_j c_{ij} |\phi_j(r)\rangle \tag{2.7}$$

In the DFT calculations described in this thesis I made use of atomic orbitals basis sets.

2.4.1 CRYSTAL17 calculations

To perform DFT models of the adsorbed OFM molecules, the code CRYSTAL17 was used. CRYSTAL17 is a software developed in Politecnico di Torino, notoriously suited for solid-state periodic systems such as those of interest for this study. [64] The SAMs of the OFMs were simulated in adsorption on a hematite (0001) surface within two-dimensional periodic

boundary conditions (slab model). The B3LYP [65–67] functional was adopted with a gaussian-type POB-DZVP basis set. [68] Grimme's correction for dispersion interactions was included in the calculations through the D3(BJ) scheme. [69–71] Initially, to reduce the computational burden, shorter versions of the OFM (C_6) molecules were used instead of the complete C_{18} molecules. This simplification is possible since the structural and electronic properties of the head groups which are of main interest in studying the adsorption of OFMs on steel are not affected by the alkyl chain length. [72] The structure of Fe_2O_3 (0001) plane is formed by a stack of oxygen atoms alternated by a bilayer of iron atoms. Hematite is overall antiferromagnetic, as the whole structure is a stack of alternated spin-up and spin-down ferromagnetic layers comprising the iron atoms. In our quantum chemical models, we considered the $Fe_2\,O_3$ (0001) surface denoted Fe-O_3-Fe-R (Fig. 2.7). [73] This single-Fe terminated structure has been chosen as it has been shown by theoretical and experimental studies to be the one most thermodynamically stable at room temperature. [73,74] Moreover, this termination of hematite has been reported in the literature to be the most common product of steel passivation. [75] It is worth mentioning that although the choice of a Fe-terminated hematite surface represents a reasonable approximation, an AISI52100 steel surface is unlikely to be fully covered by an iron terminated layer. For example, the presence of Cr might result in the formation of chromium oxide on the surface, and while the Fe-terminated surface is quite stable in presence of dry oxygen, in a humid environment hydroxylation may occur. [60] However, as it will be shown in chapters 3 and 4, this does not seem to affect the comparison between calculated and measured micro-IRRAS spectra. Nevertheless, taking into account these aspect might provide a better representation of the steel surface. The antiferromagnetism of hematite was considered in the CRYSTAL17 input by proper control of the expected α and β spins of the iron sites. [76, 77] In the calculations of the isolated hematite slab, and of the SAMs on hematite, it was run a full geometry relaxation of both the cell parameters and the atomic positions of all the atoms in the cell (hematite and SAM). This allows better reliability in the assessment of the vibrational properties of the SAM interacting with hematite. The calculation of the IR spectra was carried out on the optimized slab structures with the standard procedure implemented in CRYSTAL17. [77–82] Examples of the input files can be found in Appendix A, section 1. To calculate the adsorption energies of the OFMs at the surface, besides the fully optimized structures of the adsorbed molecules on hematite, full optimizations of a single OFM molecule and models of a bare hematite slab were also carried out. The
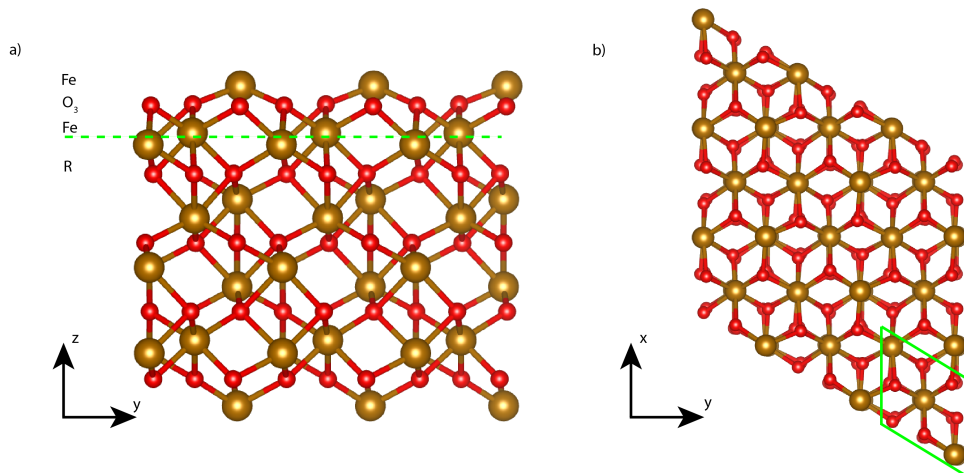
Figure 2.7: *a) Side view of the Fe_2O_3 slab cut to obtain the Fe-O_3-Fe-R termination (single-Fe). b) Top view of the surface of the Fe2O3 slab.*

total energies of the models were computed and the adsorption energy of the OFM at the surface was calculated as follows:

$$\Delta E_{ads} = \frac{1}{N} E_{mol@hem} - (\frac{1}{N} E_{hem} + E_{mol}) \qquad (2.8)$$

Where $E_{mol@hem}$ is the energy of the OFM adsorbed on hematite, E_{hem} is the energy of the bare hematite slab, E_{mol} is the energy of an isolated OFM molecule, and N is the number of molecules of OFM per cell considered. In our models, each cell has exactly one molecule in it. Therefore, N=1, and the adsorption energy can be calculated as a simple energy subtraction:

$$\Delta E_{ads} = E_{mol@hem} - (E_{hem} + E_{mol}) \qquad (2.9)$$

The adsorption energy of the OFM at the hematite surface can be separated into two contributions: one describing the interaction of the polar head of the OFM on the hematite slab, which we call interaction energy (ΔE_{int}), and the other representing the interaction among adjacent molecules of the SAM, which is a measure of how tightly packed are the OFM molecules at the surface. For this reason, the latter term has been named packing energy (ΔE_{pack}). The adsorption energy is then described as:

$$\Delta E_{ads} = \Delta E_{int} + \Delta E_{pack} \qquad (2.10)$$

In order to calculate these two contributions, a model of a slab of OFM molecules arranged in a SAM without the hematite slab is required. The

energy $E_{mol,slab}$ of this model is calculated and the packing energy is obtained as follows:

$$\Delta E_{pack} = E_{mol,slab} - N * E_{mol} \qquad (2.11)$$

Where N=1, since only one molecule per cell is present. The interaction energy of the polar head on the surface of hematite is:

$$\Delta E_{int} = E_{mol@hem} - (E_{hem} + E_{mol,slab}) \qquad (2.12)$$

The separation of the adsorption energy into its interaction and packing terms allows important considerations about the relevance of each contribution in reducing friction (see chapter 5). However, these are calculated at 0K and come from static models. Therefore, no information about temperature and molecular disorder is taken into account, which is also why we also considered calculations of the Gibbs' free energy (which procedure will be discussed further on in this chapter).

2.4.2 CP2K calculations

Born-Oppenheimer DFT-MD simulations have been performed using the CP2K package with the quickstep module, in which at each time step the electronic wavefunction and the set of forces are calculated via DFT and the nuclei displacements are treated classically. [83–85] As in the CRYSTAL17 calculations, the B3LYP [65–67] functional was adopted, augmented with the Grimme's D3 dispersion correction [69–71] to better describe the Van der Waals interactions between the molecules in the adsorbed layer. A hybrid Gaussian and plane waves (GPW) basis set, consisting of 400 Ry energy cutoff plane-wave basis set, coupled with the DZVP-MOLOPT-GTH-SR basis set [86], was selected but for the Fock exchange term. Due to the enormous computational cost of this latter term, the auxiliary cpFIT3 (for the O, C, and H atoms) and cFIT11 (for iron) basis sets were employed instead with the Auxiliary Density Matrix Methods (ADMM). [87] The antiferromagnetism of hematite was taken into account by defining the alpha and beta electron population. To correctly describe the band gap and taking better ccount of electron correlations of the 3d electrons, a Hubbard U-J value of 4 eV in the Dudarev approach was added [88], consistently with the literature on hematite calculations. [61] In the case of the 0K static calculations this correction increases the computational cost without real advantages. The system is simulated at the bottom of the potential well and we are not interested to conduction properties, i.e., the underestimation

of the band gap is not so relevant. Nevertheless, tests have been done obtaining negligible difference in the optimized geometry with and without the U term. However, during the MD simulation, especially at high temperatures, the system can explore regions quite up on the potential energy surface. It is therefore a safer choice to activate this correction. The optimized CRYSTAL17 structures were used as starting geometries for the CP2K input. The default algorithms and convergence criteria present in CP2K have been adopted. Periodic boundary conditions (PBC) in all three directions have been applied, imposing a cell dimension of 30 Åin the z-direction so that the two slab replicas would not interact with each other. Before running the DFT-MD calculation, the structure was re-optimized in CP2K, obtaining a geometry which was consistent with the result from CRYSTAL17. Regarding the dynamics part of the calculation, two simulations were performed at 300 and 423K, respectively. The dynamics were divided into two sections. An equilibration run for 5 ps and a production run for another 5 ps. The equilibration has been performed in the NVT ensemble. NVT trajectory of 5 ps was run to equilibrate the system at 300 K. A CSVR thermostat (time constant 300 fs) was applied together with the automatic rescaling of the velocities each time the temperature fluctuations exceed the threshold of ± 30K. [89] From the production run trajectory, all spectroscopic analyses were performed (IR spectra). A sample of the input files can be found in Appendix A, section 2. The calculation of the IR spectra from the molecular dynamics trajectory was done through the method described in ref. [90], which is based on the Berry phase method for the definition of the dipole moments in an infinite periodic system. [91, 92] In brief, the intensity of the IR spectra is calculated as a Fourier transformation of the dipole autocorrelation function:

$$I(\omega) = \frac{2\pi\beta\omega^2}{3cV} \int_{-\infty}^{+\infty} \exp(i\omega t)\langle \delta\mu(t) \cdot \delta\mu(0)\rangle dt \qquad (2.13)$$

Where $\beta = 1/k_B T$, ω is the frequency of the absorbed light, c the speed of light (in vacuum), V the volume of the system, and $\delta\mu(t)$ the instantaneous fluctuation of the dipole moment. A prefactor $\beta\hbar/(1-\exp(-\beta\hbar\omega))$ to take the nuclei classical line shape was included. [93] Due to the computational costs involved, these calculations were run on the Galileo100 infrastructure at CINECA.

2.5 Classical Molecular Dynamics

In order to overcome the limitations of DFT in terms of number of atoms and time scale in investigating the dynamic evolution of a system composed by a large number of adsorbed molecules subjected to macroscopic forces, larger-scale models which describe the interaction among atoms with classical potentials and Newton mechanics have been employed. In the present study, the well-established code LAMMPS (Large-scale Atomic/Molecular Massively Parallel Simulator) [94] was used. This enables the investigation of the evolution in time of the positions of each atom of a complex large system subjected to external forces. When performing molecular dynamics (MD[4]) models, is crucial to choose suitable force-fields (FF [5]) that describe the system in the most accurate way possible. A FF is a set of potentials that describe inter- and intramolecular interactions. The available literature adopts a wide variety of FFs for the description of the adsorption of fatty acid molecules on steel surfaces. Moreover, detailed information about the FF parameters was not available in most cases. For these reasons, I have chosen one FF that was employed to describe the organic molecules that constitute the OFMs and the base lubricant oil, and another one was used to describe the hematite slab. The FF used for the OFMs and base lubricant oil was the L-OPLS-AA. [95, 96] This choice of FF comes from a precedent study that benchmarked many non-reactive FFs for the description of OFMs (or in general of long hydrocarbons) and found this one to be most consistent with the experimental values for a wide variety of macroscopic quantities. [97] The L-OPLS-AA FF describes intramolecular potentials up to the description of the dihedral angle potential. Intermolecular interactions (including the interactions between the headgroup of the molecule and the hematite surface) were instead described by a Lennard-Jones potential and a Coulombic electrostatic term. When describing the hematite slab, the choice was to use a Buckingham potential with a Coulombic electrostatic term, as described by previous studies on hematite. [98, 99]

---

[4]MD: Molecular Dynamics
[5]FF: Force-Field

2.5.1 Intermolecular and Intramolecular Potentials

Lennard-Jones Potential

The interatomic Lennard-Jones (LJ[6]) potential takes the standard 12/6 form:

$$V_{LJ} = 4\epsilon_0 \left[\left(\frac{\sigma}{r_{ij}} \right)^{12} - \left(\frac{\sigma}{r_{ij}} \right)^{6} \right] \qquad (2.14)$$

Where ϵ is the depth of the potential well of the LJ function (i.e. energy at equilibrium), σ is the distance at which the potential energy is equivalent to zero, and r is the distance between two atoms i,j. A cut-off distance has been chosen at 10 Å.

Buckingham Potential

The Buckingham potential takes the form of an exponential/6 instead of the standard LJ 12/6 form:

$$V_{buck} = A \exp(-Br_{ij}) - \frac{C}{r_{ij}^6} \qquad (2.15)$$

Where A, B, C are constants and r_{ij} is the interatomic distance between atoms i and j. A cut-off distance has been chosen at 10 Å.

Coulomb Electrostatic Potential

Electrostatic interactions are described by a Coulomb potential of the form:

$$V_{q_1 q_2} = C \frac{q_i q_j}{\epsilon r_{ij}} \qquad (2.16)$$

Where C is an energy-conversion constant, q_i, q_j are the charges of the two atoms i, j, ϵ is the dielectric constant, and r_{ij} the distance between the two atoms. In this case, it was chosen to let this interaction be long-range in both the L-OPLS-AA FF and in the description of the hematite slab, in addition to the Buckingham term.

Harmonic Bong Potential

The function describing the bond between two atoms i, j is described through a harmonic bond of the type:

$$V_{ij} = K_r(r_{ij} - r_0)^2 \qquad (2.17)$$

---

[6]LJ: Lennard-Jones potential

Where K_r is the force constant of the harmonic bond, r_{ij} is the bond distance, and r_0 is the bond distance at equilibrium.

Angle Potential

The function that describes the angle potential takes a harmonic form of the angle θ between three i, j, k connected atoms:

$$V_{ijk} = K_\theta (\theta_{ijk} - \theta_0)^2 \tag{2.18}$$

Where K_θ is the force constant, θ_{ijk} is the bending angle and θ_0 is the bending angle at equilibrium (minimum energy).

Dihedral (Torsional) Potential

The potential that describes the energetic contribution from a dihedral angle in the L-OPLS-AA FF is a Fourier function. This function can be converted into a form of the Ryckaert-Bellemans potential function, which is a sum of cosine terms of the dihedral angle ϕ:

$$V_{RB} = C_0 + C_1(\cos\phi) + C_2(\cos\phi)^2 + C_3(\cos\phi)^3 \tag{2.19}$$

Where C_0, C_1, C_2, and C_3 are the optimized L-OPLS-AA parameters. Examples of the input files where all the details of the FFs are specified are provided in Appendix A, section 3.

2.5.2 Ewald method

Coulomb interactions decrese with increasing interatomic distance. When building an MD model, a cut-off can be introduced, past which the coulombic interactions between atoms are not considered anymore. However, to take long-range interaction into account more accurately, MD codes often employ the Ewald method to improve the reliability of the calculation of these terms. In LAMMPS, the Ewald method can be applied in a variety of ways. In this study, the particle-particle-mesh solver (pppm) [100] is used, which maps atom charges into a 3D mesh in the k-space, then uses 3D fast-Fourier transforms to solve the Poisson's equations on the mesh and finally interpolates the electric fields on the mesh back on the atoms. [101] The Coulombic interaction potential is split into its short (SR) and long-range (LR) terms $V_{coul,tot} = V_{SR}(r) + V_{LR}(r)$. The short-range term is computed as a direct sum of the potentials in the real space, meanwhile, the long-range

term is computed in the reciprocal k-space as follows:

$$V_{LR} = \sum_k \tilde{\Phi}_{LR}(k)|\tilde{\rho}(k)|^2 \tag{2.20}$$

Where $\tilde{\Phi}_{LR}(k)$ are the Fourier transforms of the potential and $\tilde{\rho}$ is the Fourier transform of the charge density. This is done because equation 2.20 converges quicker in the reciprocal space than in the real space and can be truncated earlier with no accuracy loss. In addition to improving computational efficiency, since while traditional Ewald summation scales as $N^{\frac{3}{2}}$, this k-space method scales as $N \log N$ (N being the number of atoms of the system).

2.5.3 Verlet Algorythm

The Verlet algorithm is a numerical method employed to speed up the integration of Newton's equations of motion. LAMMPS allows using different styles of the Verlet algorithm. In this study, the default velocity form of the Stoermer-Verlet time integration (velocity-Verlet) algorithm is used in both LAMMPS and CP2K simulations. The algorithm is implemented as follows:

- 1. $v(t + \frac{1}{2}\Delta t) = v(t) + \frac{1}{2}a(t)\Delta t$

- 2. $x(t + \Delta t) = x(t) + v(t + \frac{1}{2}\Delta t)\Delta t$

- 3. deriving the new value of $a(t)$ from the interaction potential at the new position at $t + \Delta t$

- 4. $v(t + \Delta t) = v(t + \frac{1}{2}\Delta t) + \frac{1}{2}a(t + \Delta t)\Delta t$

2.5.4 Model setup

The initial geometry for the MD simulations was constructed using the VMD (Visual Molecular Dynamics) software. [102] The single-cell geometries from the CRYSTAL17 optimizations of the adsorbed OFM molecules on hematite were taken and a 10x10 slab was generated. A first set of simulations was run on the single 10x10 slab, to investigate the effect of temperature on the tribofilm without any external tribological force applied. The simulations were run at 300K, 420K, and 500K using a Nose-Hoover thermostat (T_{damp} = 40K) in an NVT ensemble. After a first equilibration run of 1 ns, a production run of 2 ns was performed. A copy of the

10x10 initial slab was generated and placed on top of the first one mir-roring it at a distance of 60 Å. This formed an empty space between the two slabs which was filled with 75 molecules of squalane to simulate the base lubricant oil. The system was then subjected to a pressure of 0.5 GPa ($P_{damp} = 4x10^{-2}GPa$) at 300K, 420K, and 500K (in separate runs) for 0.5 ns to squeeze the two layers and form a sandwich-like structure. The resulting system is shown in Fig. 2.8. The dynamics were repeated three times with different velocity initialization seeds to ensure that the results were not affected by the initial velocity conditions. The system made this
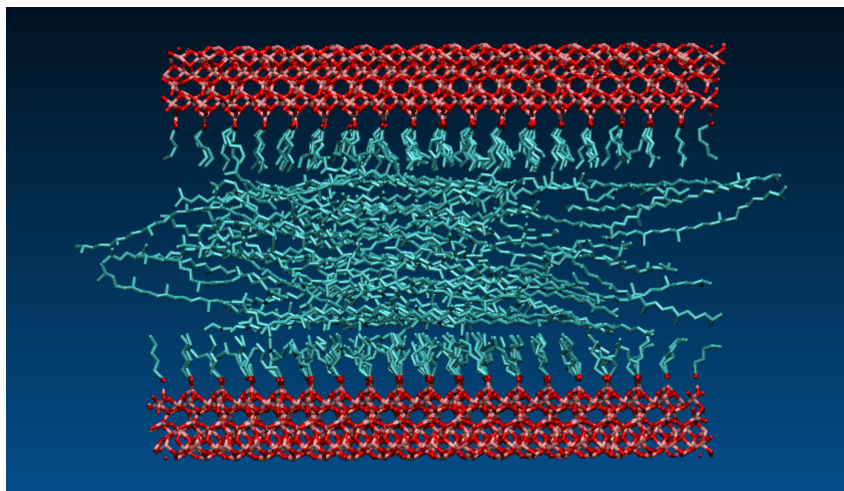

Figure 2.8: *Starting geometry of the MD simulation. The hydrogen atoms have been hidden for viewing purposes.*

way was used as a starting point for the simulation of tribological phenom-ena (i.e. the two slabs sliding on each other in opposite directions). To do this, a velocity was applied to the outermost hematite layers of the two slabs in opposite directions of ± 0.5 m/s, for a total relative velocity of 1 m/s, which is in the range of velocities applied in the tribological MTM tests, corresponding to the boundary-mixed lubrication region. To investi-gate the effect of temperature, simulations were carried out at 300K, 420K, and 500K. The pressure was kept at 0.5 GPa for the entire duration of the simulation. This set of simulations was run for a total of 2.5 ns and the sliding direction was inverted two times: The first time after 0.5 ns and the second one after 1 ns from the first one. The rationale behind this choice was to simulate the action of an engine piston. All the trajectories were then visualized and analyzed through the VMD software. The LAMMPS input files for the simulations are included in Appendix A, section 3.

2.6 Other Computational Methods

In this section, the in-house scripts used for the analysis of the outputs from DFT and MD calculations are described.

2.6.1 Calculation of angle-dependent IR spectra

Since IRRAS spectroscopy is sensitive to the component of the vibrational transition dipole moment that is perpendicular to the metallic surface, it comes naturally that the IR spectra routinely calculated from the DFT models - which take into account all the components of the transition dipole moment - will not be able to correctly represent the orientational character of the adsorbed OFM molecules at the surface. However, using some maths, it is possible to calculate polarized IR spectra on any given direction. This is done by generating a vector v on which the transition dipole moment can be projected. From this projection, a new IR spectrum can be calculated that only takes into account the dipole moments oriented along the generated vector. By changing the angle of the generated vector with respect to the surface of the metal (in the models), IR spectra at an increasing angle can be computed. This is somewhat equivalent to simulating the selection rules of IRRAS spectroscopy, since, recalling what mentioned when describing micro-IRRAS, when bouncing off the metal surface, the component of the electric field parallel to the surface is zero. Therefore, only the perpendicular component of the transition dipole moment of the vibration is detected.

2.6.2 Gibbs Free Energies

The adsorption energies calculated from the CRYSTAL17 models are only valid at 0K. However, to investigate what happens to the tribofilm at higher temperatures, one has to calculate the Gibbs free energies, which take into account the dependence on temperature of the enthalpy and entropy of the system. To do this, the methodology described in references [103, 104], was used. Here the procedure will be briefly described focusing on the aspect relevant to this work. The free energies of adsorption can be partitioned in the same way as the adsorption energy at 0 K was. Analogously to equations 2.9, 2.10, 2.11, and 2.12, we then have:

$$\Delta G_{ads} = G_{mol@hem} - (G_{hem} - G_{mol}) \tag{2.21}$$

$$\Delta G_{int} = G_{mol@hem} - (G_{hem} - G_{mol,slab}) \tag{2.22}$$

$$\Delta G_{pack} = G_{mol,slab} - G_{mol} \tag{2.23}$$

$$\Delta G_{ads} = \Delta G_{pack} + \Delta G_{int} \qquad (2.24)$$

However in this case, ΔG contains not only the electronic term, but also contains the rotational, translational terms as well as the vibrational enthalpy and entropy terms:

$$G = E^{el} + E^{rot} + E^{tras} + G^{vib} = E^{el} + E^{rot} + E^{tras} + H^{vib} - TS^{vib} \quad (2.25)$$

The rotational and translational free energies are obtained from the CRYSTAL17 output. The vibrational enthalpy is calculated as:

$$H^{vib} = k_b \sum_i \frac{\hbar\omega_i/k_b T}{e^{\hbar\omega_i/k_b T} - 1} + E_0^{vib} \qquad (2.26)$$

E_0^{vib} being the zero point vibrational enthalpy:

$$E_0^{vib} = \sum_i \frac{\hbar\omega_i}{2} \qquad (2.27)$$

The vibrational entropy is calculated as:

$$S^{vib} = k_b \sum_i \left(\frac{\hbar\omega_i/k_b}{e^{\hbar\omega_i/k_b T} - 1} - \ln(1 - e^{\hbar\omega_i/k_b T}) \right) \qquad (2.28)$$

The in-house script takes the information derived from the CRYSTAL17 frequency calculation and computes all these terms for each model. Then the free energies of adsorption, packing and interaction can be calculated with equations 2.21, 2.22, and 2.23. In this approach to Gibbs' free energy calculations we used the harmonic approximation for the vibrational energies. Anharmonic effects, which can ultimately result in important deviations - for the entropic terms in particular - are not taken into account. [103, 105]

Spectroscopic investigation of adsorbed OFMs

3.1 OFM adsorption configurations

3.1.1 FT-IR spectra of OFMs in liquid phase

When performing vibrational spectroscopy to identify the presence of certain species, and to investigate perturbations of the molecular state upon adsorption, firstly the vibrational markers of the molecule must be identified. To do this, the FT-IR spectra of the OFMs in their liquid phase are collected so to identify their vibrational peaks before any perturbation and target which molecular vibrations are most likely to be involved in the adsorption process. In the general case of the adsorption of amphiphilic molecules suspended in apolar solvents on metallic surfaces, the markers of adsorption are generally thought to be the vibrational modes on the polar head of the molecule. [34, 61] In Fig. 3.1, the FT-IR spectra of oleic acid (OA), oleic amide (OAm), glycerol monooleate (GMO), XTJ785, and PC21 are shown. The modes of OA, OAm, and GMO can be safely assigned by comparison with the abundant literature on fatty acids terminated by carboxylic, amide, and ester groups. [62, 106, 107] To assign the modes of XTJ785 and PC21

in their liquid phase, their vibrational frequencies were calculated by DFT since a specific detailed assignation cannot be found in literature, although this could be in principle made with relatively good confidence from the literature on similar molecules (i.e. the C=O stretching of PC21 is similar to the C=O stretching in the OAm molecule). In all cases apart from XTJ785,
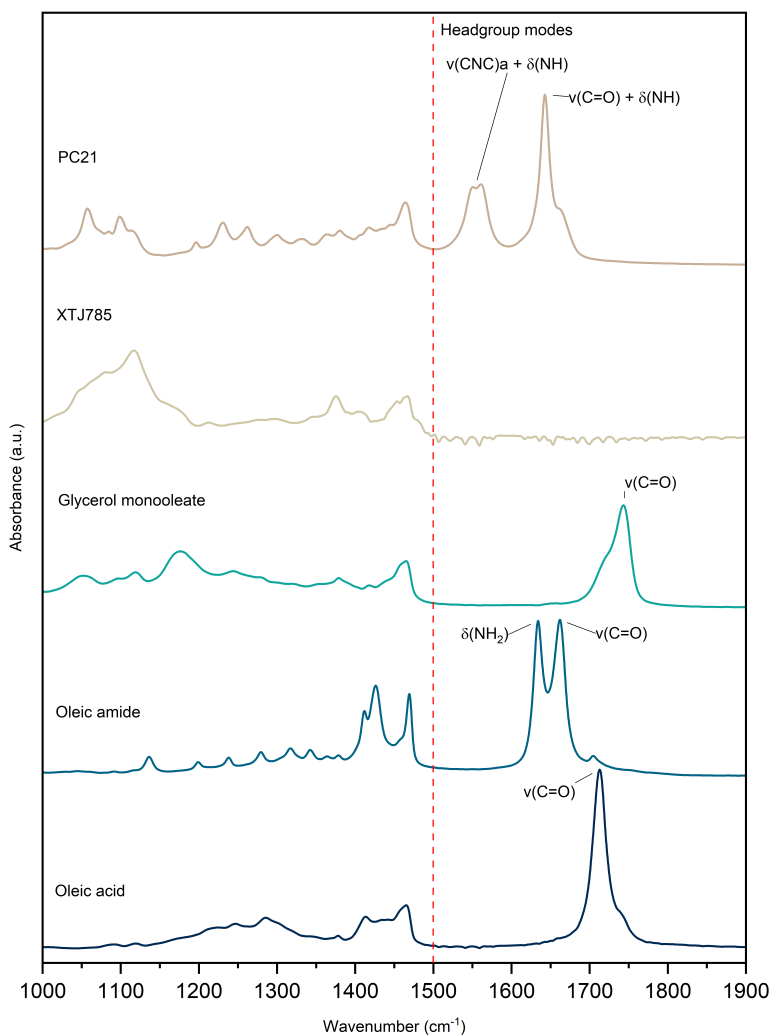

Figure 3.1: *FT-IR spectra of the OFMs investigated in the liquid phase.*

all the relevant headgroup modes are conveniently positioned in the region above 1500 cm^{-1}. For clarity purposes, the assigned vibrational modes are listed in Tab. 3.1. The case of XTJ785 is less straightforward, as there is no clear marker in the region above 1500 cm^{-1}. XTJ785 shows its C-O stretch-

ings together with its chain C-C stretching in the region between 1000 and 1200 cm^{-1}. In the FT-IR spectra recorded, the wavenumbers of the head-

Table 3.1: *List of headgroup vibrational modes and their assignations from the literature of liquid phase OA, OAm, GMO, and PC21. [62, 106, 107]*

Organic friction modifier	Wavenumber (cm^{-1})	Literature value (cm^{-1})	Vibrational Mode
Oleic Acid (OA)	1710	1750 - 1850	v(C=O)
Oleic Amide (OAm)	1660	1630 - 1695	v(C=O)
-	1635	1620 - 1670	δ(NH$_2$)
Glycerol mono oleate (GMO)	1740	1735 - 1750	v(C=O)
PC21	1640	1630 - 1695 (ester)	v(C=O) + δ(NH)
-	1550	1550 (mono-substituted amide)	v(CNC)a + δ(NH)

group vibrational modes are shifted compared to the typical values found in the literature. This is due to the formation in the liquid phase of hydrogen bonds between the polar heads of the molecules, which shifts the vibrational modes to lower wavenumbers. Another important aspect regards the modes in the region between 1400 and 1500 cm^{-1}, where the CH$_2$ and CH$_3$ bendings can be found. Among these, the scissoring of the CH$_2$ group (δCH$_2$) immediately adjacent to the polar head of the OFM molecules can be identified. The presence of this scissoring mode is a very important detail since its IRRAS signal contains information about the angle of the molecule at the surface. Indeed, when the molecule is adsorbed, the dipole moment variation $\partial\mu/\partial q_{bending}$ associated to the δCH$_2$ has a large component perpendicular to axis of the alkyl chain of the molecule. At variance, the CH stretching transitions (2800 - 3100 cm^{-1}), although in principle more intense, do not provide directly such information: their absorption bands are formed by convolutions of collective modes of the two sections of the alkyl chain that are separated by the C=C bond [47], in a *cis*- configuration. For different values of the orientation of the molecule with respect to the steel surface, the IRRAS intensity of the CH stretching contributions from such two sections vary in opposite ways for geometrical reasons, thus reducing the net effect on the total intensity. Therefore, we are not considering in this analysis the CH stretching region of the spectrum.

3.1.2 micro-IRRAS spectra of adsorbed OFMs

The spectra of the liquid OFMs samples can be now compared with the micro-IRRAS spectra recorded on the adsorbed tribofilms inside the wear track produced by the MTM tests. In the case of OA [37], The intense

v(C=O) band at 1710 cm^{-1} of the liquid phase is replaced in the tribofilm by the rise of two bands at 1646 cm^{-1} and 1524 cm^{-1}. Interestingly, a shoulder at exactly 1710 cm^{-1} is still recognizable in the spectrum of the tribofilm, which indicates the presence of a small quantity of non-adsorbed oleic acid molecules. The spectrum of the tribofilm reported in Fig. 3.2 compares well with the typical spectrum expected from the formation of a carboxylate layer on the surface of steel [62, 106, 107]. The two v(C=O) bands at 1646 cm^{-1} and 1524 cm^{-1} are often assigned to either a monodentate or bridging coordination of the oxygen of the CO groups of the molecule on a Fe atom at the surface [34, 107, 108] that is associated to the deprotonation of the -COOH group (this deprotonation of the headgroup will be a recurrent phenomenon for all OFMs investigated). As described
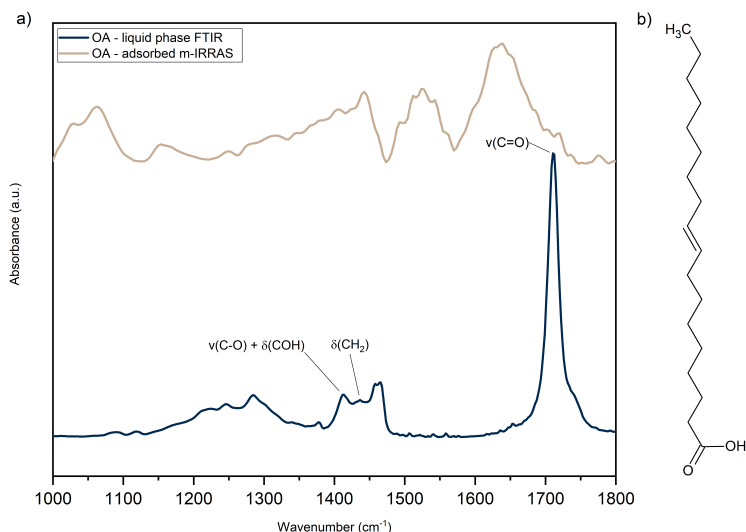

Figure 3.2: *a) micro-IRRAS spectrum of oleic acid adsorbed on the MTM sample, in the section affected by the tribological tests, and FT-IR spectrum of oleic acid sample (liquid). b) Molecular structure of oleic acid.*

in Fig 3.3, the oxygen of the CO group can be coordinated either with another Fe of the surface, forming the so-called bridging configuration, or it can form a hydrogen bond with the dissociated proton of the -COOH group to form a monodentate configuration. In Figures, 3.4, 3.5, 3.6, 3.7, the spectra of the adsorbed tribofilms of OAm, GMO, XTJ785, and PC21 are reported. In all cases, adsorption results in the shift of the headgroup bands to lower wavenumbers or in the rise of new bands in the 1500 - 1600 cm^{-1}. This, in first analysis, cannot be straightforwardly ascribed to the deprotonation of the headgroup and subsequent coordination to the surface irons of
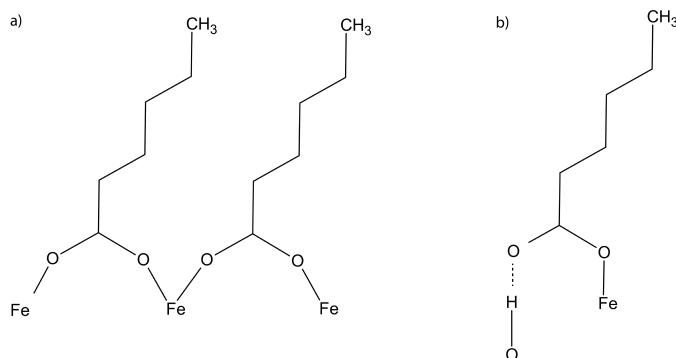
Figure 3.3: *Sketch of the a) bidentate bridging and b) monodentate coordination.*

the oxygen present on the head of the molecule, as it is done for the adsorption of OA. Moreover, in these cases, there is no clear literature available to unequivocally identify the termination that is interacting on the surface or the configuration the molecule is assuming on the surface. For this reason, DFT calculations of the adsorbed IR spectra have been necessary and are discussed in the following section of this chapter.

In the specific case of OAm, adsorption gives rise to two bands at 1538 and 1573 cm^{-1} (Fig. 3.4). In the literature, these are often assigned to mono-substituted amides. [106] Therefore, it can be assumed that deprotonation occurred on the NH$_2$ group. However, the bands belonging to the unaltered OAm headgroup can be spotted, although much less intense and broadened.

In the spectrum of adsorbed GMO (Fig. 3.5), compared to the spectrum in the liquid phase, it can be clearly seen that the v(C=O) is shifted from 1740 cm^{-1} to 1665 cm^{-1}. The first conclusion one would take is that the C=O termination of the ester head of GMO is interacting with a surface iron to cause the shift. However as it will be shown in the next chapter, this is not the case.

The spectrum of adsorbed XTJ785 shows to be riddled with heavy noise. During the experimental activities, to the best of our effort we could not avoid the noise that is shown in Fig. 3.6. Moreover, as it was previously noticed, XTJ785 does not possess clear markers in the 1500 - 1700 cm^{-1} region. Looking at the 1000 - 1200 cm^{-1} region, a shift of the band towards lower wavenumbers can be observed. This may be due to the interaction of the C-O end-groups of the head of XTJ785 interacting on the surface. However, during the experimental observation, the spectral region below 1200 cm^{-1} (in the micro-IRRAS) has been systematically subjected to is-
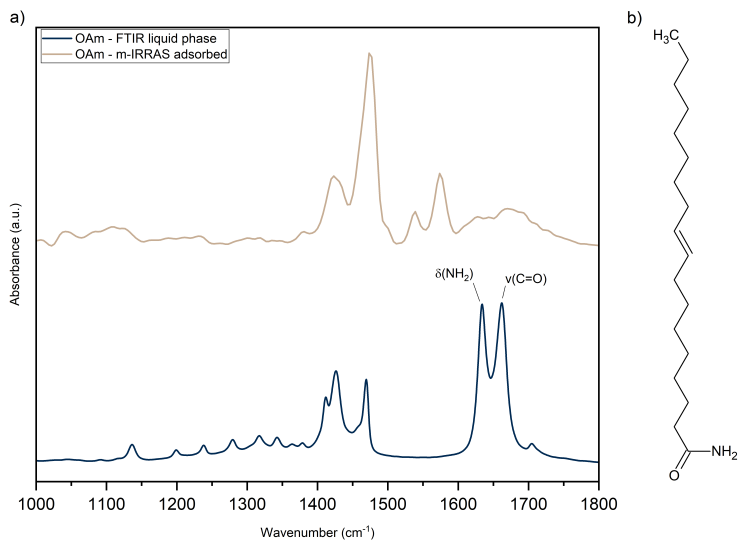
Figure 3.4: *a) micro-IRRAS spectrum of oleic amide adsorbed on the MTM sample, in the section affected by the tribological tests, and FT-IR spectrum of oleic amide sample (liquid). b) Molecular structure of oleic amide.*
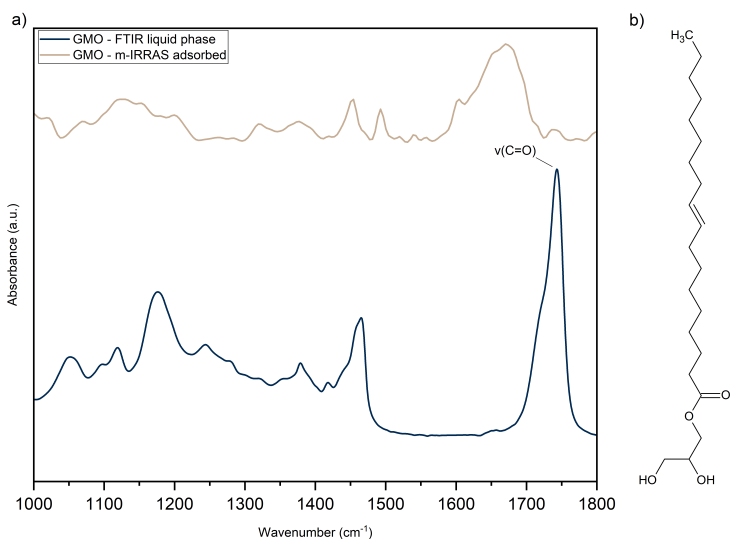

Figure 3.5: *a) micro-IRRAS spectrum of GMO adsorbed on the MTM sample, in the section affected by the tribological tests, and FT-IR spectrum of GMO sample (liquid). b) Molecular structure of GMO.*

sues regarding the choice of the baseline. Nonetheless, the DFT-calculated spectra (see chapter 4) seem to corroborate the adsorption process proposed
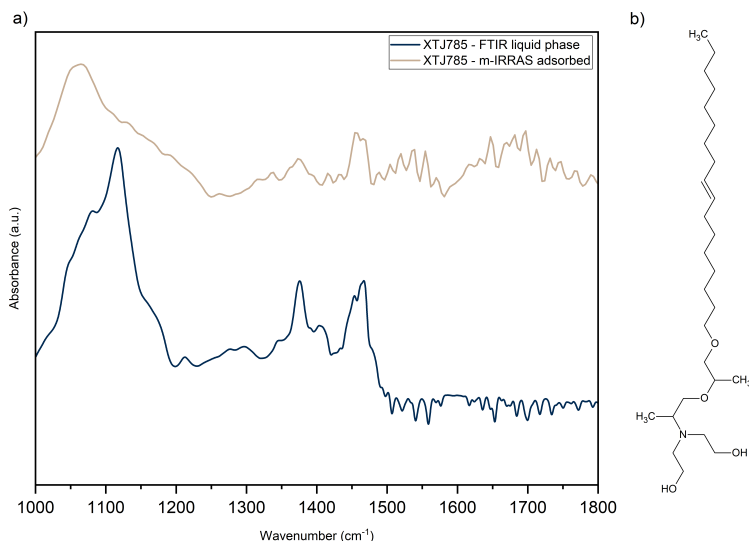
here.

Figure 3.6: *a) micro-IRRAS spectrum of XTJ785 adsorbed on the MTM sample, in the section affected by the tribological tests, and FT-IR spectrum of XTJ785 sample (liquid). b) Molecular structure of XTJ785.*

Finally, the adsorbed micro-IRRAS spectrum of PC21 is compared with its FTIR spectrum in the liquid phase (Fig. 3.7). The peak at 1640 cm^{-1} corresponding to the v(C=O) + δ(NH) mode and the peak at 1550 cm^{-1} corresponding to the v(CNC)a + δ(NH) mode are slightly shifted of 10 cm^{-1} to the lower wavenumbers. This suggests that PC21 does not adsorb on the surface through these end-groups. However, it suggests that, as in the liquid phase OFMs, there are hydrogen bonds involved. As in the case of GMO, it can be assumed that the molecule is interacting on the surface through the C-O terminations.
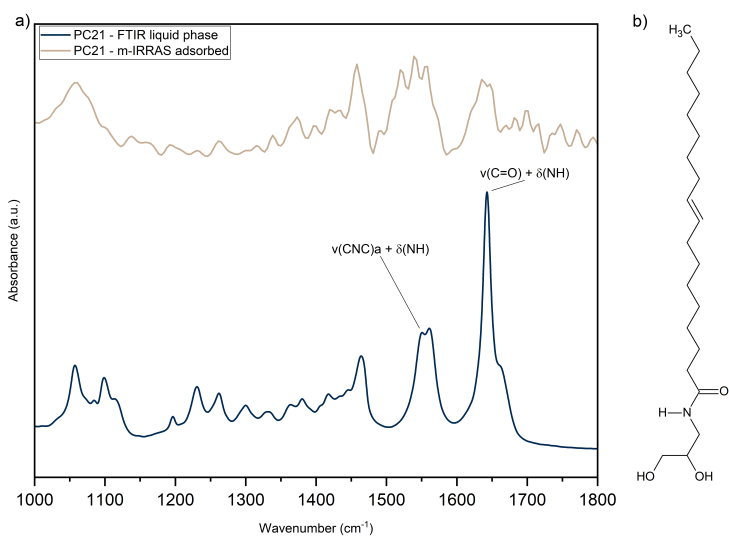
Figure 3.7: *a) micro-IRRAS spectrum of PC21 adsorbed on the MTM sample, in the section affected by the tribological tests, and FT-IR spectrum of PC21 sample (liquid). b) Molecular structure of PC21.*

3.2 micro-IRRAS as a probe for evaluating competition among additives at the steel surface

When more additives are present that may adsorb on the surface of steel, a process of competition occurs, resulting in partial or null adsorption of one or more additives. This process can significantly reduce the performances of a fully-formulated lubricant, as well as improve them if the mixture is tuned so that each additive is sufficiently adsorbed on the surface. Currently, the process of pinning down the optimal ratio between the additives relies on the formulation of mixtures and measurement of friction coefficients, without a reliable experimental tool that may provide insights on the adsorption process that occurs when more additives are present in the mixture. Since micro-IRRAS has proven to be able to consistently detect OFM layers on the surface of the steel, the technique was employed for the investigation of samples that contain more than one additive, to assess the state of the tribofilm, and thereby the results of the competition process.

3.2.1 Competition between friction modifiers

When more friction modifiers are present in a lubricant mixture, as it has been demonstrated in the literature, the competition process can bring to one of four results [109]:

- Antagonism, when the friction coefficient for the lubricant mixtures with more additives results higher than that of the formulations with the single additives;

- Synergy, when the friction coefficient is lower than what would be obtained with the single additives;

- Domination, when the friction coefficient is coincident with what would be obtained with one of the additives;

- Mutual action, when the friction coefficient is in between the values produced by the single additives.

Fig. 3.8 compares the micro-IRRAS spectrum of the region affected by the tribotests of an MTM sample immersed in a lubricant containing equal parts of OA and PC21 (1% wt. each) with the spectra obtained from the single friction modifiers. By comparison, features that can be ascribed to the presence of both OA and PC21 can be observed in the region 1500-1700 cm^{-1}, suggesting that both OFMs do adsorb on the surface and may

be interacting. However, the band at 1457 cm^{-1} is only present on the spectrum of PC21, while OA shows a similar band at 1444 cm^{-1}, which is not detected in the sample that contains both OA and PC21. This seems to corroborate the hypothesis that PC21 is more adsorbed on the surface than OA.
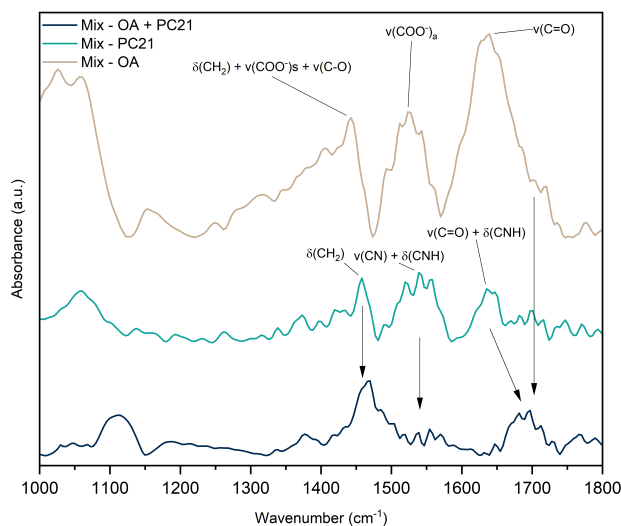

Figure 3.8: *micro-IRRAS spectrum recorded on the MTM sample that was immersed in a lubricant containing both PC21 and OA (black), in the section affected by the tribological tests, and micro-IRRAS spectra of adsorbed PC21 and OA (blue and brown, respectively).*

3.2.2 Competition between friction modifiers and anti-wear

As previously mentioned, lubricant formulations contain a variety of additives that adsorb on the surface. In order to get the most functionality out of each additive, all of them need to adsorb sufficiently. In the case of anti-wear agents, these need to adsorb in order to form their protective layer on the surface. In this specific case, BB22, an anti-wear belonging to the class of ZnDTPs was investigated, in two mixtures containing equal parts (1% wt.) of OA and PC21, respectively. In order to interpret the micro-IRRAS spectra of the mixtures adsorbed on steel, similarly to what was done in section 3.1, the ATR spectrum of BB22 is compared to its micro-IRRAS spectrum, when adsorbed on steel (Fig. 3.9). The comparison clearly shows the effect of adsorption. The phosphate band at ~1000 cm^{-1} shifts to 1200 cm^{-1}, meanwhile the alkyl portion of the spectrum

is not observable anymore, indicating that the phosphate layer has formed on the surface. We now can compare the micro-IRRAS spectrum recorded
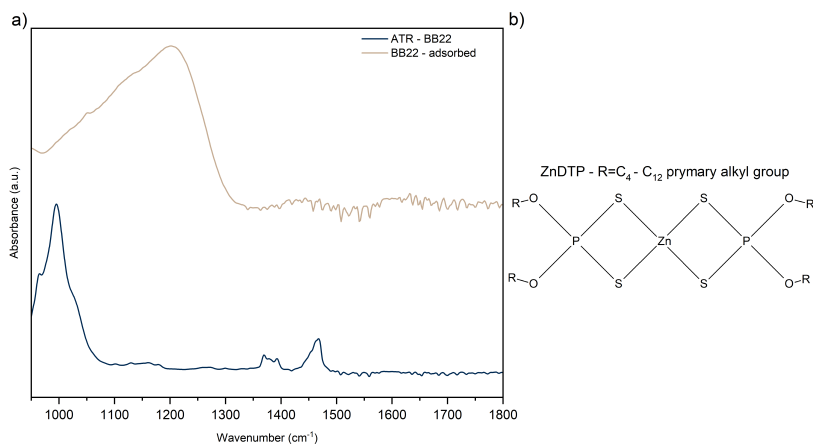

Figure 3.9: *a) micro-IRRAS spectrum of BB22 adsorbed on the MTM sample, in the section affected by the tribological tests, and ATR spectrum of BB22 sample (liquid). b) Molecular structure of BB22.*

on an MTM sample immersed in a lubricant containing equal parts of OA and BB22 (1% wt. each) with the spectra of the singularly adsorbed additives (Fig. 3.10). Features of OA can be clearly observed in the 1400-1700 cm^{-1} region, while the phosphate band of BB22 is not detected, suggesting that in this case, OA clearly dominates the adsorption at the surface. Similarly, this happens when BB22 is mixed with PC21 in equal parts (1% wt. each). Comparing the micro-IRRAS spectra (Fig. 3.11), of the mix with the single additives adsorbed, the phosphate band is again not detected. However, also the features of PC21 seem to not be present. Only the band at ∼1070 cm^{-1} resembles the C-O band of PC21, albeit broader. Nevertheless, micro-IRRAS features an objective that can take high-resolution snapshots of the surface of the tribofilm. Comparing the snapshot of the surface of the sample containing the mixture, with the one taken on the surface only containing BB22, it can clearly be observed that the phosphate layer has not formed (Fig. 3.12).
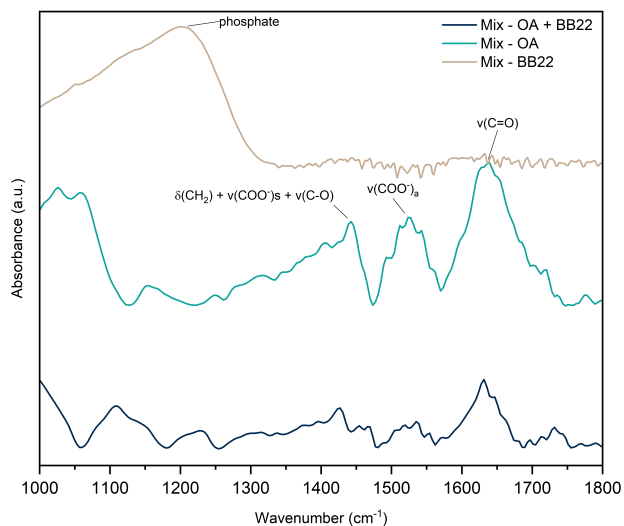
Figure 3.10: *micro-IRRAS spectrum recorded on the MTM sample that was immersed in a lubricant containing both OA and BB22 (black), and of adsorbed OA and BB22 (blue and brown, respectively), in the section affected by the tribological tests.*
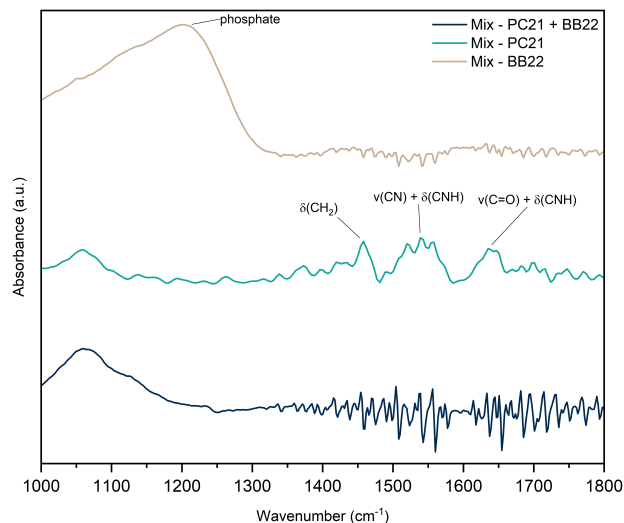

Figure 3.11: *micro-IRRAS spectrum recorded on the MTM sample that was immersed in a lubricant containing both PC21 and BB22 (black), and of adsorbed PC21 and BB22 (blue and brown, respectively), in the section affected by the tribological tests.*
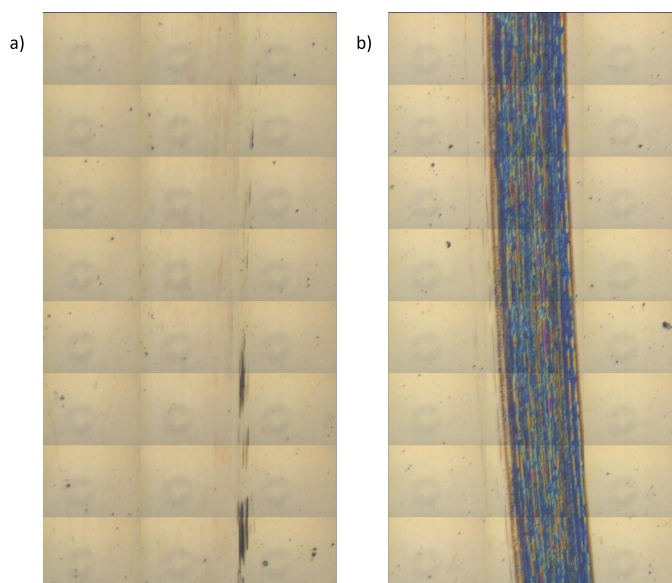
Figure 3.12: *Snapshots on the section affected by the tribological tests of an MTM sample containing: a) both PC21 and BB22; b) BB22 only.*

3.2.3 competition between friction modifiers and detergent

In the same way, as done in the last section, we investigate the competitive adsorption process in two mixtures containing 1% of either OA or PC21 and 1% of detergent. The detergent used in this case is XCA03, a calcium calixarenate that causes the adsorption of a carbonate layer on the surface of the steel. In Fig. 3.13, the ATR spectrum of XCA03 is compared to its micro-IRRAS spectrum, when adsorbed on steel. In this case, carbonate bands do not show any shift. However, the carbonate peak at $\sim$1540 cm^{-1} is slightly narrower. The micro-IRRAS spectra of the adsorbed mixture of
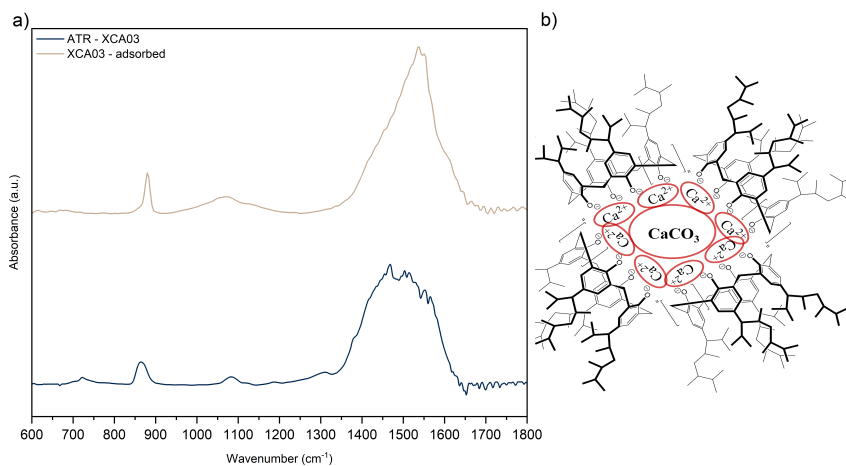

Figure 3.13: *a) micro-IRRAS spectrum of XCA03 adsorbed on the MTM sample, in the section affected by the tribological tests, and ATR spectrum of XCA03 sample (liquid). b) Molecular structure of XCA03.*

OA and XCA03 (1% wt. each) clearly show the predominance of XCA03 in the adsorption process (Fig. 3.14). Conversely, when XCA03 is in the lubricant mixture with PC21, the result is the opposite. As shown in Fig. 3.15, PC21 is predominantly adsorbed on the surface.

Figure 3.14: *micro-IRRAS spectrum recorded on the MTM sample that was immersed in a lubricant containing both OA and XCA03 (black), in the section affected by the tribological tests, and micro-IRRAS spectra of adsorbed OA and XCA03 (blue and brown, respectively).*
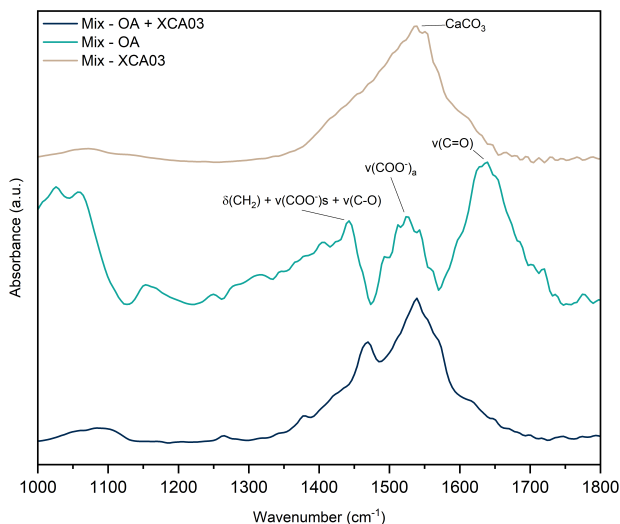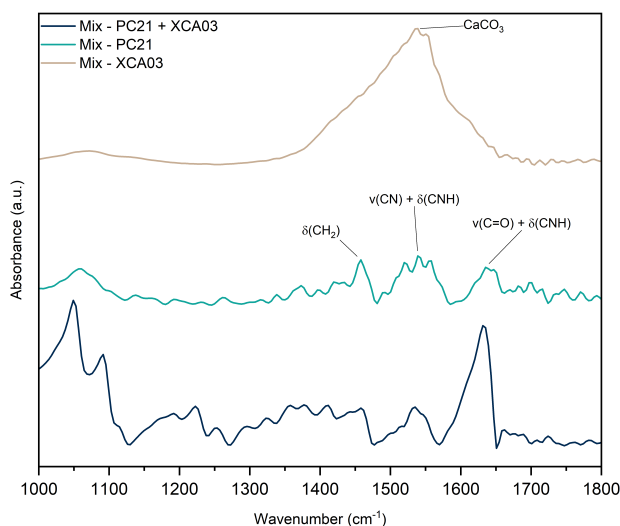

Figure 3.15: *micro-IRRAS spectrum recorded on the MTM sample that was immersed in a lubricant containing both PC21 and XCA03 (black), in the section affected by the tribological tests, and micro-IRRAS spectra of adsorbed PC21 and XCA03 (blue and brown, respectively).*

3.2.4 Competition between friction modifiers and dispersants

Dispersants are also involved in adsorption on the steel surface Therefore, the competition process occurring at the surface will result in variation in the friction performances of the formulated lubricant. In this case, previous investigations done in the R& D laboratories of Eni S.p.a. found that lubricant mixtures containing PC21 and XTJ785 showed diametrically opposite friction performances when containing the same concentrations of two dispersants: XD23, and XD18. PC21 seems to improve its friction performance when substituting XD23 with XD18 in the mixture, while XTJ785 shows worse friction performance. These dispersants are composed of the same central core, while the numbers 23, and 18 represent the molecular weight of the PIB section. Before the comparative micro-IRRAS analysis of the adsorbed mixtures, the dispersants have been characterized singularly by ATR. Unfortunately, the micro-IRRAS spectra of samples immersed in lubricants containing only the dispersant were not available. Therefore, the micro-IRRAS signal of the mixed sample will be compared with the ATR spectra of the dispersants. In Fig. 3.16, the ATR spectra of the two dispersants, XD23 and XD18, are shown. The normalized spectra are co-incident with each other, although there is a difference in the intensity of the band at ~ 1701 cm^{-1}, which is assigned to the C=O groups. Their intensity is reduced in XD23 as the molecular weight of the PIB section is increased, resulting in a lower relative intensity with respect to the rest of the bands. The spectra are then used to comparatively analyze the adsorp-
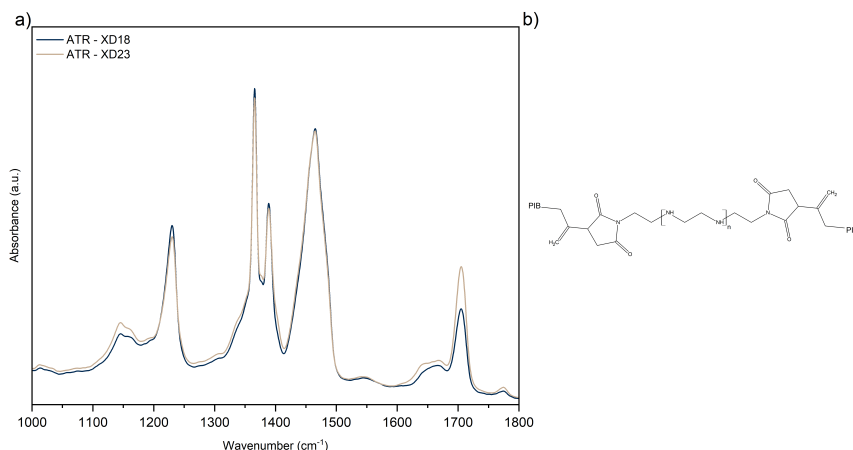

Figure 3.16: *a) ATR spectra of XD23 (black) and XD18 (brown) liquid phase sample. b) Molecular structure of the dispersant.*

tion on the ternary samples containing the friction modifier, together with the dispersant. In Fig. 3.17, the spectra of the ternary samples containing the dispersants and XTJ785, show that the dispersant is more likely to be the one adsorbed preferentially on the surface, and this behavior is more prominent lowering its molecular weight. This may explain the worsening of the friction performances of XTJ785 when mixed with dispersants of lower molecular weights. Instead, when PC21 is mixed in with the dispersants, instead. Fig. 3.18 shows that when decreasing the molecular weight of the dispersant, PC21 can adsorb more reliably on the surface, resulting in an actual increase in performance.

Figure 3.17: *From bottom to top: micro-IRRAS spectrum recorded on the MTM sample that was immersed in a lubricant containing both XTJ785 and XD23, in the section affected by the tribological tests; micro-IRRAS spectrum recorded on the MTM sample that was immersed in a lubricant containing both XTJ785 and XD18, in the section affected by the tribological tests; micro-IRRAS spectrum recorded on the MTM sample that was immersed in a lubricant containing only XTJ785, in the section affected by the tribological tests; ATR spectrum of a liquid sample of XD18.*
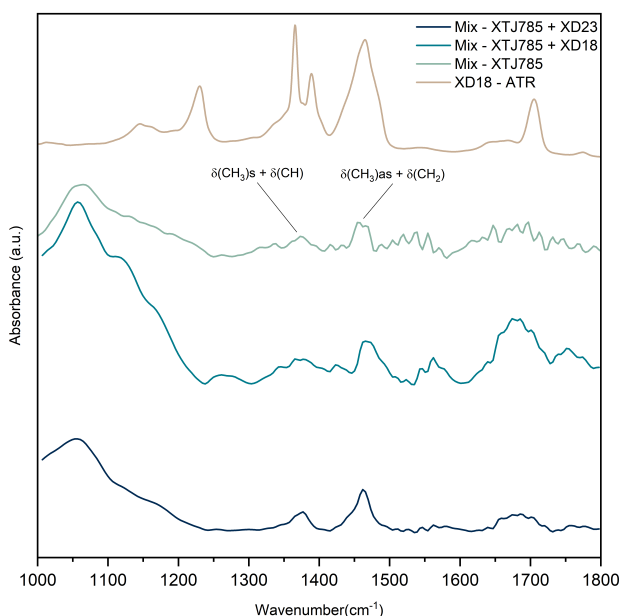
Figure 3.18: *From bottom to top: micro-IRRAS spectrum recorded on the MTM sample that was immersed in a lubricant containing both PC21 and XD23, in the section affected by the tribological tests; micro-IRRAS spectrum recorded on the MTM sample that was immersed in a lubricant containing both PC21 and XD18, in the section affected by the tribological tests; micro-IRRAS spectrum recorded on the MTM sample that was immersed in a lubricant containing only PC21, in the section affected by the tribological tests; ATR spectrum of a liquid sample of XD18.*
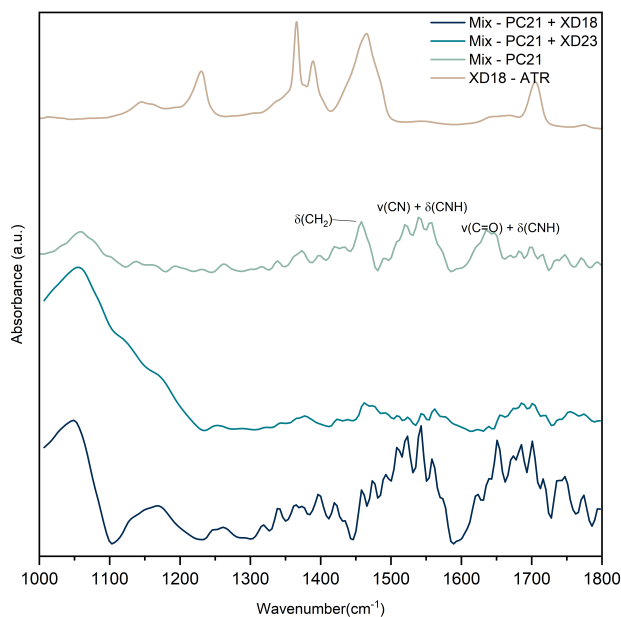
3.3 Conclusions

In this chapter, the adsorption of OFMs on steel surfaces has been examined. Vibrational micro-IRRAS spectroscopy has been used to investigate the competition process at the surface among lubricant additives that adsorb on the surface in complex lubricant mixtures. We found that the OFMs indeed adsorb on the surface through the headgroups, as shown by the clear shifts of the headgroup vibrational modes in the micro-IRRAS spectra with respect to the IR spectra of the OFMs in the liquid phase. This is a remarkable feat, given the monomolecular size of the adsorbed tribofilm and the setup used. At the same time, it is clear how the experimental characterization alone is not sufficient to fully reconstruct the adsorption process and give a definite answer to the configuration of the OFMs on the surface of the steel. This aspect will be tackled in the next chapter with the aid of computational DFT and DFT-MD methods. The spectroscopic micro-IRRAS technique has also been used to investigate competition processes in lubricant formulation comprising more than one additive adsorbing on the steel surface. Competition is a highly complex problem, where many variables can affect the outcome of the adsorption process. Molecular orientation and interactions between the additive molecules in the lubricant and on the surface are only a few examples of variables that must be taken into account and that the present technique cannot resolve at this stage. However, we were still able to gain important information about the competition process result, i.e. which additive is mostly adsorbed on the surface given a specific mixture composition. In the case of adsorption of XTJ785 and PC21 in mixture with dispersants, we found that efficient adsorption of OFM results in a marked improvement of friction reduction properties of the lubricant, in agreement with the tribological measurements. This is a great aid in finding the optimal lubricant composition to achieve the maximum result out of every additive included, as having the knowledge of which additive adsorbs the most on the surface is a crucial information that can be used to tune the composition of the lubrication for specific uses.

DFT interpretation of OFM adsorption

4.1 Interpretation of the adsorption configurations of OFMs by DFT

In the previous chapter it was demonstrated how the result of the adsorption is shown in the IRRAS spectra in the modification of the bands corresponding to the modes belonging to the polar head of the OFM. To determine how the chemical interaction of the polar head of the OFMs with hematite affects the headgroup bands, DFT calculations with CRYSTAL17 with boundary conditions applied of the equilibrium structure and associated IR spectra of the adsorbed molecules on the surface of hematite have been performed. As discussed in Ch. 2 the structural and electronic properties of the polar head are the only aspect involved in the adsorption of the OFMs on the metllic surface. By consequence, we expect that its infrared spectrum is only weakly affected by the alkyl chain length. For these reason, we decided to perform the calculations on C_6 versions of the original OFMs (which are C_{18}), greatly simplifying the problem, meanwhile also sharply reducing computational costs. In all calculations, the OFM molecule is placed at an arbitrary distance from the hematite surface (close enough for the molecule to "feel the presence" of the surface) and the adsorption process is let hap-

pen spontaneously. Details regarding the CRYSTAL17 calculations can be found in Appendix A.1.

Oleic Acid [37]

We compare in Fig. 4.2 the experimental micro-IRRAS spectrum of OA with the calculated IR spectra associated with the monodentate (Fig. 4.1a) and bidentate bridging (Fig. 4.1b) configurations of hexanoic acid (the C_6 counterpart to OA). The list of the relevant peaks and their assignments is shown in Table 4.1. Based on the comparison between the experimen-
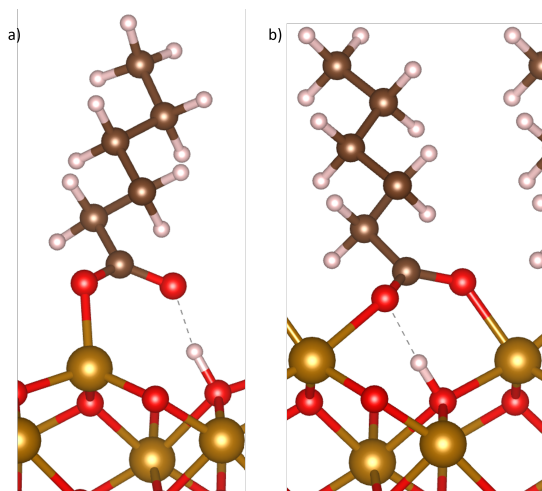

Figure 4.1: *a) Snapshot of the final geometry of hexanoic acid in the monodentate configuration on the surface of hematite, and b) Snapshot of the final geometry of hexanoic acid in the bidentate bridging configuration on the surface of hematite. Atoms shown in the models: Hydrogen (white), carbon (gray), oxygen (red), and iron (orange).*

tal spectrum and the simulated spectra, we can straightforwardly assign the peak at 1524 cm^{-1} (IRRAS) to the computed band at 1532 cm^{-1} that corresponds to the -COO asymmetric stretching of the bridging configuration. In a similar way, we assign the IRRAS peak at 1646 cm^{-1} to the C=O stretching of the monodentate configuration, which is found at 1602 cm^{-1} in the simulated spectrum. The 1444 cm^{-1} peak of the IRRAS spectrum corresponds to the 1457 cm^{-1} peak that is observed in the calculated spectra of the monodentate and bridging configuration (Fig. 4.2). This is assigned to the scissoring mode of the CH$_2$ group adjacent to the acid head, with some contributions from the -COO symmetric stretching (bridging con-

Table 4.1: *List of vibrational modes and assignation of adsorbed oleic acid. Experimental micro-IRRAS, calculated monodentate model and bridging model. *non-interacting on the hematite surface.*

Wavenumber (cm^{-1})	Experimental	Calculated - Monodentate	Calculated - Bridging
1444	$\delta(CH_2)$ + v(CO) + v(COO^-)s	-	-
1457	-	$\delta(CH_2)$ + v(CO)	$\delta(CH_2)$ + v(COO^-)s
1524	v(COO^-)as	-	-
1532	-	-	v(COO^-)as
1602	-	v(C=O)	-
1646	v(C=O)	-	-
1710	v(C=O)*	-	-

figuration) or from the CO stretching (monodentate configuration). The peaks found in the calculated spectra follow Crowell's empirical rule [110] which assigns the signals in the IR spectrum by calculating the distance between the asymmetric and symmetric -COO stretching (which is about 80 cm cm^{-1} for bridging coordination) or the distance between the C=O and CO stretching (which is about 200 cm^{-1} for monodentate coordination). Indeed, Crowell's distances are 80 cm^{-1} in the bridging model, and 202 cm^{-1} in the monodentate model. Finally, the presence in the IRRAS spectrum of a shoulder at about 1710 cm^{-1} suggests the presence in the tribofilm of oleic acid molecules not interacting with the surface through their polar head; such molecules may get stuck in the SAM during the tribological tests. The analysis of the IRRAS spectrum discussed above suggests that both monodentate and bridging configurations are present in the adsorbed layer. This is confirmed by the very close electronic adsorption energies calculated for the two models: $\Delta E_{ads,monodentate} = -82.6$ kcal/mol, $\Delta E_{ads,bridging} = -83.5$ kcal/mol (see Appendix A.1. for computational details). Within the expected accuracy of DFT, such values can be considered almost isoenergetic.
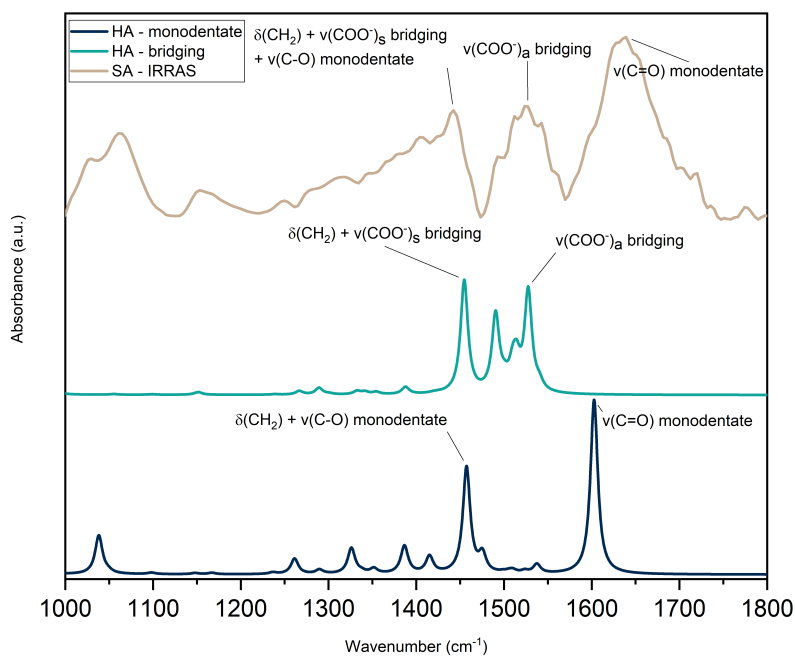
Figure 4.2: *Micro-IRRAS spectrum of the of oleic acid adsorbed on the MTM sample, in the section affected by the tribological tests, and calculated IR spectra of hexanoic acid adsorbed on hematite in the monodentate and bridging structures (scale factor: 0.99).*

Oleic Amide

As discussed in Chapter 3, the adsorption of oleic amide on the surface of hematite results in the rise of two new bands in the 1500 -1600 cm^{-1} region. In Fig. 4.4 the experimental micro-IRRAS spectrum of adsorbed oleic amide is compared with the calculated spectra of two possible configurations that the molecule can assume on the surface. In the monodentate coordination (Fig. 4.3a), there is no deprotonation of the molecule. However, the oxygen of the C=O of the headgroup coordinates with the iron at the surface of the hematite. This results in great shifts of the modes of the
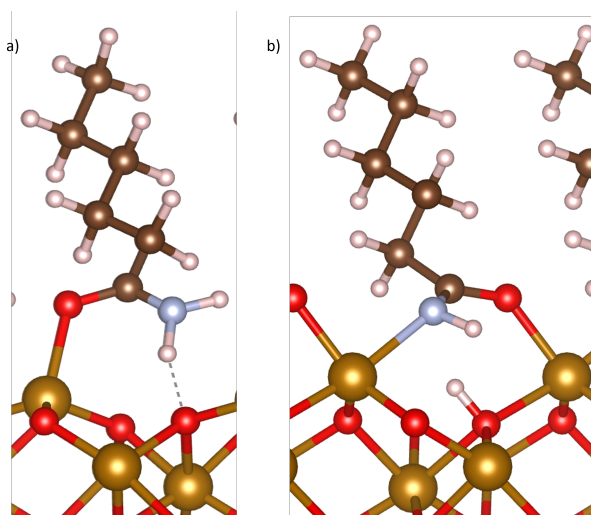

Figure 4.3: *a) Snapshot of the final geometry of hexanoic amide in the monodentate configuration on the surface of hematite, and b) Optimized geometry of hexanoic amide in the bidentate bridging configuration on the surface of hematite. Atoms shown in the models: Hydrogen (white), carbon (gray), nitrogen (blue), oxygen (red), and iron (orange).*

OAm headgroup. The band at 1670 cm^{-1} that belongs to the v(C=O) in the liquid phase is replaced by a simultaneous stretching-scissoring of the NH$_2$ group (1665 cm^{-1} - model). The double bond involving the C and the O of the headgroup is now redistributed along the CNO group due to the interaction with the surface iron. This gives rise to an asymmetric v(CNO) (1588 cm^{-1} - model) which is assigned to the band at 1627 cm^{-1} in the experimental spectra, that also involves the scissoring of the NH$_2$ group. Finally, the symmetric v(CNO) stretchings (1457 and 1475 cm^{-1} - model) are assigned to the band at 1473 cm^{-1} in the experimental spectra. The v(CNO) stretching at 1457 cm^{-1} is mixed with the scissoring of the CH$_2$

group adjacent to the headgroup. The bidentate bridging coordination (Fig. 4.3b) conversely shows deprotonation of the NH_2 group, resulting in the formation of an NH group, and the N atom forms a bond to a surface iron. This gives rise to two bands at 1526 cm^{-1} and 1546 cm^{-1} (model) that correspond to the stretchings of the CN bond. These are straightforwardly assigned to the experimental bands at 1538 cm^{-1} and 1573 cm^{-1} given their remarkable accordance in terms of relative intensity. In the bidentate bridging configuration, the charge of the C=O double bond is not redistributed as in the monodentate configuration. However, some double bond character is still lost, giving rise to a CO stretching band at 1457 cm^{-1} (mixed the δNH and the δCH_2 adjacent to the headgroup) . This is assigned to the band at 1473 cm^{-1} in the experimental spectrum. The list of all assigned vibrational modes is reported in Tab. 4.2. It is important to note that the band at 1423 cm^{-1} has not been assigned and it is not found in the calculated spectra. We believe that this and the band at 1473 cm^{-1} (in part) may arise from a possible not complete wash of the ETROIV base oil from the MTM sample. This is supposed since the profile of the peak at 1473 cm^{-1} clearly resembles the peak found in the IR spectrum of ETROIV (Fig. 4.4).

Table 4.2: *List of vibrational modes and assignation of adsorbed oleic amide. Experimental micro-IRRAS, calculated monodentate model and bridging model.*

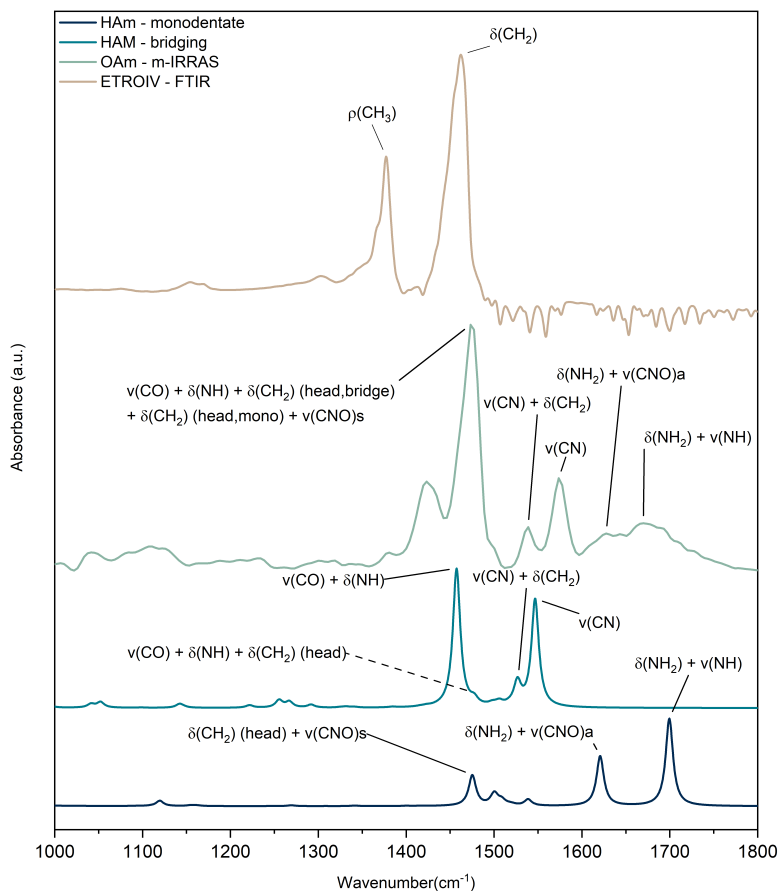| Wavenumber (cm^{-1})	Experimental	Calculated - Monodentate	Calculated - Bridging
1457	-	-	δ(CNH) + v(CO)
1473	δ(CNH) + v(CO) + δ(CH$_2$)$_{head}$(bridging) + δ(CH$_2$)$_{head}$(monodentate) + v(CNO)s	-	-
1475	-	v(CNO)s + δ(CH$_2$)$_{head}$	δ(CNH) + v(CO) + δ(CH$_2$)$_{head}$
1526	-	-	v(CN) + δ(CH$_2$)$_{chain}$
1538	v(CN) + δ(CH$_2$)$_{chain}$	-	-
1546	-	-	v(CN)
1573	v(CN)	-	-
1588	-	δ(NH$_2$) + v(CNO)as	-
1627	δ(NH$_2$) + v(CNO)as	-	-
1665	-	δ(NH$_2$) + v(CN)	-
1670	δ(NH$_2$) + v(CN)	-	-

Figure 4.4: *Micro-IRRAS spectrum of the of oleic amide adsorbed on the MTM sample, in the section affected by the tribological tests, calculated IR spectra of hexanoic amide adsorbed on hematite in the monodentate and bridging structures (scale factor: 0.99), and FT-IR spectrum of the of ETROIV sample (liquid phase).*

Glycerol mono Oleate

GMO adsorbs on the surface of hematite forming a bidentate chelate configuration (Fig. 4.5), where the terminal oxygens of the OFM head coordinate with a single iron site of the surface. This produces a shift of the ν(C=O) band to 1670 cm^{-1} (with respect to the ν(C=O) band of GMO in liquid phase) that is found at 1688 cm^{-1} in the calculated spectrum. The bands at 1492 cm^{-1} and 1454 cm^{-1} are assigned to the δCH$_2$, the former involving all the alkyl chain and the headgroup of the molecule, the latter only involving the CH$_2$ in the headgroup and on the first carbon of the alkyl chain. It is worth noticing, there are significant differences in intesities between the band in the experimental spectrum and the bands in the calculated one. This is most likely a product of orientational effects on the surface. As discussed previously in chapter 2, micro-IRRAS is selective with respect to the orientation of the transition dipole moment of the vibrational modes respective to the metallic surface.
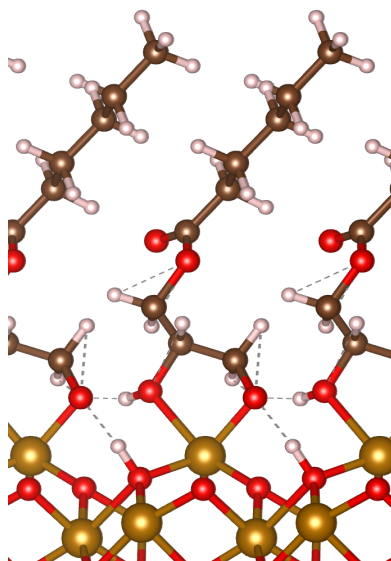
Figure 4.5: *Optimized geometry of glycerol mono hexanoate in the bidentate chelate configuration on the surface of hematite. Atoms shown in the models: Hydrogen (white), carbon (gray), oxygen (red), and iron (orange).*

Table 4.3: *List of vibrational modes and assignation of adsorbed GMO. Experimental micro-IRRAS, calculated monodentate model.*

Wavenumber (cm^{-1})	Experimental	Calculated - Bidentate Chelate
1440	-	$\delta(CH_2)$(head)
1447	-	$\delta(CH_2)$(ester)
1454	$\delta(CH_2)$(head) + $\delta(CH_2)$(ester)	-
1476	-	$\delta(CH_2)$(all)
1492	$\delta(CH_2)$(all)	-
1493	-	$\delta(CH_2)$(all)
1670	ν(C=O)	-
1688	-	ν(C=O)

Figure 4.6: *Micro-IRRAS spectrum of the of GMO adsorbed on the MTM sample, in the section affected by the tribological tests, and calculated spectra of glycerol mono hexanoate adsorbed on hematite in the bidentate chelate configuration (scale factor: 0.97).*

59

XTJ785

In Fig. 4.8, the experimental micro-IRRAS spectrum is compared with the calculated spectrum of XTJ785(C_6) adsorbed on hematite in monodentate coordination (Fig. 4.7). Due to the very large headgroup, this was the only possible coordination that was available to form an ordered monolayer. Moreover, there is no deprotonation of the headgroup upon adsorption. The experimental spectra are quite noisy for the reasons discussed in chapter 2. Nonetheless, we have been able to provide an assignment for this case (a list of all assigned vibrational modes is shown in Tab. 4.5). The adsorption of XTJ785 on the surface of steel gives rise to a large band peaked at 1060 cm^{-1}. This band is so broad that it encompasses many of the vibrational modes found in the monodentate model. It was therefore assigned to the stretchings of the CN, CO, and CC bonds, which are found in the calculated spectrum in the 1100 - 1200 cm^{-1} region. The band at 1362 cm^{-1} (model) that belongs to the symmetric umbrella motion of the CH$_3$ present in the headgroup and the CH bending was assigned to the band at 1373 cm^{-1} in the experimental spectrum. In the same way, the band at 1464 cm^{-1} (model) which belongs to the asymmetric umbrella motion of the CH$_3$ present in the headgroup, and the scissoring of the CH$_2$ of the headgroup was assigned to the band at 1457 cm^{-1} of the experimental spectrum. The monodentate model also shows a sharp band at 1616 cm^{-1}. This band is not found in the experimental spectrum, most likely due to the heavy noise present, and it is produced by the COH bending in the CO terminations of the headgroup.

Table 4.4: *List of vibrational modes and assignation of adsorbed XTJ785. Experimental micro-IRRAS, calculated monodentate model.*

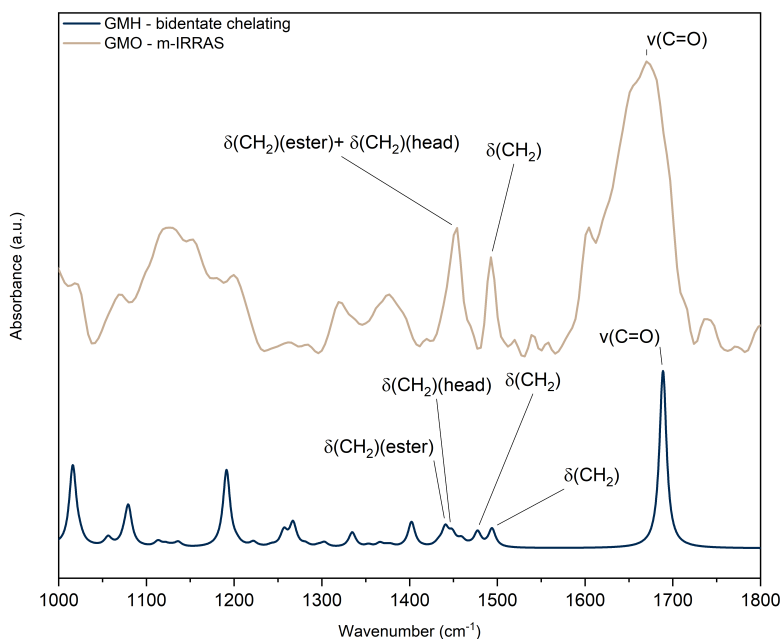| Wavenumber (cm^{-1})	Experimental	Calculated - Monodentate
1060 (large band)	ν(CN), ν(CO), ν(CC)	-
1100 - 1200	-	ν(CN), ν(CO), ν(CC)
1362	-	δ(CH$_3$)s + δ(CH)
1373	δ(CH$_3$)s + δ(CH)	-
1457	δ(CH$_3$)as + δ(CH$_2$)	-
1464	-	δ(CH$_3$)as + δ(CH$_2$)
1616	-	δ(COH)
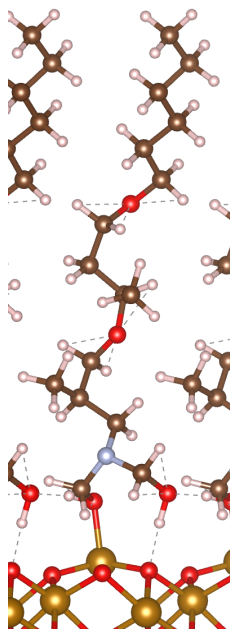
Figure 4.7: *Optimized geometry of the C_6 representation of XTJ785 in the monodentate configuration on the surface of hematite. Atoms shown in the models: Hydrogen (white), carbon (gray), oxygen (red), and iron (orange).*
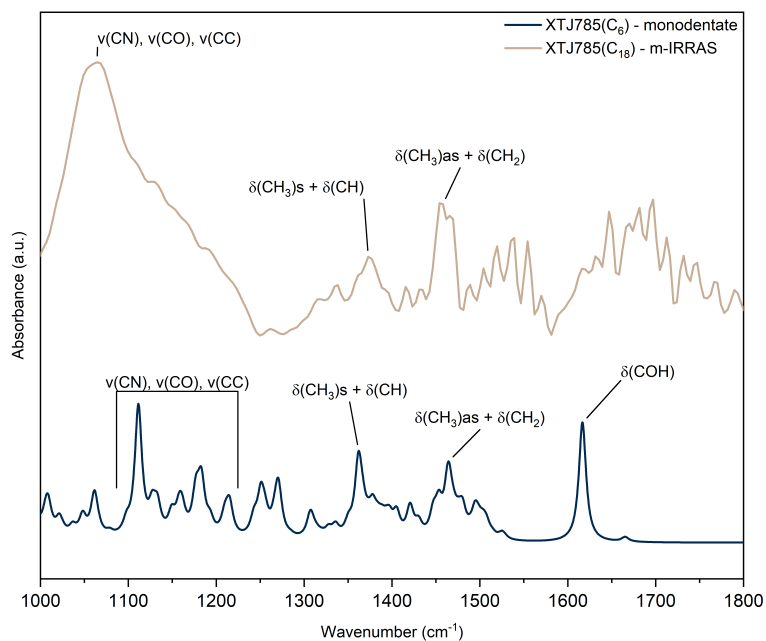
Figure 4.8: *Micro-IRRAS spectrum of the of XTJ785 adsorbed on the MTM sample, in the section affected by the tribological tests, and calculated spectra of XTJ785(C_6) adsorbed on hematite in the monodentate structure (scale factor: 0.98).*

4.1. Interpretation of the adsorption configurations of OFMs by DFT

PC21

In Fig. 4.10, the experimental micro-IRRAS spectrum of adsorbed PC21 is compared with the calculated spectrum of PC21(C_6) adsorbed on hematite in bidentate chelate coordination (Fig. 4.9). Adsorption in this case involves the deprotonation of the headgroup at one of the oxygen of the -C_3OO termination. The two oxygen of this group then interact together with an iron atom at the surface of hematite. The C=O of the headgroup interestingly forms a hydrogen bond with the -NH group of an adjacent molecule, increasing the stability of the layer (this is further discussed in the next chapter). Comparing the experimental spectrum with the calculated one, the band at 1635 cm^{-1} in the experimental spectrum was assigned to the stretching of the C=O bond which is mixed with the bending motion of the CNH group (1594 cm^{-1} in the model). In the same way, the peak at 1538 cm^{-1} is assigned to the stretching of the CN bond plus the CNH bending motion (1551 cm^{-1} in the model). The signal of adsorbed PC21 shows a relatively small change with respect to the spectrum of its liquid phase. This could be because the hydrogen bonding between the C=O and the -NH group of two different molecules is not changed upon adsorption. A change can be observed in the rather wide band at 1056 cm^{-1}. This was assigned through the model to the stretching modes of the -CO, -CN groups of the head of the molecule. To this band also belong the CC stretchings of the alkyl chain.

Table 4.5: *List of vibrational modes and assignation of adsorbed PC21. Experimental micro-IRRAS, calculated monodentate model.*

| Wavenumber (cm^{-1})	Experimental	Calculated - Bidentate Chelate
1056 (large band)	ν(CN), ν(CO), ν(CC)	-
1000 - 1100	-	ν(CN), ν(CO), ν(CC)
1425	-	δ(CH$_2$)(ester) + δ(CH$_2$)(head)
1454	-	δ(CH$_2$)(chain) + δ(CH$_2$)(head)
1457	δ(CH$_2$)(chain) + δ(CH$_2$)(head)	-
1470	-	δ(CH$_2$)(chain)
1538	ν(CN) + δ(CNH)	-
1551	-	ν(CN) + δ(CNH)
1594	-	ν(C=O) + δ(CNH)
1635	ν(C=O) + δ(CNH)	-

Figure 4.9: *Optimized geometry of the C_6 representation of PC21 in the bidentate chelate configuration on the surface of hematite. Atoms shown in the models: Hydrogen (white), carbon (gray), oxygen (red), and iron (orange).*
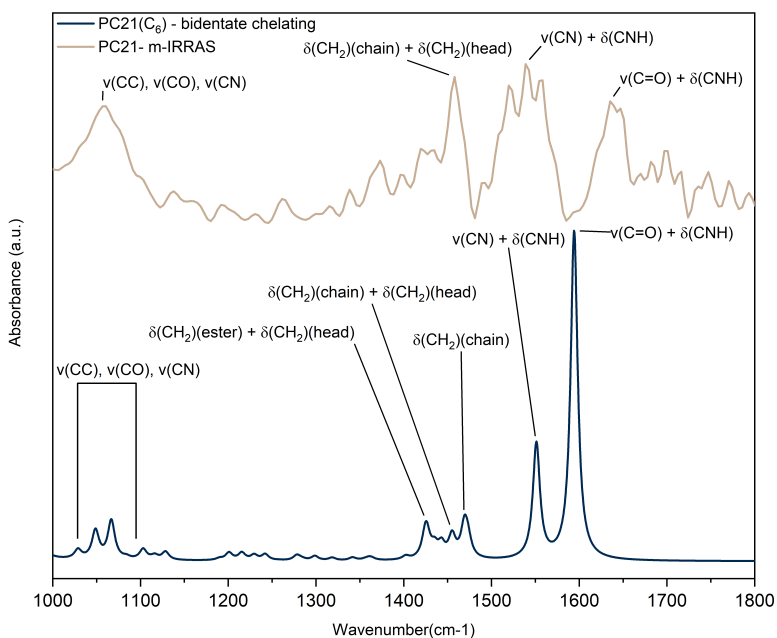
Figure 4.10: *Micro-IRRAS spectrum of the of PC21 adsorbed on the MTM sample, in the section affected by the tribological tests, and calculated spectra of PC21(C_6) adsorbed on hematite in the bidentate chelate structure (scale factor: 0.96).*

4.2 Interpretation of micro-IRRAS spectra before and after friction

As discussed in Ch. 2., micro-IRRAS was used to record spectra of the adsorbed OFMs inside the wear track produced by the tribotest on the MTM sample. This allowed to record a signal only coming from the area subjected to friction and assess its effect on the adsorption state of the OFMs. To complete the spectroscopic analysis of the tribofilm, we compare the spectra inside the track with the signal coming from outside the wear track, which has not been subjected to tribological contact. Because of the required spatial resolution, this is a feature only micro-IRRAS could achieve. The friction modifier is adsorbed in the same starting conditions in both positions, but only the SAM inside the track is subjected to the mechanical stress applied by the friction test, whereas the SAM outside of the wear is not affected by the test. Therefore, any spectroscopic change observed between the spectra acquired inside and outside of the wear track can be ascribed to the effect of friction during the tribotest. By considering a simplified planar model of the surface that neglects rugosity, the tilt angle of the chain axis with respect to the surface is the main geometric parameter that can describe the orientation of the molecules in the SAM. In the interpretation of the micro-IRRAS data, we assume that the thickness of the oxide layer is thin enough so that its dielectric constant does not play a major role in determining IRRAS relative intensities. [63] This is reasonable since the literature reports that the typical oxide layer on top of steel is only a few nanometers thick, which is much smaller that the wavelength range of the IR light used in the IRRAS experiments. [111] Therefore, based on the selection rule of IRRAS on metals, which enhances the component of the transition dipole normal to the surface, we can provide simple geometrical interpretations of the changes in the relative intensities of the peak before and after the tribotest. Changes in relative intensity suggest that the z-projection of the transition dipole moment has increased/decreased, meaning that the molecules adsorbed on the surface have changed their angle with respect to the normal to the surface of steel. All the spectra discussed in this analysis will be shown with baseline correction, without normalization.

OA [37]

In Fig. 4.11, the spectra of adsorbed OA inside and outside the wear track produced by the MTM tribological test are compared. Firstly, no significant

shift in the band position is observed. However, significant changes in the relative intensity of the IR bands are observed. The remarkable increase of the intensity of the δCH_2 scissoring peak at 1444 cm^{-1} which is observed in the spectrum of the tribofilm inside the wear track suggests that the applied mechanical stress is affecting the tilt angle in such a way to push the molecules towards the surface, i.e., from a more upright position to a position which complies with the direction of the applied stress. This transition dipole moment of the CH$_2$ scissoring mode is perpendicular to the molecular axis. Meanwhile, the -COO symmetric stretching is almost perfectly parallel to the surface during the tilt of the molecule. After tilting, the CH$_2$ scissoring mode has a sizeable projection orthogonally to the surface after the tribotest, which implies a larger IRRAS intensity. This interpretation is corroborated by the concurrent decrease of the IRRAS intensity of the C=O stretching at 1646 cm^{-1}, whose transition dipole is oriented so that its component normal to the surface decreases. Our interpretation of the IRRAS intensity data based on changes of the molecular orientation in the SAM is also consistent with the results of molecular dynamics simulations of the tribofilm, which predict this molecular behavior caused by the applied mechanical stress (see chapter 6). To corroborate the interpretation
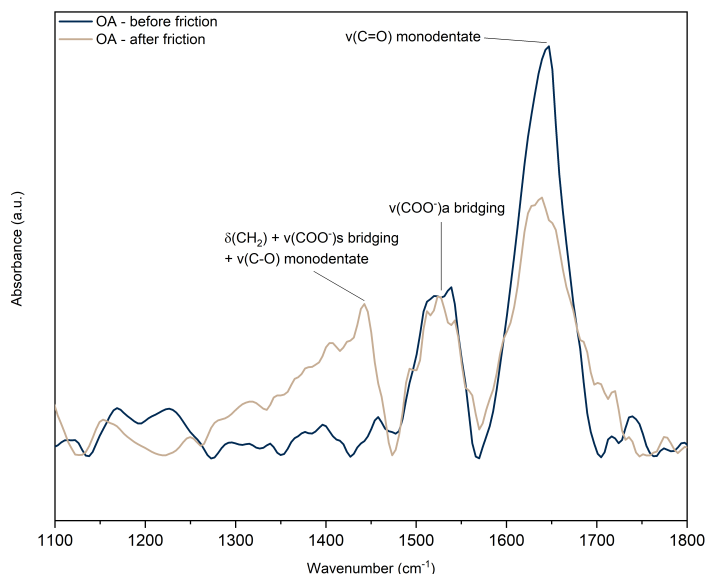

Figure 4.11: *Micro-IRRAS spectrum of the of OA adsorbed on the MTM sample, in the section affected by the tribological tests (yellow), and outside the section affected by the tribological tests (black). All spectra are shown after correction of the baseline, without normalization.*

given above, polarized spectra have been calculated from the DFT models as discussed in section 2.6.1. The procedure consisted in generating a vector v on which the transition dipole moment matrix can be projected. From this projection, a new IR spectrum can be calculated that only takes into account the dipole moments oriented with the generated vector. By changing the angle of the generated vector with respect to the surface of the metal (in the models), IR spectra at a different angle can be computed. This was done at angles from 0 to 45 at steps of 5 for both monodentate and bidentate bridging configurations. The final spectra were obtained by summation of the spectra obtained from the single configuration at the same angle. In Fig. 4.12 the computed spectra at angles of 0 and 20 degrees are reported. The remarkable agreement observed between the relative intensity changes from model to experimental, leads to conclude that the interpretation of the IRRAS spectra is correct.
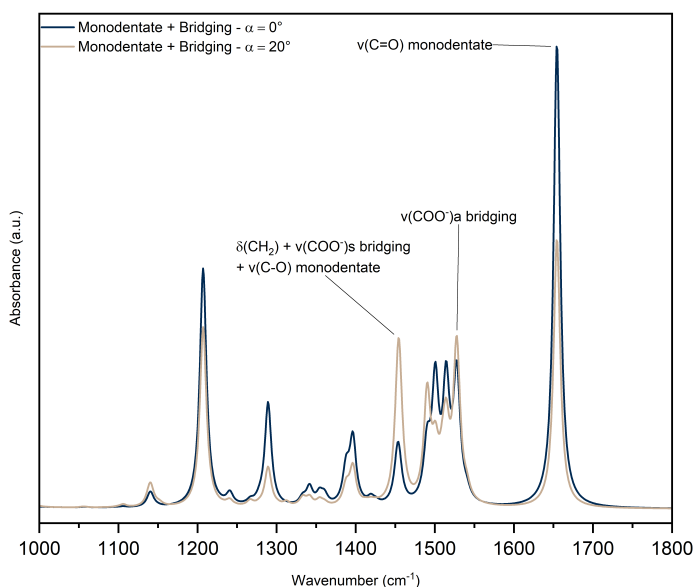

Figure 4.12: *Calculated spectra of hexanoic acid adsorbed on hematite, projected on a vector z at an angle α from the normal to the hematite surface. Each spectrum was obtained as a sum of the spectra calculated from the monodentate and bidentate bridging configurations.*

OAm

In Fig 4.13 the spectra of adsorbed OAm inside and outside the wear track produced by the MTM tribological test are compared. As in the previous case, no significant shift in the band position is observed. However, again, significant changes in the relative intensity of the IR bands are observed. The band at 1473 cm^{-1} increases in intensity, as well as the two bands at 1538 cm^{-1} and 1573 cm^{-1}. The bands at 1627 cm^{-1} and 1670 cm^{-1} seem to not be present before the tribotest, and they appear in the spectra recorded in the wear track. The same method used before was applied in this case to

Figure 4.13: *Micro-IRRAS spectrum of the of OAm adsorbed on the MTM sample, in the section affected by the tribological tests (yellow), and outside the section affected by the tribological tests (black). All spectra are shown after correction of the baseline, without normalization.*

help in the interpretation. In Fig. 4.14, the computed polarized spectra at angles of 0 and 30 degrees (z-vector with respect to the normal to the surface) are shown. Comparing them to the experimental spectra, the increase in relative intensity of the bands in the region 1500-1700 cm^{-1} shows good agreement (supposing that some of the intensity is not detected due to the sensitivity limit). The band at 1473 cm^{-1} also increases. However, its relative intensity with respect to the other bands is not in agreement with the experimental spectra. Nevertheless, as discussed earlier when interpreting the adsorption configurations of OAm, this could be caused by the presence

of excess ETROIV in the sample.
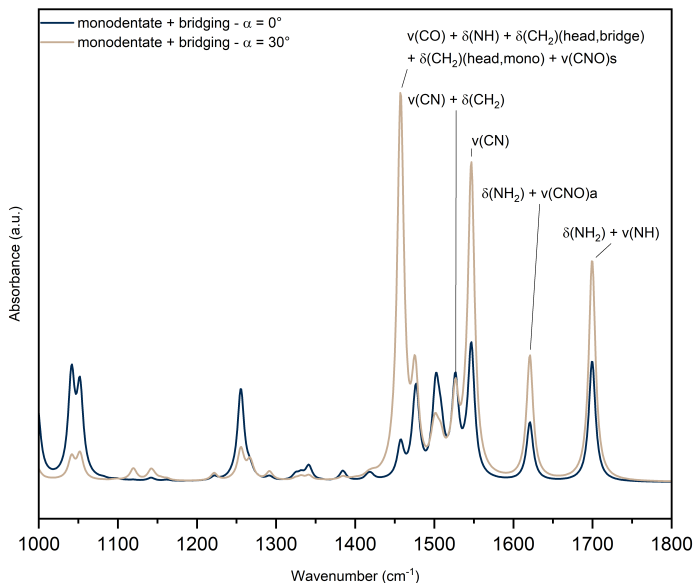
Figure 4.14: *Calculated spectra of oleic amide adsorbed on hematite, projected on a vector z at an angle α from the normal to the hematite surface. Each spectrum was obtained as a sum of the spectra calculated from the monodentate and bidentate bridging configurations.*

70

GMO

Comparing the spectra of GMO adsorbed on hematite before and after the MTM test (Fig. 4.15), there is a clear rise of the ν(C=O) band at 1670 cm^{-1}, not seen in the spectra recorded outside of the wear track. When the molecule is in an upright position, the transition dipole moment of the ν(C=O) is nearly parallel to the surface. As the molecule tilts with its chain axis towards the surfacedue to the tribological contact, the component of the ν(C=O) mode perpendicular to it increases and produce the rise of intensity that s observed in the spectra. The same reasoning can be applied to the scissoring of the CH$_2$ at 1492 cm^{-1}, as its transition dipole moment is also oriented perpendicularly to the alkyl chain. Before the MTM test, only one band at 1461 cm^{-1} is spotted. Moreover, this band seems to slightly shift to 1454 cm^{-1} after the tribotest. Earlier on in the previous chapter, we assigned this band to the scissorings of the CH$_2$ belonging to the ester headgroup and to the first carbon of the alkyl chain. The results of the DFT calculation allow us to expand this description. In the calculated spectrum two distinct peaks slightly separated by 7 cm^{-1} are found, which is the same distance we observe between the two peaks before and after the tribotest. Indeed, the two peaks belong to vibrations with transitions dipole moments perpendicular to each other. It is therefore reasonable that upon tilting, their relative intensities in the spectra follow an opposite evolution. The intensity of the scissorings in the ester group decreases, as its component perpendicular to the surface would progressively get smaller, meanwhile, the scissoring of the first CH$_2$ of the alkyl chain increases. The computed polarized spectra at angles of 0 and 30 degrees (z-vector with respect to the normal to the surface) confirm the interpretation. As it can be observed in Fig. 4.16, the band at 1688 cm^{-1} sharply increases in intensity as the molecule tilts towards the surface. When the molecule is assumed completely perpendicular with respect to the steel surface, the intensity of this band is almost null, demonstrating that initially, the C=O bond is parallel to the surface.
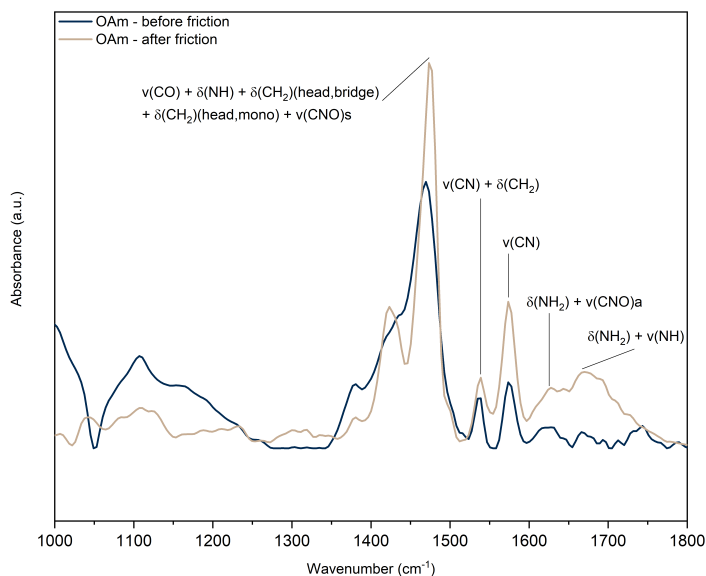
Figure 4.15: *Micro-IRRAS spectrum of GMO adsorbed on the MTM sample, in the section affected by the tribological tests (yellow), and outside the section affected by the tribological tests (black). All spectra are shown after correction of the baseline, without normalization.*
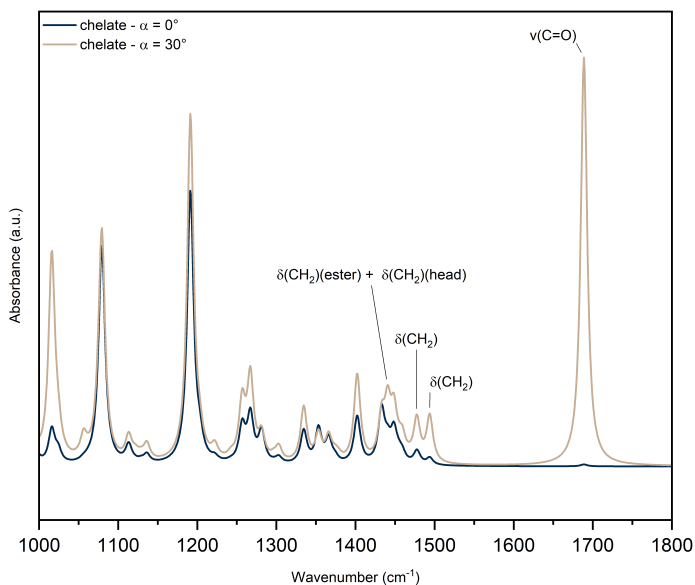
Figure 4.16: *Calculated spectra of glycerol mono oleate adsorbed on hematite, projected on a vector z at an angle α from the normal to the hematite surface.*

XTJ785

Interpreting how the spectrum of XTJ785 is affected by the tribotest revealed to be more straightforward than in the previous cases. In Fig. 4.17 the spectra of adsorbed XTJ785 inside and outside the wear track produced by the MTM tribological test are compared. Since the bands at 1373 and 1457 cm^{-1}, which are produced by $\delta(CH_2)$ modes, possess transition dipole moments oriented perpendicular to the molecular axis, it seems safe to assume that their increase in intensity after the tribotest results from a tilt of the molecule towards the surface.
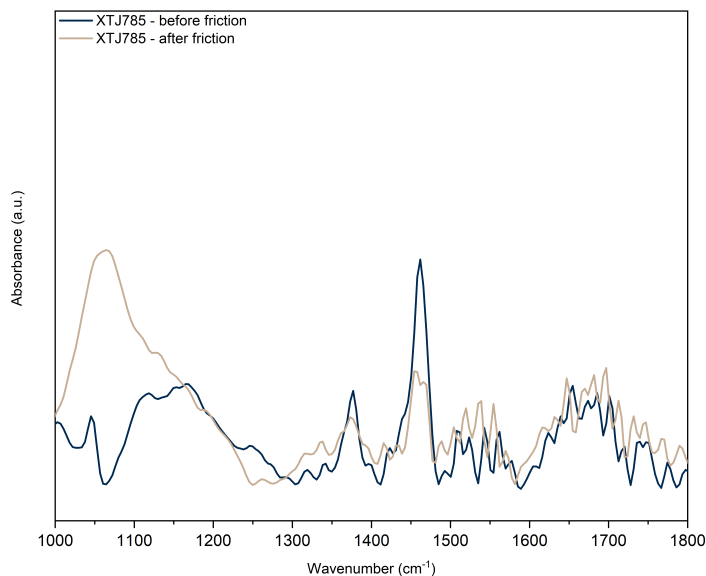
Figure 4.17: *Micro-IRRAS spectrum of the of XTJ785 adsorbed on the MTM sample, in the section affected by the tribological tests (yellow), and outside the section affected by the tribological tests (black). All spectra are shown after correction of the baseline, without normalization.*

PC21

As in the previous case, interpreting how the spectrum of PC21 is affected by the tribotest is also rather straightforward. The bands at 1470 (δ(CH$_2$)), 1538 (v(CN)), and 1635 cm^{-1} (v(C=O)) all increase in intensity in the signal recorded inside the wear track (Fig. 4.18). These vibrational modes have their transition dipole moment oriented perpendicular to the molecular axis. It is then safe to assume also in this case that their increase in intensity after the tribotest results from a tilt of the molecule towards the surface.
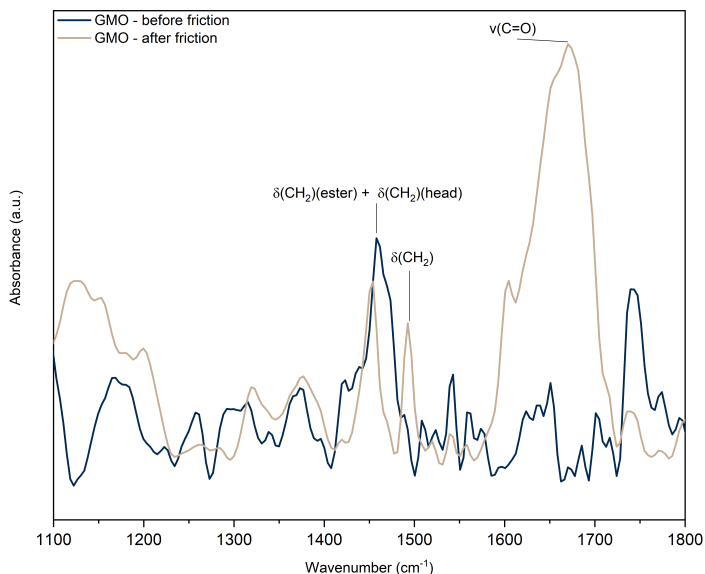

Figure 4.18: *Micro-IRRAS spectrum of PC21 adsorbed on the MTM sample, in the section affected by the tribological tests (yellow), and outside the section affected by the tribological tests (black). All spectra are shown after correction of the baseline, without normalization.*
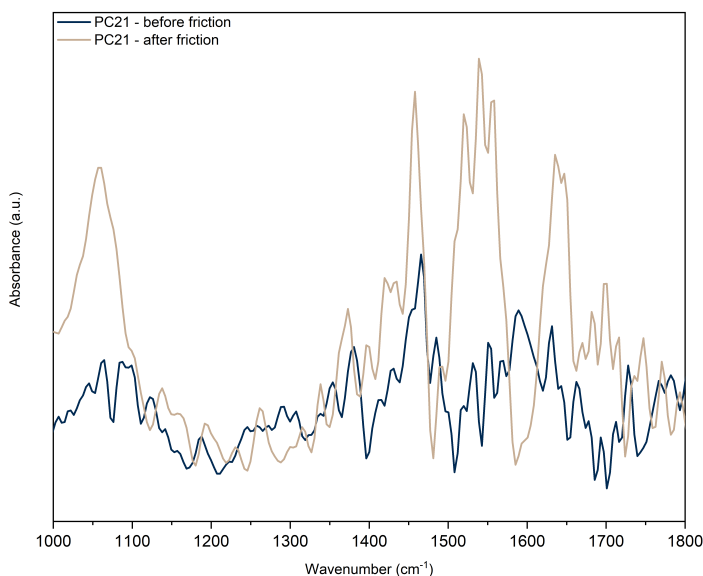
4.3 DFT-MD simulations of molecular disorder

The bands on the micro-IRRAS spectra of the adsorbed OFMs on the wear track are in all cases significantly broad. This could be ascribed to the disorder that occurs due to the thermodynamical molecular arrangement of the tribofilm. To complete the computational interpretation of the micro-IRRAS spectra, taking this disorder into account, DFT-MD models were carried out, and the IR spectra were calculated from the final trajectories as described in section 2.4.2. Since the computational costs involved were very demanding, the discussion is limited to the case of oleic acid. The final optimized CRYSTAL geometry of hexanoic acid in the monodentate configuration on the hematite surface was let evolve for 5 ps at 300 K and 423 K in an NVT ensemble, using a B3LYP functional. The IR spectra were calculated from the evolution of the dipole moment matrix in time. The evolution of the dipole moment in time, when calculating the IR spectra, only the z-component of the matrix was considered. This is because we observed that the dipole moment along the axes on the plane of the hematite slab tends to systematically increase. This could be due to the conductive character of the surface of hematite. However, since IRRAS is much more sensitive in the direction perpendicular to the slab plane, the choice of taking only the z-component of the dipole was considered a better comparison to the IRRAS spectra. A previous set of DFT-MD runs using the BLYP functional was performed, in the hope of reducing computational costs while maintaining a good agreement with the experimental results. However, the BLYP functional proved to not be able to predict correctly the peak position and intensities of the vibrational modes, especially for what concerns the modes of the carboxyl group of hexanoic acid. In Fig. 4.19, the results are plotted for both temperatures. The broadening of the bands is well described in the 1400 cm^{-1} - 1500 cm^{-1} region, indicating that the band broadening observed experimentally in this region is reflective of the disorder occurring on the alkyl chain of the molecule due to temperature. However, although a broader C=O band is observable at 1608 cm^{-1}, the experimental band is of the order of 50 cm^{-1} broader. This could be due to the fact that the model only considers a periodic 1x1 cell, meaning that different orientations of the headgroup on the hematite slab are likely neglected. It is possible that considering a larger cell, the result would be more reflective of the experimental IRRAS spectra. Finally, the peak positions calculated are downshifted with respect to the experimental micro-IRRAS spectra of about 50 cm^{-1}. A possible explanation to this downshift is that the B3LYP functional further underestimates the bond strengths due to anharmonicity

introduced by the dynamics with respect to the spectra calculated in static conditions, which translates into downshifted vibrational frequencies.
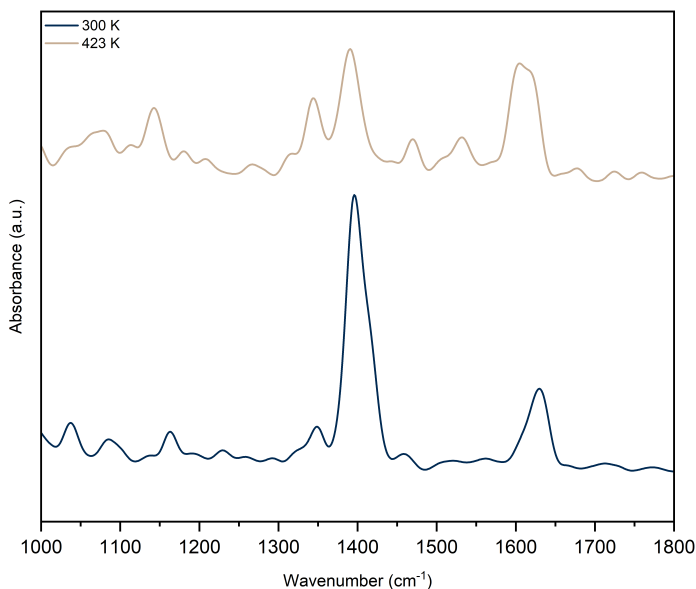
Figure 4.19: *Calculated IR spectra of hexanoic acid adsorbed on hematite after 5 ps DFT-MD run at 300 K (black), and 423 K (brown).*

4.4   Conclusions

In this chapter, we have demonstrated how the combination of micro-IRRAS spectroscopy and computational spectral calculation provide a reliable tool for the investigation of OFM adsorption on steel surfaces. In particular, we have confirmed that OFM do adsorb on the surface through their polar head, and we were able to assign the vibrational wavenumbers in the micro-IRRAS spectra to their vibrational modes. Moreover, we have shown the possible configurations in which the molecules can engage on the surface of steel, finding that the interaction nature is chemisorption through tight bonds between the functional groups of the OFM to the iron of the surface, which usually results in the deprotonation of the molecule. The lost hydrogen is then adsorbed on a surface iron. We also demonstrated how micro-IRRAS represent a powerful tool to investigate the effect of tribological contact thanks to its small measurement area. We have found, thanks to the interpretation provided by DFT calculations, that the effect of friction is to

tilt the molecules towards the surface. Although this tilt has been experimentally observed, it is still not yet clear why the molecules do not tilt back to the original angle upon removal of the load. However, this phenomenon can be reasonably connected to the friction reducing mechanism acted by OFMs, adding to the already present literature which correlated it to interdigitation phenomena among the molecules of the tribofilm and residual base oil molecules into the SAM. [112, 113] Using DFT-MD models, we also shown that the large bands found in the experimental micro-IRRAS spectra are caused by the molecular disorder that is introduced on the tribofilm due to temperature.

Effect of adsorption on the determination of the friction coefficient

5.1 Adsorption energies - the relevance of packing

As it was demonstrated in the previous chapter OFMs adsorb on the surface forming tight bonds with the surface of steel, arranging in SAMs. However, even though the combination of m-IRRAS spectroscopy combined with the calculation of adsorption spectra with DFT has provided a solid framework for understanding the adsorption configuration of the OFMs and can qualitatively assess the result of the tribological phenomena, little is yet known about what distinguishes the friction modifiers in terms of friction performances. However, we demonstrated indirectly that the interaction of the investigated friction modifiers on the surface pretty much occurs in the same way for all of them, i.e. through the interaction of the terminal CO groups (in the case of oleic amide the CN group is also involved). In this case, it is safe to assume that the strength of the interaction on the surface is roughly the same in all cases. Still, these OFM show different friction performances. Looking at GMO and PC21, for example, the only difference (in their molecular structures) lies in the substitution of one of the oxygen

on the head with an -NH group. However, the substituted -NH group does not participate in the interaction on the surface but it likely contributes to strengthening the interaction between the molecules of the tribofilm forming a hydrogen bond with the C=O of an adjacent molecule, as suggested by the DFT models and corroborated by the IRRAS spectra. Noticing this aspect (that hereby will be called "packing") brought to question the whole rationale behind OFM development, asking whether there was a larger contribution to the friction performance of OFMs can be caused by the packing interaction that holds the tribolayer together.

To answer this open question, through the methodology described in section 2.4.1, calculations of adsorption energy were performed. Subsequently, this quantity was split into the contributions of the interaction of the OFM head on the surface (interaction energy) and of the packing interaction among adjacent molecules in the tribolayer (Packing energy). In Fig. 5.1 the adsorption energy for each friction modifier investigated and its contributions are plotted and sorted on the x-axis in descending order with respect to the adsorption energy (from less stable to more stable). The plot shows unequivocally that - neglecting the interaction energy of OAm which is considerably less stable due to the deprotonation of the NH_2 group which is less favorable than the deprotonation of an OH group - the interaction contributes to the total adsorption energy are pretty much the same for all OFMs. Observing the packing contribution, instead, there is a remarkable difference. The trend of the packing energy seems to suggest that this contribution is what actually determines the difference in adsorption stability for all friction modifiers, since the total adsorption energy corresponds to the sum of packing and interaction energy (chapter 2, eqn. 2.10). The values of all calculated adsorption, packing, and interaction energies are listed in Tab. 5.1.

Table 5.1: *List of the DFT calculated adsorption, packing, and interaction energies for each of the OFM investigated (units in kcal/mol)*

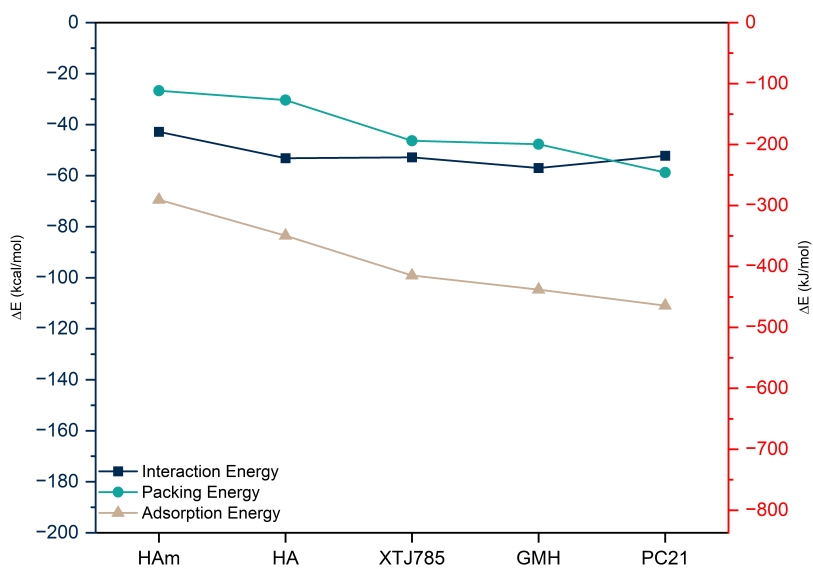| OFM	Adsorption Energy	Packing Energy	Interaction Energy
Hexanoic amide (monodentate)	-81.11	-26.68	-54.43
Hexanoic amide (bridging)	-69.46	-26.68	-42.78
Hexanoic acid (monodentate)	-82.57	-30.34	-52.24
Hexanoic acid (bridging)	-83.51	-30.34	-53.17
XTJ785 (C_6)	-99.12	-46.31	-52.81
Glycerol mono hexanoate	-104.69	-47.68	-57.00
PC21 (C_6)	-110.94	-58.74	-52.20

Figure 5.1: *Calculated adsorption energies and their interaction and packing contribute to each of the investigated OFMs.*

5.2 Correlation with Friction Coefficients

After finding that the packing energy is the discriminating factor that could determine the friction performances of OFMs, we checked if the experimental friction coefficient of the various investigated friction modifiers is in some way correlated to it. A large batch of MTM samples in ideally identical conditions (same sample material, lubricant formula containing only base oil and friction modifier in same quantities - 99% wt. squalane, 1% wt. OFM) was produced and tribological measurements were performed at three temperatures: 45, 120, and 150 °C, which are the common working temperature of these lubricant oils. All the results were recorded and after a simple post-process of the Stribeck curves (Fig. 5.2). A simple logistic fit is applied to each Stribeck curve, and the total friction coefficient is calculated as the area under the fitted curve. Afterwards, a simple linear regression analysis was done as a first analysis to assess whether a correlation between the adsorption energy and friction coefficient exists. The result of this linear regression is shown in Fig. 5.3, revealing a picture of not straightforward interpretation. As shown in the plot, at 45 and 120 °C, the friction performances of the OFM investigated seem to be all at the same level. However, at 150 °C this situation is completely different, showing an uncanny linear correlation with the adsorption energy (Correlation coefficient = -0.72; Pearson's r = 0.0001), which in turn is determined by the packing energy of the tribofilm, as demonstrated in the previous section. The variance in the data points was investigated previously in the Eni laboratories and was ascribed to the fact that when the lubricant mixture is made by squalane (base oil) and the friction modifier only, and the viscosity of the base oil plays an important role in the friction performances at low sliding speed, increasing the variance of the tribological results (is also to avoid this phenomenon that viscosity modifiers are added in the lubricant mix). An interesting aspect is the fact that the friction coefficient also seems to be linearly dependent with temperature, except in the cases of oleic amide and oleic acid. For these two OFMs, the friction coefficient decreases linearly with temperature up to 120 °C, whereas jumping from 120 to 150 °C friction coefficient increases for oleic amide and seems to stabilize for oleic acid. This aspect leads to suppose that the effect of the packing interaction is to allow the friction modifiers to extend the temperature at which they can retain their friction-reducing properties. However, the evolution with temperature of the tribofilm is still unclear at this point.

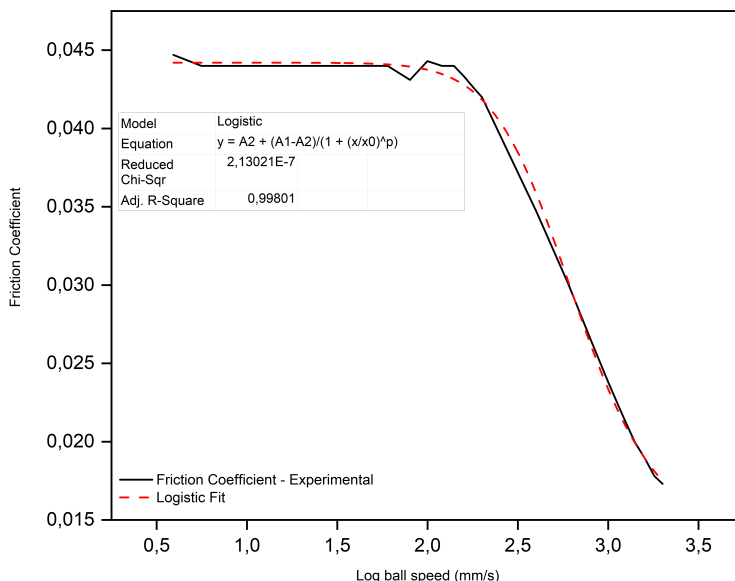**Figure 5.2:** *Example of a Stribeck curve recorded from the MTM tribological measurement (black) and logistic fit (red, dashed line). R^2 of the fit: 0,998. The total Stribeck friction coefficient is calculated as the area under the curve.*
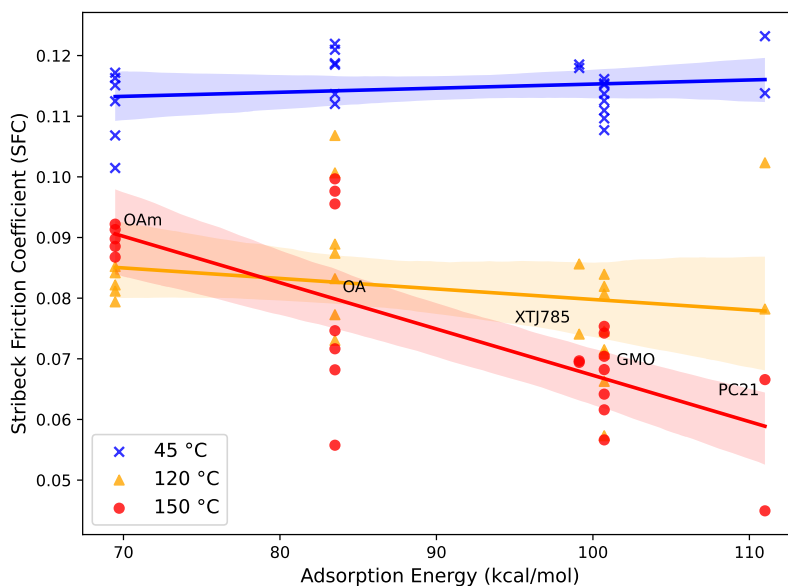
Figure 5.3: *Measured friction coefficient for each of the MTM samples investigated plotted with respect to the adsorption energy calculated from the DFT models.*

83

5.3 Gibbs' Free-energies of Packing

The adsorption energies from the DFT models are calculated assuming a completely static system at 0 K. Calculating the Gibbs' free energies of the packing contributions seemed to be the best way to go to possibly find an interpretation of the temperature-dependent phenomenon that was just observed. Using the methodology described in section 2.6.2, the Gibbs free energies of packing were calculated. The results for each OFM investigated are plotted in Fig. 5.4. The results obtained are in remarkable agreement
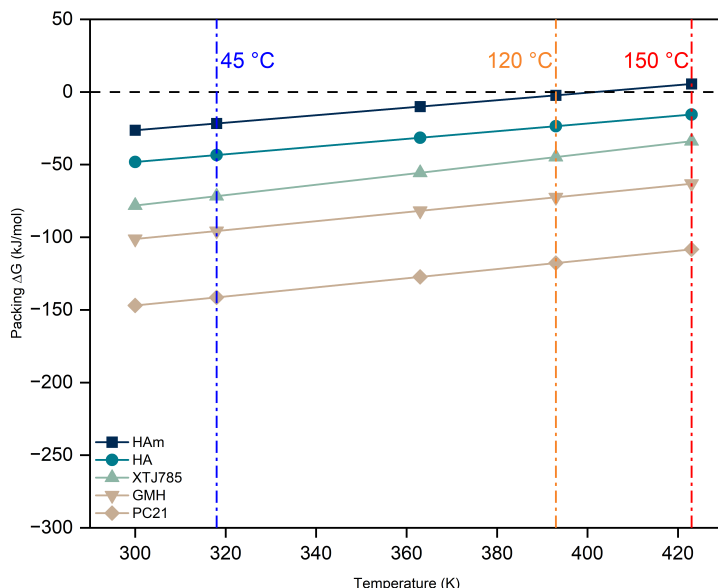
Figure 5.4: *Gibbs' free energies of packing calculated from the DFT models of the OFMs investigated.*

with the experimental tribological results. As shown in the plot, the Gibbs free energy of packing of oleic amide reaches 0 at temperatures around 120 °C (393 K), which is exactly where the friction performances of oleic amide are lost. For oleic acid, this temperature is close to 150 °C (423 K), possibly explaining why at that range of temperatures, its friction performances seem to stabilize, and the friction coefficient will likely rise with increasing temperature. The Gibbs free energy of packing for the other friction modifiers reaches zero at higher temperatures and retains the same order of the adsorption energies, thus very likely confirming the interpretation attempt discussed before. This also corroborates the idea that the true actor in the determination of the friction performances of OFMs, provided a tight in-

teraction with the surface of the steel, is the interaction among the friction modifier molecules inside the tribofilm. The friction coefficient will decrease with temperature until the packing is stable, and will start increasing again once the packing is not stable anymore.

5.4 Conclusions

In this chapter, we have confirmed through adsorption energy calculations the chemisorptive nature of the adsorption of OFMs on steel surfaces. Moreover, we have demonstrated how the adsorption energy can be divided into two terms that represent the interaction of the molecules on the surface, and the interaction of the molecules of the SAMs with the ones adjacent to them, which we called interaction energy and packing energy respectively. This separation allowed us to understand how the packing energy contribution is the one that governs the differences among the OFMs studied, both in terms of the stability of the tribofilm, and its friction performances. Regarding the latter, we have found that there is a clear correlation between the strength of the packing and the friction coefficient recorded during tribological measurements. We have also investigated the effect of temperature through calculations of Gibbs' free adsorption energies, and shown that the range of temperature in which the packing free energy is negative is in relative good agreement with the experimental window in which the friction modifiers show the best friction reducing performances.

CHAPTER 6

Classical dynamics to understand the effect of adsorption on friction performances of OFM

6.1   Hexanoic acid adsorbed on hematite - no sliding

In the previous chapter, the crucial role of the interactions between the OFM molecules in the SAM in determining friction performances has been introduced and investigated through DFT energy calculations. However, there are still physical insights about friction phenomena at the microscopic level that are worth investigating. To do this, MD simulations are the best approach as they allow to observe the dynamical evolution of the system in presence of external forces at a much wider scale compared to DFT simulations. As it was demonstrated, friction performances seem to be determined by the temperature at which the packing among the molecules in SAM fails, which happens when the tightly packed state is not favorable anymore. The behavior of OFMs has been investigated extensively with MD simulations, as described in chapter 2. However, to the best of our knowledge, the role of packing has never been investigated before. A first set of MD simulations was run to confirm if the calculations can correctly predict the temperature

at which the failure of the packed state occurs without the presence of external inputs, which in our case translates into the absence of tribological stresses. In order to reduce the computational costs, the MD simulation was carried out only on adsorbed tribofilms of hexanoic acid. Given the similarities among all the friction modifiers investigated, it is expected that the information acquired from the simulations could be extended to describe the other friction modifiers. MD simulations were carried out at three increasing temperatures: 300K, where we expect the tribofilm to be stable; 420K, close to the predicted temperature at which packing would fail from DFT calculations; 500K, which is well beyond the predicted packing failure temperature. If the calculation can predict this temperature correctly, substantial differences should be observed at 500K that could be connected to this packing phenomenon. In Fig. 6.1, a snapshot of the hexanoic acid slab after the full MD run at 300K is shown. The molecules appear collectively ordered on the surface of hematite, which is a hint that the packed layer is very stable. The headgroups of hexanoic acid also appear very ordered on the surface, as each carboxyl group is oriented in the same direction (imagining a vector crossing the two terminal oxygens). This situation is kept at 420 K (Fig 6.2), although the chains show an increased orientational disorder. At 500 K, disordered domains are formed on the surface of hematite by the headgroups of hexanoic acid, as one can realize by observing Fig. 6.3. The carboxyl groups jump from one functionalization site (iron) to another one, as an effect of the increased level of freedom of the chains due to the instability of the packing interaction at this temperature.

Figure 6.1: *Snapshot (bottom view) of the 10x10 slab of hexanoic acid adsorbed on hematite after 2 ns classical MD run at 300K. The hematite slab has been hidden from view for clarity purposes.*

Figure 6.2: *Snapshot (bottom view) of the 10x10 slab of hexanoic acid adsorbed on hematite after 2 ns classical MD run at 420K. The hematite slab has been hidden from view for clarity purposes.*
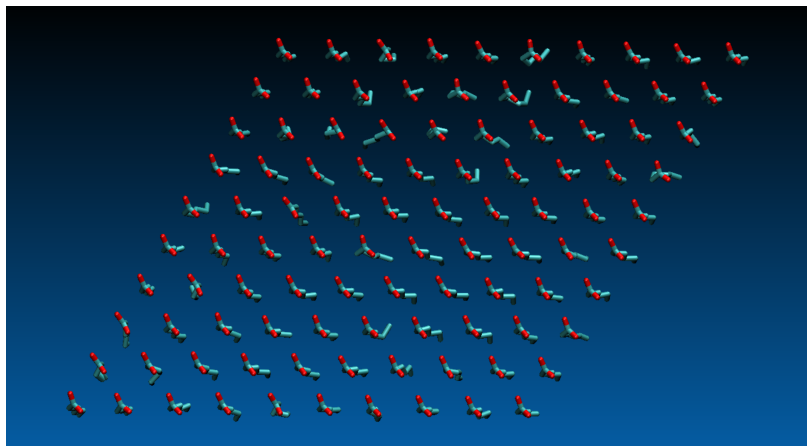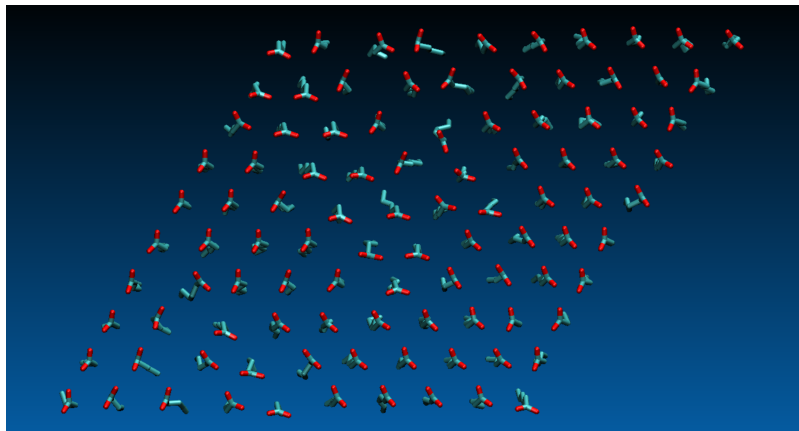
Figure 6.3: *Snapshot (bottom view) of the 10x10 slab of hexanoic acid adsorbed on hematite after 2 ns classical MD run at 500K. The hematite slab has been hidden from view for clarity purposes.*
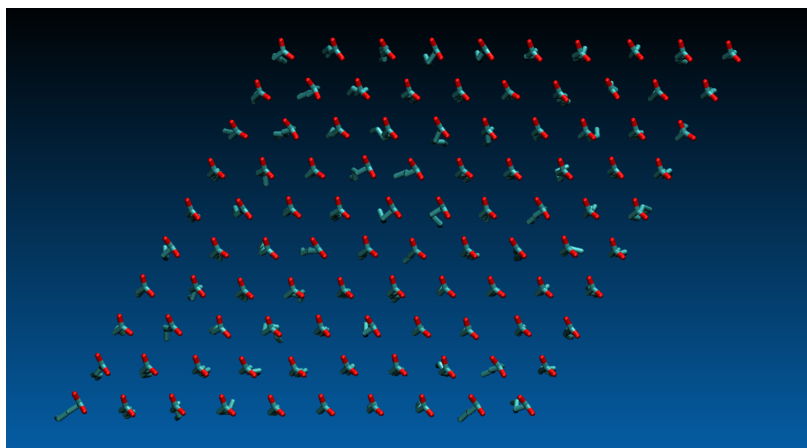
To better describe the level of the order of the molecules in the SAM, we choose three quantities as order parameters: Firstly, the distribution along all the trajectory of the scalar products of the vector $\mathbf{v}_i$ crossing the two terminal oxygens of one molecule's headgroup with the vectors $\mathbf{v}_j$ crossing the terminal oxygens of the first adjacent molecules of the SAM (Fig. 6.4a).

$$O = \mathbf{v}_i \cdot \mathbf{v}_j \tag{6.1}$$

The parameter O describes the orientation of each molecule head group with respect to the other molecules in the SAM, and it allows to understand whether disordered domains occur on the slab. Secondly, the distribution of the dihedral angle $\theta = \widehat{O_1 C_1 C_2 C_3}$ between one terminal oxygen atom of the molecule and the third carbon of the alkyl chain (Fig. 6.4b). This parameter is chosen as a description of the orientation of the molecules in the SAM. Finally, the distribution of the end-to-end distances $d = \|C_1 C_6\|$ of the alkyl chain of the molecules (Fig. 6.5). This parameter describes the amount of torsional deformation that occurs on the molecules. In Fig. 6.6, the order parameter O is plotted for each temperature. At 300 K, the distribution of the order parameter peaks at 0, indicating that the vectors crossing the oxygens in the carboxyl groups are all mostly parallel to each other. A similar situation is depicted at 420 K. However, the distribution is slightly broadened by the effect of temperature. At 500 K, the distribution shows a new, very broad peak, indicating the formation of the unordered domains that were observed on the snapshots at the end of the trajectory. The distri-

a)   b)
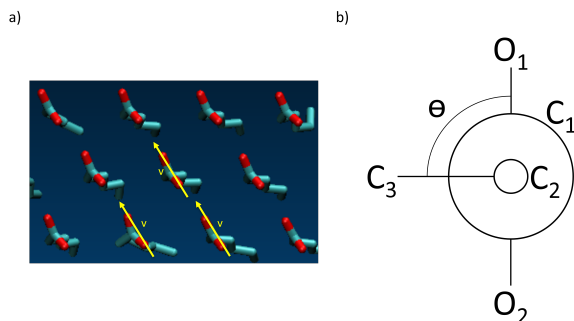
Figure 6.4: *Schematics showing the descriptors emplyed for the calculation of the order parameters: a) vectors crossing the oxygens of the carboxylic head groups of hexanoic acid; b) The dihedral angle $O_1\widehat{C_1C_2}C_3$ between one terminal oxygen atom of the molecule and the third carbon of the alkyl chain.*
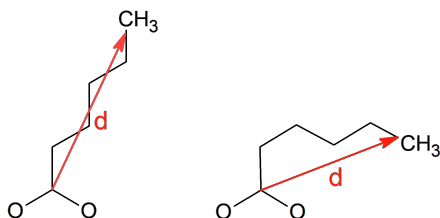
Figure 6.5: *End-to-end distance of the alkyl chain of hexanoic acid.*

bution of the dihedral angle θ (Fig. 6.7) at 300 K shows a narrow peak at 110° showing a high degree of order, as all the molecules are oriented in one direction. Rising the temperature to 420° the narrow peak is replaced by a smaller, broader peak at 100°, and by a smaller, very broad peak at -100°, showing that at higher temperatures the chains are more disordered, starting to face opposite directions. Analyzing the distribution at 500 K to infer molecular orientation would be meaningless, as the definition of the angle depends on the orientation of the carboxyl group. However, this parameter still carries information about the disorder on the tribofilm. At 500 K the distribution of the dihedral angle θ is distributed almost equally around 100° and -100°, showing a state where the two orientations along the O-O axis of the carboxyl group have an almost equal probability of occurring after 2 ns MD evolution. This is also likely to reflect the loss of packing interactions in the tribofilm, allowing the molecules to rotate the dihedral angle freely. Lastly, the end-to-end distance d of the alkyl chain of hexanoic acid shows a similar trend: at 300 K the distribution clearly centered
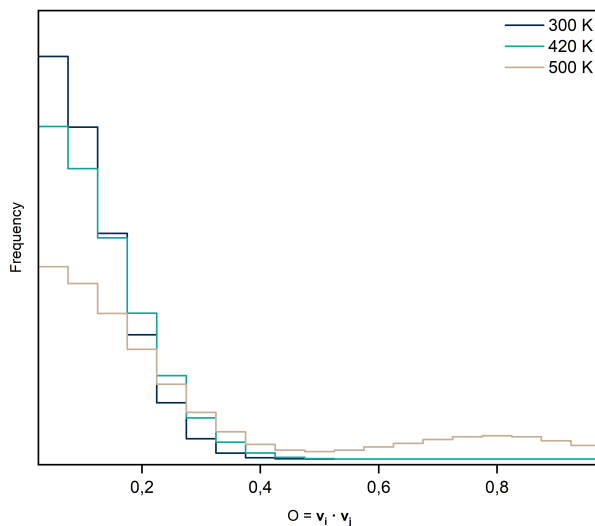
Figure 6.6: *Distribution of the scalar product of vectors crossing the atomic center of the oxygens of the carboxyl groups of hexanoic acid after 2 ns MD evolution at 300 K (black), 420 K (blue), and 500 K (light brown).*

at 6.00 Å. With increasing temperature, the distribution broadens, and its maximum decrease reaching 420 K. At 500 K the distribution undergoes a greater broadening, and its maximum shifts to around 5.50 Å, showing that going from 420 K to 500 K - crossing the packing failure temperature - results in a sudden increase of disorder on the molecules adsorbed on the slab.
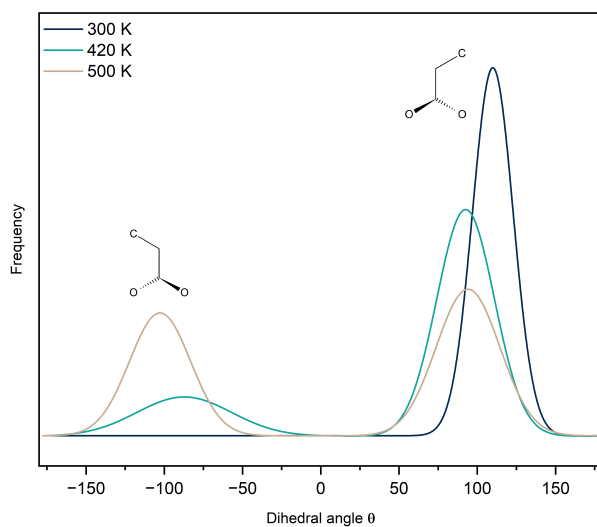
Figure 6.7: *Distribution of the dihedral angle θ of hexanoic acid after 2 ns MD evolution at 300 K (black), 420 K (blue), and 500 K (light brown).*
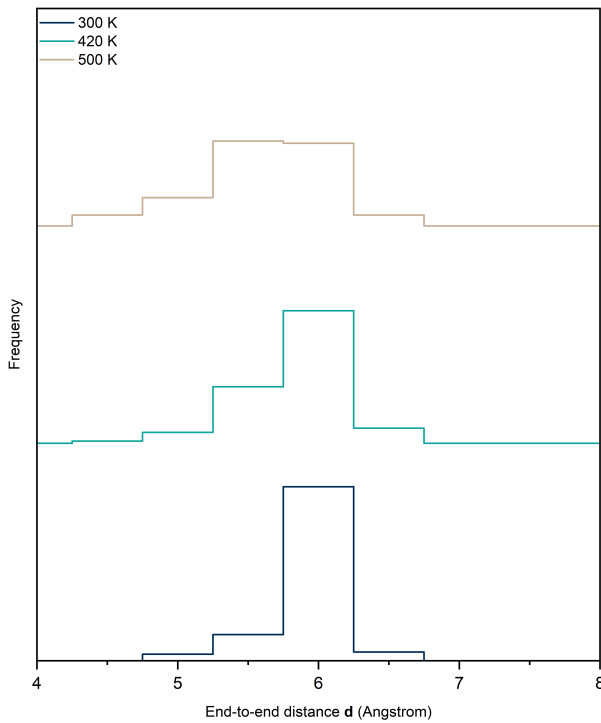
Figure 6.8: *Distribution of the end-to-end distance d of the alkyl chains of hexanoic acid after 2 ns MD evolution at 300 K (black), 420 K (blue), and 500 K (light brown).*

6.2 Hexanoic acid adsorbed on hematite - sliding

To paint a complete picture of the temperature behavior of the packing of hexanoic acid, it is then appropriate to investigate the tribofilm simulating a sliding tribological contact. The geometries of the slab at the last step of the previous run were used to generate a second slab that was positioned on top of the first one. In the space between the two slabs, molecules of squalane were added to simulate the base oil of the lubricant. The two slabs were then put under pressure, creating a sandwich-like structure. This structure was let evolve for an additional 0.5 ns and at this point, the sliding simulations were initiated. Six simulations at three temperatures were run - 300 K, 420 K, and 500 K. As earlier, the aim is to observe the behavior of the tribofilm when crossing the packing failure temperature, as well as the behavior of the tribofilm when the packing of the OFM molecules is still stable. The first set of simulations was run applying a relative sliding velocity of 1 m/s between the two slabs, inverting the direction of motion after 0.5 ns, and then letting the trajectory evolve for another 2 ns. In the second set, a successive inversion of motion was introduced after 1 ns from the first one. To describe the behavior of the tribofilm, the same order parameters discussed before were chosen as descriptors. The evolution of the order parameter θ along the trajectory at 300K shows how the molecules of the slab collectively react with the direction of friction during tribological sliding (Fig. 6.9). Letting the direction of friction constant for 2 ns, it can be observed how the population of one orientation keeps increasing, while the population of the other one decreases accordingly. When the direction of motion is inverted again, the molecules of the SAM quickly adjust and the populations invert in ~0.5 ns. Increasing the temperature to 420K (Fig. 6.10), the behavior of the tribofilm is still to follow along the direction of friction. However, as it can be observed from the trajectory with two inversions of motion, the molecules seem to react quicker to the change of direction, as more torsional angles flip in the same timespan with respect to the situation at 300K. Rather interestingly, when the packing failure temperature is crossed, as the evolution of the torsional angle θ at 500K in Fig. 6.11 demonstrates, the molecules of the SAM seem to not be affected anymore by the sliding direction, which is suggested by observing the fact that at the end of the trajectory, the torsional angle θ is actually aligned in the opposite direction. Moreover, when adding a further inversion of motion, the populations do not flip, corroborating the idea that at 500 K, once the packing is not any more stable, the motion of the molecules in the SAM is not collective anymore. This supports the hypothesis that the pack-

ing of the molecules in the SAM contributes to friction reduction, which is acted by the collective motion of the torsional angles of the molecules that flip together according to the direction of motion to find a more energetically favorable arrangement. As long as the temperature is below the packing failure, the molecule can arrange quicker increasing temperature, resulting in less friction.   The end-to-end distances of the alkyl chains of

Figure 6.9: *Evolution in time of the dihedral angle θ of hexanoic acid at 300 K. 2.5 ns MD run at 1 m/s relative sliding velocity. The full lines represent a run with an inversion of motion placed after 0.5 ns evolution, the dash-dot lines represent a run with a second inversion of motion at 1.5 ns evolution.*

the molecules of the SAM (Fig. 6.12), in the same way as in the simulations with no tribological sliding, tend to decrease with temperature. At the same time, their distribution gets broader. In general, at 300 and 420 K, the distribution is broader than in the no-sliding simulation at the same temperature. Interestingly enough, at 500 K the distribution looks almost the same in both cases. This is further confirmation that at temperatures higher than the packing failure temperature, the molecules of the SAM seem to act independently from one another. In the MD simulation of the single slab, it was observed that the carboxyl groups of hexanoic acid maintained a well-ordered arrangement on the surface of hematite, albeit showing disordered domains when the temperature was set at 500 K. In Fig. 6.13, 6.14, and 6.15, the snapshots of the slab after the MD runs with the tribological contact show an analogous situation. The order of the carboxylic heads is maintained until reaching the temperature of 500K, at which disordered
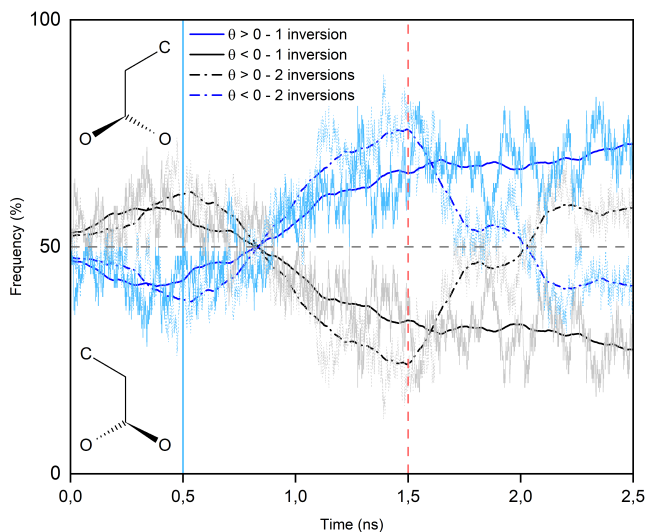
Figure 6.10: *Evolution in time of the dihedral angle θ of hexanoic acid at 420 K. 2.5 ns MD run at 1 m/s relative sliding velocity. The full lines represent a run with an inversion of motion placed after 0.5 ns evolution, the dash-dot lines represent a run with a second inversion of motion at 1.5 ns evolution.*

domains appear. As earlier, the order parameter $O = \mathbf{v}_i \cdot \mathbf{v}_j$ shows that the heads of hexanoic acid are very well ordered at 300 K as their distribution only shows one maximum at 0, indicating that all the carboxylic heads are parallel to each other. The distribution broadens at 420 K, while at 500 K a new peak of the distribution forms, indicating the presence of disorder (Fig. 6.16). Comparing these distributions with the one obtained in the absence of friction (Fig. 6.17), it is surprising to observe that at 300 K and 420 K, almost no difference is seen between the two cases. The difference arises after the packing fails, at 500 K, where the distribution in the presence of friction shows a higher amount of disorder. Here as well, the impact of packing on the collective behavior of the molecules in the SAM is clearly noticeable.
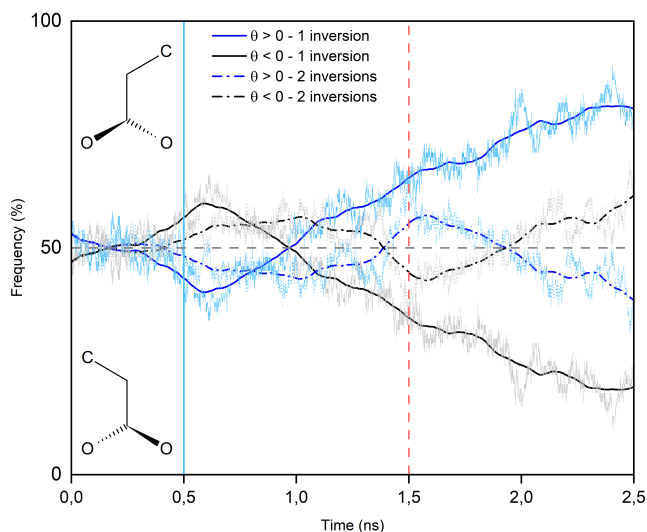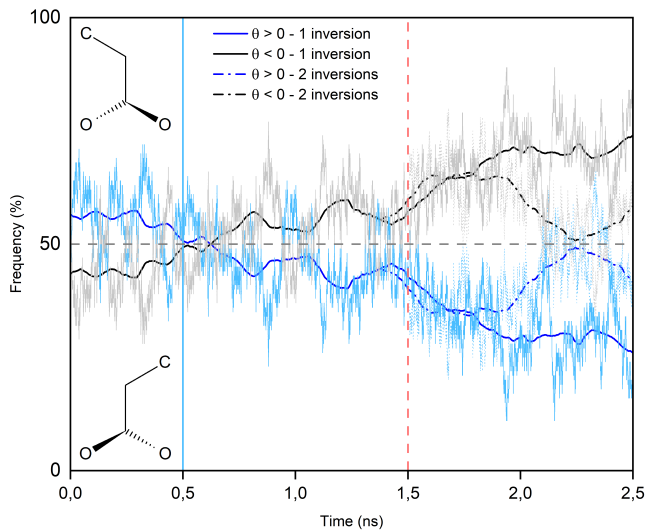
Figure 6.11: *Evolution in time of the dihedral angle θ of hexanoic acid at 500 K. 2.5 ns MD run at 1 m/s relative sliding velocity. The full lines represent a run with an inversion of motion placed after 0.5 ns evolution, the dash-dot lines represent a run with a second inversion of motion at 1.5 ns evolution.*
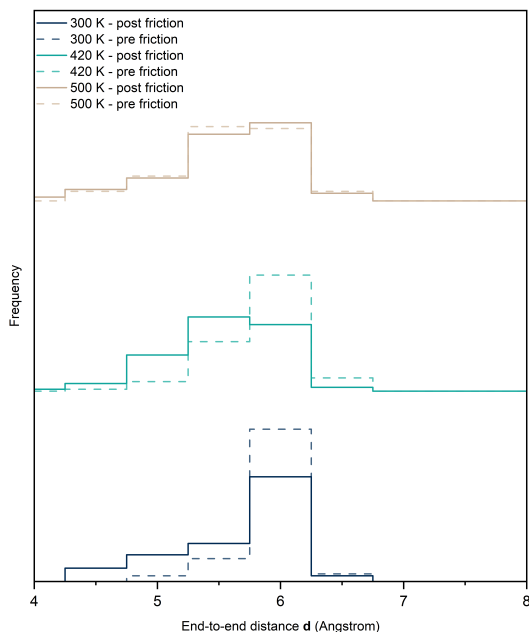
Figure 6.12: *Distribution of the end-to-end distance d of the alkyl chains of hexanoic acid after 2.5 ns MD evolution at 300 K (black), 420 K (blue), and 500 K (light brown) (full lines). The dashed lines represent the same distribution after 2 ns evolution with no relative sliding velocity applied.*

Figure 6.13: *Snapshot (bottom view) of the 10x10 slab of hexanoic acid adsorbed on hematite after 2.5 ns classical MD run at 300K (1 m/s relative sliding velocity). The hematite slab has been hidden from view for clarity purposes.*
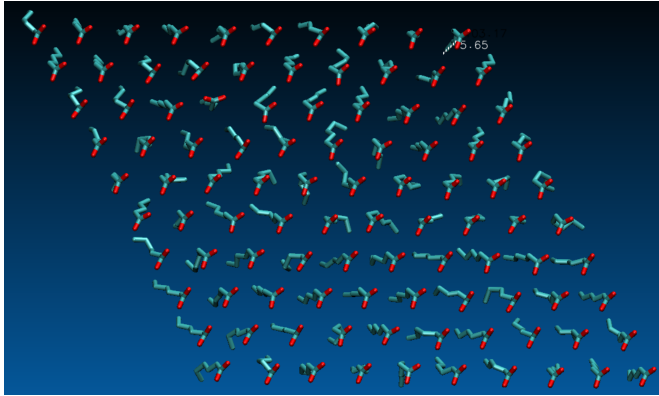
Figure 6.14: *Snapshot (bottom view) of the 10x10 slab of hexanoic acid adsorbed on hematite after 2.5 ns classical MD run at 420K (1 m/s relative sliding velocity). The hematite slab has been hidden from view for clarity purposes.*

Figure 6.15: *Snapshot (bottom view) of the 10x10 slab of hexanoic acid adsorbed on hematite after 2.5 ns classical MD run at 500K (1 m/s relative sliding velocity). The hematite slab has been hidden from view for clarity purposes.*

Figure 6.16: *Distribution of the scalar product of vectors crossing the atomic center of the oxygens of the carboxyl groups of hexanoic acid after 2.5 ns MD evolution at 300 K (black), 420 K (blue), and 500 K (light brown) - 1 m/s relative sliding velocity.*

Figure 6.17: *Distribution of the scalar product of vectors crossing the atomic center of the oxygens of the carboxyl groups of hexanoic acid after 2.5 ns MD evolution at 300 K (black), 420 K (blue), and 500 K (light brown) - 1 m/s relative sliding velocity (full lines). The dashed lines represent the same distribution after 2 ns evolution with no relative sliding velocity applied.*

6.3 Conclusions

In this chapter, we demonstrated through molecular dynamics simulations that the effect of packing interactions among the friction modifier molecules is translated into collective torsional motions that occur when the tribofilms are sliding against each other. These collective motions are facilitated by the temperature increase, justifying the well-behaved temperature-dependant friction coefficient. This is true until, at high temperatures, the packing can no longer be maintained, i.e. the entropy driving force prevails. At that point, we observe the formation of disordered domains of the SAM on the surface. When this happens, the molecules of the SAM are not moving collectively anymore, causing the loss of performance. These results confirm the picture painted in the previous chapter when discussing electronic and Gibbs' adsorption energies provides a phenomenological explanation to the results obtained.

Conclusion

The development of higher-performance lubricants requires a deep understanding of additive adsorption on steel surfaces and their competitive interactions, and their behavior during the tribological processes. In other words, to open the way to the rational design of these lubricants the precondition is to know the characteristics that can be tailored at the molecular structure level that translate into lower friction coefficients. In this thesis, I have demonstrated that micro-IRRAS, DFT, DFT-MDs, and classical MDs computational methods are very powerful tools to access this precious information.

We provided clear pictures of how organic friction modifiers adsorb on steel surfaces, which molecular sites interact with the surface, and the strength of the interaction. Adding to the originality of our approach, here we applied a derivation of the IRRAS technique that allowed us to greatly restrict the investigation area compared to traditional IRRAS methods, and determine the adsorption state of the organic friction modifiers. We determined that the organic friction modifiers molecules definitely tilt towards the surface of steel during friction, and we also provided a methodology to determine its entity. However, this approach can be further improved. The micro-IRRAS technique used in our work, albeit possessing the ben-

efit of yielding separate information on the species interacting only with the metallic surface and those that were also mechanically stressed by the tribotest, is still subjected to the drawbacks of an IRRAS method without polarization modulation (PM-IRRAS). This unfortunately results in great noise in the recorded signals. Even though this detrimental effect is greatly reduced with respect to traditional IRRAS, thanks to a shorter path length in air, micro-IRRAS would dramatically benefit from the capability of reducing the noise of a polarization module. To summarize our results:

- The combination of experimental and computational approaches, through the simulation of the experimental technique allows us to determine the adsorption state of organic friction modifiers;

- Organic friction modifiers do adsorb through their polar head, resulting in tightly packed, chemisorbed SAMs;

- More than one adsorption configuration can be present on the surface of hematite (i.e., oleic acid forming monodentate and bridging configurations);

- micro-IRRAS is a valid tool to assess the result of competition processes among additives in complex lubricant formulations;

- Organic friction modifiers molecules do tilt towards the surface as a result of the tribological stress.

The computational approach also allowed us to evaluate the strength of the adsorption of organic friction modifiers. We found that most of the difference in adsorption strength among organic friction modifiers results from interactions among the adjacent molecules in the SAM, rather than their interaction with the surface, which was almost equal for all the organic friction modifiers investigated. This finding led us to question whether this could be a reasonable determining factor for their different tribological performances. We found that this is indeed the case. The interaction of the organic friction modifiers with the surface is still an important factor in the determination of tribological performances, but the packing interactions among the friction modifier molecules determine how steeply the friction coefficient drops with temperature, and also determine the critical temperature at which the friction modifier loses its friction reducing properties. Molecular dynamics simulations were crucial in understanding this phenomenon, as we could extrapolate that the effect of packing interactions among the friction modifier molecules is reflected in collective torsional motion that occurs when the tribofilms are sliding against each other.

Adding to the originality of our approach, we were able to perform the simulations from the adsorption configurations obtained from the density functional theory models. These collective motions are facilitated by the temperature increase, justifying the temperature-dependant friction coefficient, until the packing can be no longer maintained, and friction performances are lost as a result of the formation of disordered domains of the SAM on the surface. When this happens, the molecules of the SAM are not moving collectively anymore, contributing to the loss of performance. The remarkable results obtained through the combination of computational (density functional theory and molecular dynamics) and experimental techniques (tribological stribeck friction coefficient measurements, in this case), further reiterate the power of this approach. Nevertheless, there is room for improvement. Here we have simplified our approach modelling a shorter version of the organic friction modifier molecules. Moreover, our simulation relied on ideal hematite surfaces which were absent of defects and modifications imparted from the environment. In the real case, the surface would present irregularities (roughness), and be subjected to the presence of humidity and oxygen that can modify the nature of the surface as the system evolves. To summarize:

- The friction performances of organic friction modifier are determined by the interaction among adjacent molecules in the SAM;

- The interaction between organic friction modifier and steel surface is of chemisorption;

- Friction performances are tightly correlated with the entity of the packing strength of the SAM;

- The effect of packing is to allow the same to collectively respond to the tribological stress;

- This collective motion is facilitated by temperature increase, which results in better performances at higher temperatures;

- The packing strength determines a limit temperature at which the collective behavior of the SAM cannot be maintained anymore, resulting in loss of friction performance.

With these results as a guideline, an immediate suggestion for the development of future OFMs is to design the head and tail of the molecules to maximize the number of cohesive interaction among the molecules assembled in a SAM, at the same time maintaining a relatively low size of

the molecules, to guarantee a dense covering of the surface. As far as the computational models are concerned, this approach would greatly benefit from the use of reactive force fields, to take proper account of the interaction between the head of the molecule and the surface irons. Furthermore, hydroxylation of the surface should be taken into consideration to provide a representation of the surfaces which is closer to the real case.

To conclude, it is crucial to discuss the implications of the findings obtained from this approach on the future development of Organic Friction Modifiers. As a matter of principle, the results obtained computationally, are only dependent on the knowledge of the structure of the organic friction modifier. This means that future development of organic friction modifiers can benefit from software-assisted molecular design tools that can be implemented to tailor to this specific task. Moreover, the presence of the tight correlation among adsorption energy, temperature, and friction performances suits very well to machine learning extensions that would allow us to predict friction performance starting only from the knowledge of the molecular structure of the friction modifier. Of course, experimental validation will be always necessary. However, these applications could save a dramatic amount of time and expenses that are currently injected into the organic friction modifiers research and development.

APPENDIX $\mathcal{A}$

Computational Details

A.1   CRYSTAL17 input files

A.1.1   Input Data file - adsorbed hexanoic acid on hematite

Note: here only the input file for the hexanoic acid molecule will be shown. All the other inputs are obtained simply inserting the starting coordinates of each model and changing the number of atoms and cell parameters accordingly. The $C_{1}8$ geometries are obtaining by adding the necessary amount of carbon atoms on the chain from the optimized C_6 structures.

```
# comment line
SLAB
1
5.035 5.035 120
45
26    0.68136    0.34068    2.51475
26    0.34059    0.68073    7.04260
26    0.68099    0.34002    6.41101
26    0.33773    0.67361   11.05934
26    0.01950    0.00456   11.44164
26    0.34061    0.68125    4.23589
26    1.02190    1.02186    4.66541
26    1.01972    1.02040    8.65618
26    0.68232    0.34233    9.27404
```

```
26    0.69112    0.36548   12.98050
 8    0.71144    1.02198    3.39119
 8    0.31850    1.01719   10.09757
 8    0.00006    0.71150    3.39119
 8    0.00195    0.31448   10.11352
 8    0.31054    0.31060    3.39119
 8    0.70797    0.71169   10.09520
 8    0.36937    0.33956    7.85053
 8    0.68242    0.03040    7.83964
 8    0.99202    0.65138    7.84628
 8    0.02395    0.69264   12.34060
 8    0.65492    0.68445    5.60010
 8    0.34758    0.36103   12.31103
 8    0.33690    0.99205    5.59951
 8    0.67391    1.00718   12.38006
 8    0.02971    0.36683    5.59898
 8    0.63027    0.14319   16.07982
 8    0.82032    0.64857   16.11099
 6    0.70484    0.37478   16.73529
 6    0.66665    0.34992   18.23155
 6    0.77063    0.66087   18.90228
 6    0.73012    0.62601   20.42370
 6    0.83358    0.93659   21.09311
 6    0.79545    0.90312   22.60824
 1    0.48442    0.46688   20.66161
 1    0.86867    0.52744   20.82185
 1    1.07905    1.09699   20.85929
 1    0.69469    1.03559   20.70541
 1    0.55105    0.74741   22.87258
 1    0.87181    1.13108   23.06546
 1    0.93644    0.80949   23.02462
 1    0.84596    0.66631   15.15006
 1    1.01668    0.81950   18.66823
 1    0.63247    0.75986   18.50346
 1    0.80363    0.25027   18.63482
 1    0.42062    0.19175   18.46377
OPTGEOM
NOGUESS
FULLOPTG
END
BASISSET
POB-DZVP
UHF
DFT
SPIN
B3LYP-D3
XLGRID
ENDdft
SHRINK
4 4
TOLDEE
8
SPINLOCK
0 15
SCFDIR
```

```
LEVSHIFT
3 0
FMIXING
30
TOLINTEG
8 8 8 8 16
MAXCYCLE
100000
EXCHSIZE
10000000
BIPOSIZE
10000000
ATOMSPIN
10
 1 -1
 2 -1
 3 -1
 4 -1
 5 -1
 6  1
 7  1
 8  1
 9  1
10 1
ENDscf
```

A.1.2   Input Data file - starting coordinates of all adsorption models

Hexanoic amide

```
5.035 5.035 120
46
26    0.68136    0.34068    2.51475
26    0.34070    0.68008    7.04358
26    0.68134    0.33990    6.40852
26    0.33934    0.67908   11.07767
26    1.01756    1.01378   11.45065
26    0.34075    0.68126    4.23560
26    0.00002    1.02171    4.66561
26    0.00042    1.02122    8.66467
26    0.68176    0.33836    9.26377
26    0.68055    0.33403   12.77667
 8    0.71144    1.02198    3.39119
 8    0.31576    1.01821   10.11365
 8    0.00006    0.71150    3.39119
 8    0.00265    0.31339   10.10381
 8    0.31054    0.31060    3.39119
 8    0.70233    0.70305   10.10696
 8    0.36978    0.33806    7.84351
 8    0.68246    0.02843    7.84496
 8    0.99243    0.65113    7.84838
 8    0.01778    0.68062   12.32212
 8    0.65515    0.68413    5.59924
 8    0.32708    0.34758   12.38097
 8    0.33726    0.99162    5.59916
```

```
8    0.66850    0.99604    12.35929
8    0.02982    0.36652     5.59942
8    0.72438    0.37209    14.85148
6    0.96930    0.42263    15.44750
6    0.98720    0.45606    16.96484
6    0.72536    0.47990    17.60861
6    0.75558    0.50866    19.13237
6    0.49296    0.52699    19.81005
6    0.52491    0.55497    21.33112
1    0.99461    0.25591    17.38087
1    0.18790    0.65900    17.22355
1    0.71937    0.68047    17.18976
1    0.50453    0.27581    17.33602
1    0.76752    0.31035    19.54398
1    0.97640    0.71454    19.40021
1    0.48069    0.72478    19.39967
1    0.27295    0.32103    19.54371
1    0.53010    0.35615    21.76625
1    0.33269    0.56727    21.79431
1    0.73946    0.76307    21.62378
1    0.20875    0.41699    13.78778
1    0.37394    0.47259    15.36818
7    0.18863    0.44420    14.83556
```

Glycerol mono hexanoate

```
5.035    5.035    120
56
26    0.94548    0.85818     2.51475
26    0.60598    0.17765     7.04083
26    0.94655    0.85879     6.41049
26    0.61546    0.18388    11.03680
26    0.26016    0.53432    11.45387
26    0.60500    0.17694     4.23543
26    0.26453    0.51764     4.66575
26    0.26682    0.51714     8.65952
26    0.94463    0.85746     9.27075
26    0.91678    0.84463    12.95595
 8    0.97556    0.51745     3.39119
 8    0.57548    0.51401    10.09433
 8    0.26418    0.20696     3.39119
 8    0.26856    0.84187    10.09485
 8    0.57466    0.82810     3.39119
 8    0.97696    0.20645    10.12103
 8    0.63577    0.85894     7.84870
 8    0.94717    0.54711     7.85111
 8    0.23440    0.14802     7.83670
 8    0.28806    0.19061    12.45133
 8    0.91946    0.18039     5.59768
 8    0.59453    0.87816    12.28556
 8    0.60205    0.48813     5.60029
 8    0.92677    0.50393    12.31921
 8    0.29432    0.88435     5.59950
 8    0.73214    0.03700    19.58128
 8    0.32099    0.97200    18.31927
```

```
8    0.88580    0.89823   14.78288
8    0.53108    0.16964   14.82199
6    0.45758    0.96979   19.49271
6    0.22713    0.83856   20.61272
6    0.51474    0.03775   17.14500
6    0.34576    0.09255   16.00939
6    0.02743    0.83653   15.77049
6    0.36095    0.99344   21.95616
6    0.14169    0.83110   23.11887
6    0.26435    0.99323   24.45924
6    0.05106    0.82276   25.62991
1    0.15315    0.59093   20.66161
1    0.02271    0.85330   20.34392
1    0.73722    0.24378   17.35530
1    0.55644    0.87045   16.88510
1    0.31978    0.29371   16.23607
1    0.05386    0.63832   15.47198
1   -0.10115    0.77652   16.72525
1    0.64318    0.05274   14.79501
1    0.40421    0.22534   13.32071
1    0.58087    0.99985   22.13067
1    0.41585    0.21352   21.90938
1    0.93894    0.81278   22.91159
1    0.09628    0.59207   23.18750
1    0.49331   -0.00202   24.64355
1    0.30104    0.20675   24.39481
1    0.84419    0.79683   25.47721
1    0.14225    0.94444   26.58333
1    0.01930    0.59040   25.73554
```

XTJ785 - C$_6$

```
5.035 5.035 120
81
26  -0.31864    0.34068    2.51475
26   0.34059   -0.31927    7.04260
26  -0.31901    0.34002    6.41101
26   0.33773   -0.32639   11.05934
26   0.01950    0.00456   11.44164
26   0.34061   -0.31875    4.23589
26   0.02190    0.02186    4.66541
26   0.01972    0.02040    8.65618
26  -0.31768    0.34233    9.27404
26  -0.30888    0.36548   12.98050
 8  -0.28856    0.02198    3.39119
 8   0.31850    0.01719   10.09757
 8   0.00006   -0.28850    3.39119
 8   0.00195    0.31448   10.11352
 8   0.31054    0.31060    3.39119
 8  -0.29203   -0.28831   10.09520
 8   0.36937    0.33956    7.85053
 8  -0.31758    0.03040    7.83964
 8  -0.00798   -0.34862    7.84628
 8   0.02395   -0.30736   12.34060
 8  -0.34508   -0.31555    5.60010
```

113

```
8   0.34758   0.36103  12.31103
8   0.33690  -0.00795   5.59951
8  -0.32609   0.00718  12.38006
8   0.02971   0.36683   5.59898
1  -0.52950   0.43196  21.58844
1  -0.50215   0.33509  15.13544
1  -0.45405   0.28170  19.51194
1  -0.38547   0.00324  20.28634
1  -0.37786  -0.02297  17.83054
1  -0.36883   0.09241  22.69994
1  -0.33536   0.01083  15.69554
1  -0.36426   0.25344  27.08814
6  -0.28053   0.21329  19.67684
8  -0.31432   0.38309  14.66374
1  -0.32527   0.19327  29.62364
6  -0.29936   0.62368  21.80204
1  -0.28932   0.13520  32.17024
6  -0.17226   0.15430  18.34294
1  -0.30207   0.70085  22.82004
6  -0.16269   0.22625  15.23984
6  -0.12241   0.25766  22.64714
8  -0.15942   0.49986  24.65724
1  -0.24855   0.80908  21.09354
6  -0.11640   0.41492  27.07044
1  -0.18770   0.53784  17.42134
6  -0.07822   0.35947  29.58894
1  -0.05387  -0.18289  19.06494
6  -0.04293   0.29977  32.09964
6  -0.05990   0.52335  21.70084
1  -0.15145   0.78108  26.11264
1  -0.06139   0.17501  14.38174
6  -0.02828   0.44843  17.50034
1  -0.12307   0.71581  28.59564
6  -0.04420   0.64166  25.92594
6  -0.00039   0.36203  24.05534
8  -0.01989   0.45262  20.34344
6   0.05347   0.03759  18.53824
1  -0.03010   0.16618  24.65684
6  -0.01098   0.57956  28.41714
1  -0.08872   0.65783  31.10984
1  -0.00980   0.13742  22.23224
6   0.02509   0.52319  30.93864
1  -0.00499   0.27828  26.89674
1   0.03485   0.22398  29.41474
7   0.07298   0.40515  16.18364
1   0.03146   0.41836  33.06234
1   0.07395   0.16744  31.95664
1   0.13831   0.01060  17.56954
1   0.08586   0.83926  14.78314
1   0.17259   0.62387  18.03444
1   0.16595   0.71801  21.94454
1   0.24956   0.20320  19.13154
1   0.20533   0.79894  25.85354
1   0.24711   0.53105  24.02474
1   0.23630   0.74493  28.38044
```

114

```
8    0.27358    0.92008    15.31514
6    0.33056    0.67487    15.61684
1    0.27174    0.68971    30.89764
1    0.40319    0.60424    14.71154
1    0.51988    0.77062    16.33344
```

PC21 - C$_6$

```
5.035   5.035   120.000
57
26    0.94548    0.85818     2.51475
26    0.60598    0.17765     7.04083
26    0.94655    0.85879     6.41049
26    0.61546    0.18388    11.03680
26    0.26016    0.53432    11.45387
26    0.60500    0.17694     4.23543
26    0.26453    0.51764     4.66575
26    0.26682    0.51714     8.65952
26    0.94463    0.85746     9.27075
26    0.91678    0.84463    12.95595
 8    0.97556    0.51745     3.39119
 8    0.57548    0.51401    10.09433
 8    0.26418    0.20696     3.39119
 8    0.26856    0.84187    10.09485
 8    0.57466    0.82810     3.39119
 8    0.97696    0.20645    10.12103
 8    0.63577    0.85894     7.84870
 8    0.94717    0.54711     7.85111
 8    0.23440    0.14802     7.83670
 8    0.28806    0.19061    12.45133
 8    0.91946    0.18039     5.59768
 8    0.59453    0.87816    12.28556
 8    0.60205    0.48813     5.60029
 8    0.92677    0.50393    12.31921
 8    0.29432    0.88435     5.59950
 6    0.65956    0.67794    26.58885
 1    0.61684    0.44830    26.90285
 6    0.85308    0.78061    25.31895
 1    1.07538    0.79238    25.51925
 6    0.68897    0.56079    24.15395
 6    0.88908    0.66553    22.89345
 1    1.10098    0.65390    23.06845
 6    0.71510    0.47232    21.67555
 6    0.91783    0.59329    20.42905
 8    1.13739    0.50165    20.45215
 7    0.73985    0.49509    19.18465
 6    0.94792    0.62774    18.03165
 1    1.05236    0.48381    17.80025
 1    1.13637    0.86402    18.27035
 6    0.78365    0.65590    16.78535
 8    0.99536    0.78451    15.73315
 1    1.11579    1.00891    15.89745
 6    0.51683    0.34772    16.32595
 1    0.60137    0.18893    16.05375
 1    0.34826    0.24676    17.15805
```

115

```
8    0.37848    0.39627   15.20655
1    0.16116    0.22982   15.19555
1    0.68691    0.80717   17.02545
1    0.59569    0.58898   19.21145
1    0.63609    0.22477   21.82595
1    0.51177    0.49887   21.54625
1    0.95536    0.90787   22.67715
1    0.63503    0.32437   24.41745
1    0.47071    0.55891   23.95805
1    0.89882    1.01419   25.04865
1    0.43660    0.66723   26.42145
1    0.78305    0.84469   27.40385
```

Stearic acid

```
5.07751242  5.10759708  120.284097
81
26  −0.00552    0.38023    4.01049
26  −0.33697   −0.28519    8.01231
26  −0.00560    0.38167    7.41611
26  −0.33926   −0.29180   12.06501
26   0.34834    0.05030   12.48587
26  −0.33913   −0.28568    5.17733
26   0.32850    0.04847    5.58670
26   0.32649    0.04701    9.65107
26  −0.00171    0.38486   10.29987
26   0.00535    0.40071   14.03713
 8   0.00873    0.03963    4.29562
 8  −0.35665    0.04409   11.11914
 8   0.33676   −0.26206    4.29487
 8   0.32990    0.35504   11.13675
 8  −0.36110    0.36840    4.29675
 8   0.02449   −0.25264   11.11149
 8  −0.30960    0.38305    8.85002
 8  −0.00407    0.07761    8.83520
 8   0.30228   −0.31269    8.84565
 8   0.35591   −0.27650   13.37597
 8  −0.02761   −0.28414    6.55607
 8  −0.32457    0.40399   13.29194
 8  −0.33892    0.02524    6.55025
 8  −0.00480    0.03028   13.50423
 8   0.35162    0.40473    6.55062
 8  −0.10713    0.37480   15.88412
 8  −0.11191   −0.18991   15.82366
 6  −0.21101   −0.45126   16.29097
 6  −0.46257    0.42198   17.29767
 6   0.46925   −0.34198   17.86899
 6   0.22364   −0.47273   18.94946
 6   0.15677   −0.23322   19.49847
 6  −0.07929   −0.35170   20.62238
 1   0.01547    0.33686   18.52969
 1   0.29373    0.43272   19.76778
 1   0.37014   −0.03831   19.85592
 1   0.07988   −0.14644   18.67601
 1  −0.28677    0.44181   20.30969
```

```
6  -0.14493  -0.18546  20.91194
1   0.00779  -0.40862  21.51222
1  -0.04848  -0.08423  14.40125
1  -0.32161  -0.15186  18.27912
1   0.40057  -0.24618  17.05462
1  -0.40824   0.30632  18.07454
1   0.33625   0.24231  16.77915
1  -0.22599  -0.09361  20.14950
1   0.04870   0.02000  21.39864
6  -0.41353  -0.32415  21.93720
1  -0.61756  -0.52216  21.48288
6  -0.50354  -0.09154  22.37311
1  -0.34876  -0.40351  22.85352
1  -0.57858  -0.01624  21.48250
1  -0.30227   0.10791  22.82609
6  -0.76412  -0.22837  23.39567
1  -0.96571  -0.42778  22.94407
6  -0.85297   0.00484  23.82797
1  -0.69041  -0.30478  24.28890
1  -0.92694   0.08128  22.93563
1  -0.65113   0.20425  24.27829
6  -1.11281  -0.13135  24.85364
1  -1.31483  -0.33067  24.40392
6  -1.20100   0.10220  25.28818
1  -1.03870  -0.20787  25.74529
1  -1.27528   0.17870  24.39705
1  -0.99882   0.30151  25.73704
6  -1.46040  -0.03371  26.31610
1  -1.66269  -0.23297  25.86765
6  -1.54823   0.20003  26.75203
1  -1.38603  -0.11025  27.20681
1  -1.62268   0.27657  25.86160
1  -1.34586   0.39930  27.20006
6  -1.80738   0.06429  27.78109
1  -2.00985  -0.13495  27.33344
6  -1.89493   0.29816  28.21702
1  -1.73292  -0.01224  28.67157
1  -1.97047   0.37507  27.33213
1  -1.69371   0.49767  28.66891
6  -2.15274   0.16395  29.24173
1  -2.35880  -0.03322  28.80823
1  -2.21126   0.33798  29.53876
1  -2.08146   0.08965  30.14760
```

Oleic acid

```
5.10008388   5.09734037  120.458828
79
26  -0.00415   0.38167   4.01049
26  -0.33649  -0.28627   8.01231
26  -0.00422   0.38312   7.41611
26  -0.33880  -0.29291  12.06501
26   0.34698   0.05049  12.48587
26  -0.33865  -0.28677   5.17733
26   0.32721   0.04866   5.58670
```

117

```
26   0.32521   0.04719    9.65107
26  -0.00034   0.38633   10.29987
26   0.00675   0.40223   14.03713
 8   0.00883   0.03978    4.29562
 8  -0.35491   0.04426   11.11914
 8   0.33434  -0.26306    4.29487
 8   0.32970   0.35639   11.13675
 8  -0.35820   0.36980    4.29675
 8   0.02349  -0.25360   11.11149
 8  -0.30687   0.38451    8.85002
 8  -0.00377   0.07790    8.83520
 8   0.29984  -0.31388    8.84565
 8   0.35336  -0.27755   13.37597
 8  -0.02850  -0.28522    6.55607
 8  -0.32170   0.40553   13.29194
 8  -0.33733   0.02533    6.55025
 8  -0.00467   0.03039   13.50423
 8   0.35150   0.40627    6.55062
 8  -0.10533   0.37623   15.88412
 8  -0.11208  -0.19063   15.82366
 6  -0.21168  -0.45298   16.29097
 6  -0.45903   0.42358   17.29767
 6   0.46596  -0.34328   17.86899
 6   0.22097  -0.47453   18.94946
 6   0.15525  -0.23410   19.49847
 6  -0.08018  -0.35304   20.62238
 1   0.01660   0.33814   18.52969
 1   0.29396   0.43436   19.76778
 1   0.36837  -0.03846   19.85592
 1   0.07901  -0.14700   18.67601
 1  -0.28394   0.44349   20.30969
 6  -0.15169  -0.11212   21.12630
 1   0.00631  -0.41018   21.51222
 1  -0.04857  -0.08455   14.40125
 1  -0.32073  -0.15243   18.27912
 1   0.39793  -0.24711   17.05462
 1  -0.40535   0.30748   18.07454
 1   0.33562   0.24323   16.77915
 1  -0.21274  -0.00423   20.32290
 1   0.05641   0.06777   21.63420
 6  -0.41794  -0.25984   22.10039
 1  -0.79295  -0.37603   24.07575
 1  -0.70680  -0.29783   26.51249
 1  -0.53784  -0.25579   28.88192
 1  -0.35427  -0.21113   31.28147
 6  -0.63194  -0.13291   23.98450
 6  -0.52076  -0.06020   26.31364
 1  -0.17108  -0.15570   33.70606
 6  -0.34930  -0.01974   28.68176
 6  -0.43308  -0.03007   22.98006
 6  -0.61171   0.06733   25.12320
 1  -0.31196  -0.06591   26.03267
 1  -0.83124   0.05841   25.29564
 6  -0.16558   0.02389   31.06817
 6  -0.44813   0.12563   27.59283
```

```
1  −0.14834  −0.03128  28.32645
1  −0.65179   0.13346  27.92592
6   0.01588   0.07746  33.45925
6  −0.26500   0.16596  29.97308
1   0.03543   0.01225  30.71813
1  −0.46567   0.17721  30.32672
6  −0.08280   0.21446  32.35055
1   0.21969   0.06775  33.14530
1  −0.28329   0.22646  32.70224
1   0.07352   0.22105  34.37000
1  −0.43116   0.30793  24.93856
1  −0.25892   0.36089  27.39123
1  −0.07542   0.40049  29.76153
1   0.10637   0.44928  32.14136
1  −0.37563  −0.40381  22.80394
1  −0.63539  −0.40790  21.56539
1  −0.26429   0.21114  22.88793
```

PC21

```
5.02511587  5.06166562  119.441950
91
26  −0.43501   0.41502   3.85539
26   0.23087  −0.24969   7.89532
26  −0.43752   0.41358   7.30340
26   0.23887  −0.24636  11.95874
26  −0.10563   0.10154  12.39265
26   0.23006  −0.25287   5.05831
26  −0.10391   0.08145   5.46388
26  −0.10255   0.07980   9.54884
26  −0.44046   0.41571  10.19750
26  −0.46394   0.39201  14.07814
8   −0.42426   0.07090   4.16613
8    0.19918   0.07757  11.01128
8   −0.09517  −0.22911   4.16317
8   −0.10103   0.40029  11.02929
8    0.20572   0.39990   4.16359
8   −0.40697  −0.21906  11.02562
8    0.25693   0.41689   8.74050
8   −0.43801   0.10961   8.73777
8   −0.13279  −0.28049   8.72695
8   −0.08864  −0.23546  13.42993
8   −0.45972  −0.25142   6.43470
8    0.23225   0.43631  13.21619
8    0.22821   0.05760   6.43902
8   −0.46142   0.06528  13.27246
8   −0.08051   0.43711   6.42909
1    0.04400  −0.17020  14.22308
1    0.42505  −0.02223  16.65603
1   −0.16729   0.15434  18.35349
1    0.04323   0.38322  15.69973
6    0.42392   0.19145  16.84396
6   −0.07687   0.39708  18.16097
1    0.16511   0.49745  17.91899
8   −0.10285   0.46868  15.72674
```

```
1    0.29269    0.16156   17.76374
6   -0.24697    0.44380   17.00071
8    0.29378    0.26359   15.74210
8    0.38446   -0.30845   20.10406
7   -0.09899   -0.45220   19.36331
6    0.13149   -0.31664   20.25147
1   -0.29533   -0.44580   19.55198
1   -0.24335   -0.33953   17.14233
1    0.07755   -0.10119   37.68492
6    0.07337   -0.17779   21.47888
1    0.20146    0.25740   23.42197
1    0.04215   -0.11284   24.16525
6    0.14789   -0.27035   37.95160
6    0.25208    0.07552   23.71939
1    0.48993    0.09844   35.85783
1   -0.05400   -0.47551   38.34537
1    0.35770    0.48774   25.74790
1    0.09110   -0.45061   35.95600
6    0.33935   -0.04304   22.47774
1    0.19029    0.10986   26.41661
6    0.27298   -0.35243   36.72419
6    0.40476    0.30247   26.02633
6   -0.44652   -0.07519   36.14194
1    0.32337   -0.17526   38.74823
1   -0.10550    0.28866   34.03135
1    0.49464   -0.30231   28.12493
1    0.49212   -0.25909   34.14136
6   -0.49517    0.19716   24.78058
1   -0.45521    0.14365   21.99951
1    0.31705    0.31683   28.69925
6   -0.46278   -0.49146   28.37980
6   -0.32507   -0.16143   34.90648
1    0.39307   -0.22220   22.78443
6   -0.04412    0.11308   34.30917
1   -0.26466    0.02351   36.91275
1    0.29437    0.47529   32.18854
1    0.33504    0.47281   37.00696
6   -0.35316    0.41296   27.13375
1   -0.28392    0.38873   24.36277
1   -0.11006   -0.07193   32.30569
1   -0.44528    0.01420   25.06742
6    0.07378    0.02509   33.06784
6    0.35495    0.29916   32.46761
1    0.13959    0.21019   35.07006
6   -0.22423   -0.38553   29.46488
1   -0.13752   -0.39308   26.76206
1   -0.26364   -0.33681   35.18756
1    0.28326    0.10592   30.49449
1   -0.30709    0.22698   27.41111
6    0.47126    0.21078   31.22207
1   -0.00706   -0.18602   29.23454
6   -0.24966    0.48258   30.66316
1   -0.46084    0.39652   33.22663
1    0.13470   -0.15085   33.34532
1   -0.04917   -0.41822   31.30549
```

```
1  -0.46464    0.03686   31.49073
1   0.01834   -0.00061   21.15577
1  -0.13051   -0.35937   21.99027
```

A.1.3   Input Data file - frequency calculation

```
SLAB
1
5.07751242 5.10759708 120.284097
45
26 -5.517972850174E-03 3.802281675416E-01 4.010489872788E+00
26 -3.369661224252E-01 -2.851880189801E-01 8.012310532315E+00
26 -5.599558654049E-03 3.816682849945E-01 7.416106850176E+00
26 -3.392648248193E-01 -2.918009954659E-01 1.206500705006E+01
26 3.483390121640E-01 5.029953387311E-02 1.248587479904E+01
26 -3.391340980311E-01 -2.856805793021E-01 5.177334636424E+00
26 3.284967393465E-01 4.847324910621E-02 5.586696139379E+00
26 3.264917178214E-01 4.701488884920E-02 9.651071487158E+00
26 -1.712352137535E-03 3.848645444861E-01 1.029987099552E+01
26 5.350102432589E-03 4.007116360247E-01 1.403712707479E+01
8 8.726616450211E-03 3.962637607725E-02 4.295615723861E+00
8 -3.566438114775E-01 4.409029475554E-02 1.111913728524E+01
8 3.367630889194E-01 -2.620649146678E-01 4.294868258711E+00
8 3.299048954242E-01 3.550396111328E-01 1.113675087586E+01
8 -3.611048739346E-01 3.683979924841E-01 4.296751848693E+00
8 2.449322262628E-02 -2.526424898142E-01 1.111149331944E+01
8 -3.095973006872E-01 3.830512063953E-01 8.850015941626E+00
8 -4.066380864388E-03 7.760873491664E-02 8.835202502154E+00
8 3.022813273348E-01 -3.126908706355E-01 8.845650050048E+00
8 3.559128332767E-01 -2.764993893642E-01 1.337596679086E+01
8 -2.761417024459E-02 -2.841402820292E-01 6.556072599373E+00
8 -3.245659220190E-01 4.039940273075E-01 1.329193664378E+01
8 -3.389169968587E-01 2.523665016223E-02 6.550252818242E+00
8 -4.797289303686E-03 3.027826109469E-02 1.350422705265E+01
8 3.516204420187E-01 4.047255999953E-01 6.550618341913E+00
8 -1.071319018276E-01 3.748009696884E-01 1.588412453616E+01
8 -1.119069204730E-01 -1.899099911538E-01 1.582365821638E+01
6 -2.110117582406E-01 -4.512597429768E-01 1.629096995091E+01
6 -4.625702388544E-01 4.219769402146E-01 1.729766800281E+01
6 4.692482756978E-01 -3.419839984750E-01 1.786899184123E+01
6 2.236366777107E-01 -4.727324182975E-01 1.894945960275E+01
6 1.567688786535E-01 -2.332160893429E-01 1.949846541342E+01
6 -7.928769900256E-02 -3.516984530448E-01 2.062238180181E+01
1 1.547288624010E-02 3.368615534154E-01 1.852968863347E+01
1 2.937293517852E-01 4.327187724449E-01 1.976778100325E+01
1 3.701428518440E-01 -3.830976588955E-02 1.985591737612E+01
1 7.988410560370E-02 -1.464412576585E-01 1.867601072035E+01
1 -2.867733595290E-01 4.418100595241E-01 2.030969009004E+01
1 -1.449280363932E-01 -1.854627121612E-01 2.091194309130E+01
1 7.792649890003E-03 -4.086214641635E-01 2.151221699846E+01
1 -4.848214461353E-02 -8.423234668425E-02 1.440124990502E+01
1 -3.216149542838E-01 -1.518558512727E-01 1.827911848342E+01
1 4.005715938279E-01 -2.461748598463E-01 1.705461693138E+01
1 -4.082382017199E-01 3.063190218654E-01 1.807453981965E+01
1 3.362496201772E-01 2.423101148761E-01 1.677914809199E+01
```

```
FREQCALC
INTENS
NUMDERIV
2
INTRAMAN
INTCPHF
ENDFREQ
END
BASISSET
POB-DZVP
UHF
DFT
SPIN
B3LYP-D3
XLGRID
ENDdft
SHRINK
8 8
TOLDEE
8
SPINLOCK
0 15
SCFDIR
LEVSHIFT
3 0
FMIXING
30
TOLINTEG
8 8 8 8 16
MAXCYCLE
100000
EXCHSIZE
10000000
BIPOSIZE
10000000
ATOMSPIN
10
 1 -1
 2 -1
 3 -1
 4 -1
 5 -1
 6  1
 7  1
 8  1
 9  1
10 1
ENDscf
```

A.2   CP2K input files

A.2.1   Input Data file - DFT-MD run

```
&GLOBAL
```

```
    PRINT_LEVEL  LOW
    PROJECT_NAME DYN
    RUN_TYPE  MD
    WALLTIME 43200
  &END GLOBAL
  &MOTION
    &MD
      ENSEMBLE  NVT
      STEPS  100000000
      TIMESTEP      3.9999999999999997E-01
      STEP_START_VAL  0
      TIME_START_VAL    4.9959999999996871E+03
      ECONS_START_VAL   -1.5468927605338276E+03
      TEMPERATURE   4.2300000000000000E+02
      TEMP_TOL   3.0000000000000000E+01
      &THERMOSTAT
        TYPE  CSVR
        REGION  GLOBAL
        &CSVR
          TIMECON    1.5000000000000000E+02
          &THERMOSTAT_ENERGY
               4.2136587904207032E-02
          &END THERMOSTAT_ENERGY
          &RNG_INIT
Wiener process for Thermostat # 1  1 F T F
4.8459704247838659E-01  1997187044.0
4044397199.0  538280735.0  2172583236.0  101348787.0  3275455522.0
12345.0  12345.0 12345.0  12345.0  12345.0  12345.0  12345.0  12345.0
12345.0  12345.0  12345.0  12345.0
          &END RNG_INIT
        &END CSVR
      &END THERMOSTAT
      &AVERAGES  T
        &RESTART_AVERAGES
          ITIMES_START  1
          AVECPU    4.4935808242331397E+01
          AVEHUGONIOT    0.0000000000000000E+00
          AVETEMP_BARO    0.0000000000000000E+00
          AVEPOT    -1.5468936370213969E+03
          AVEKIN    8.8281856621039739E-02
          AVETEMP    4.2238139682919609E+02
          AVEKIN_QM    0.0000000000000000E+00
          AVETEMP_QM    0.0000000000000000E+00
          AVEVOL    4.5117944632962326E+03
          AVECELL_A    9.5862188474140844E+00
          AVECELL_B    9.5856001498301620E+00
          AVECELL_C    5.6691783986576191E+01
          AVEALPHA    9.0000000000000000E+01
          AVEBETA    9.0000000000000000E+01
          AVEGAMMA    1.1999270885018561E+02
          AVE_ECONS    1.2046616057533713E+03
          AVE_PRESS    0.0000000000000000E+00
          AVE_PXX    0.0000000000000000E+00
        &END RESTART_AVERAGES
      &END AVERAGES
    &END MD
    &PRINT
      &TRAJECTORY  SILENT
        &EACH
          MD  1
        &END EACH
      &END TRAJECTORY
      &VELOCITIES  SILENT
        &EACH
          MD  1
        &END EACH
      &END VELOCITIES
      &RESTART  SILENT
        BACKUP_COPIES  1
```

123

```
        &EACH
          MD  1
        &END EACH
      &END RESTART
      &RESTART_HISTORY  SILENT
        &EACH
          MD  1000
        &END EACH
      &END RESTART_HISTORY
    &END PRINT
  &END MOTION
  &FORCE_EVAL
    METHOD  QS
    &DFT
      BASIS_SET_FILE_NAME ./BASIS_MOLOPT
      BASIS_SET_FILE_NAME ./BASIS_ADMM
      POTENTIAL_FILE_NAME ./GTH_POTENTIALS
      WFN_RESTART_FILE_NAME ./old-RESTART.wfn
      UKS  T
      &SCF
        MAX_SCF  150
        EPS_SCF     2.9999999999999999E-07
        SCF_GUESS  RESTART
        &OT  T
          MINIMIZER  DIIS
          PRECONDITIONER  FULL_KINETIC
        &END OT
        &OUTER_SCF  T
          EPS_SCF     5.9999999999999997E-07
          MAX_SCF  30
        &END OUTER_SCF
        &PRINT
          &RESTART  SILENT
            BACKUP_COPIES  1
          &END RESTART
        &END PRINT
      &END SCF
      &AUXILIARY_DENSITY_MATRIX_METHOD
        ADMM_PURIFICATION_METHOD  MO_DIAG
        METHOD  BASIS_PROJECTION
      &END AUXILIARY_DENSITY_MATRIX_METHOD
      &QS
        EPS_DEFAULT     1.0000000000000000E-13
        EXTRAPOLATION  ASPC
        EXTRAPOLATION_ORDER  2
      &END QS
      &MGRID
        NGRIDS  5
        CUTOFF     4.0000000000000000E+02
        REL_CUTOFF     4.0000000000000000E+01
      &END MGRID
      &XC
        DENSITY_CUTOFF     1.0000000000000000E-10
        GRADIENT_CUTOFF     1.0000000000000000E-10
        TAU_CUTOFF     1.0000000000000000E-10
        &XC_GRID
          XC_SMOOTH_RHO  NN10
          XC_DERIV  NN10_SMOOTH
        &END XC_GRID
        &XC_FUNCTIONAL  NO_SHORTCUT
          &BECKE88  T
            SCALE_X     7.1999999999999997E-01
          &END BECKE88
          &LYP  T
            SCALE_C     8.1000000000000005E-01
          &END LYP
          &VWN  T
            SCALE_C     1.9000000000000000E-01
            FUNCTIONAL_TYPE  VWN5
```

```
              &END VWN
              &XALPHA  T
                SCALE_X      8.0000000000000002E-02
              &END XALPHA
            &END XC_FUNCTIONAL
            &HF
              FRACTION     2.0000000000000001E-01
              &SCREENING
                EPS_SCHWARZ    1.0000000000000000E-10
              &END SCREENING
              &INTERACTION_POTENTIAL
                POTENTIAL_TYPE  TRUNCATED
                CUTOFF_RADIUS    2.0000000000000000E+00
                T_C_G_DATA ./t_c_g.dat
              &END INTERACTION_POTENTIAL
              &MEMORY
                EPS_STORAGE_SCALING    1.0000000000000001E-01
                MAX_MEMORY  900
              &END MEMORY
            &END HF
            &VDW_POTENTIAL
              POTENTIAL_TYPE  PAIR_POTENTIAL
              &PAIR_POTENTIAL
                TYPE  DFTD3
                PARAMETER_FILE_NAME ./dftd3.dat
                REFERENCE_FUNCTIONAL BLYP
                CALCULATE_C9_TERM   T
                REFERENCE_C9_TERM   T
              &END PAIR_POTENTIAL
            &END VDW_POTENTIAL
          &END XC
          &PRINT
            &MOMENTS  SILENT
              ADD_LAST  NUMERIC
              COMMON_ITERATION_LEVELS  1
              FILENAME DIPOLES
              REFERENCE  COAC
              MAX_MOMENT  1
            &END MOMENTS
          &END PRINT
        &END DFT
        &SUBSYS
          &CELL
A    4.3933576099500007E+00   -2.5360984403800000E+00    0.0000000000000000E+00
B    2.9239009051299999E-04    5.0724811215200027E+00    0.0000000000000000E+00
C    0.0000000000000000E+00    0.0000000000000000E+00    3.0000000000000011E+01
            MULTIPLE_UNIT_CELL  1 1 1
          &END CELL
          &COORD
Fe_surf_up
 -2.0337327455753442E+00   -2.9813335143910065E+00    2.7079607923324436E+00
Fe_up   -3.5590918472898938E+00   -1.9557850462239393E-01    6.8345482884941422E+00
Fe_up   -2.1129988989281299E+00   -2.7430988716714029E+00    6.0626645216419117E+00
Fe_up   -3.2334946454889188E+00   -8.5217065943799991E-02    1.0702586184190532E+01
Fe_up   -4.6912506544459381E-01    4.4150254770190488E-02    1.1462968147306658E+01
Fe_down   -3.4178727569911005E+00   -3.6340034266610216E-01    3.5727500865977762E+00
Fe_down   -5.3953115154069065E-01   -2.4372615696548539E-01    4.4822123781065502E+00
Fe_down   -6.7937940740549796E-01   -2.0883657092972821E-01    8.2631682631010221E+00
Fe_down   -2.0513813074186826E+00   -2.6789285382203532E+00    9.3423541081487169E+00
Fe_surf_down
-2.0052384864755179E+00   -2.7266073019776447E+00    1.3069049233975635E+01
O   -1.8506037387483556E+00    3.3890460774953779E-01    3.0301899380758792E+00
O    7.6167765405917620E-01   -9.1812189604351924E-01    9.9785545891361842E+00
O   -4.6460601776875637E-01   -2.1000785726208635E+00    2.9506763288061983E+00
O   -5.0046517577782335E-01    1.4899720856998899E+00    9.7792754765305077E+00
O    9.1496628058733454E-01    4.9543050998912502E-01    2.7978982267359918E+00
O   -1.9238430991972297E+00   -8.7409141960873749E-01    9.9054192755973745E+00
O    9.7371586500563856E-01    6.8126947744553590E-01    7.7282329423644729E+00
O   -2.0396800387475160E+00    7.8726126457906176E-01    7.6547054207538769E+00
```

```
O    -6.7362792126524829E-01   -1.8372582989319193E+00    7.5276150649713029E+00
O    -5.4747569493924064E-01   -1.7052900468440846E+00    1.2746395931185040E+01
O    -2.1368593778084870E+00   -1.1122766811664082E+00    5.0794492588644991E+00
O     1.0052942861532517E+00    7.9126719003330392E-01    1.2154323742870181E+01
O     8.6853094890576943E-01   -1.1326900394869719E+00    5.3569625163008459E+00
O    -2.0502970470167408E+00    7.7866419614703342E-01    1.2099243275060919E+01
O    -6.0430453145067409E-01    1.4103149548562792E+00    5.3866585630687212E+00
H    -2.9765488066029624E+00   -3.0519958089653558E+00    2.1248472541697488E+01
H    -1.1792966218894396E+00   -2.4861489747224423E+00    1.8040771033551987E+01
H    -3.0774949948325898E+00   -5.2913092083309534E+00    1.7099309689014536E+01
C    -2.1559884874567974E+00   -2.8527443754078456E+00    2.0556771153378055E+01
H    -3.0679312126248002E+00   -3.9056903773960143E+00    1.8978448917797312E+01
C    -1.0122601966293863E+00   -3.5166969414566833E+00    1.8437839006878281E+01
H    -1.2515090183602200E+00   -2.6467142436007220E+00    2.1073996639485490E+01
O_chain  -3.4679772302433278E+00   -4.9446869238227471E+00    1.4601636482422126E+01
C    -2.0573343108598889E+00   -3.8644989739965934E+00    1.9513127167814392E+01
H    -7.9970622138441050E-01   -5.5974489019969091E+00    1.7390721764691559E+01
C    -2.4784268389188293E+00   -4.4710517296316050E+00    1.6737925584245644E+01
H    -2.4480145141869034E+00   -1.9615375318703694E+00    1.9973473615027576E+01
C    -1.0785380788609975E+00   -4.5233974007835034E+00    1.7236643360705038E+01
H    -7.4271774803404036E-02   -3.5391041298160992E+00    1.8950810170571550E+01
C    -2.7009275646535236E+00   -4.2485255020116393E+00    1.5299258208197124E+01
H    -2.8208407192820011E+00   -3.4792473654149663E+00    1.7099139978740499E+01
H    -1.8888524004496581E+00   -4.8309460170356173E+00    2.0033154890146715E+01
H    -3.3506699134068191E-01   -4.0932418053288169E+00    1.6544641503252254E+01
O_chain  -2.1967709088292930E+00   -3.0671132069429641E+00    1.4922556894097260E+01
H     1.9223613903801881E-01   -1.8110055297898948E+00    1.3364567988153679E+01
        &END COORD
        &VELOCITY
-2.2980021206644073E-05    1.5542994526563365E-04   -1.2113782475360606E-04
-5.0996586893007425E-06    1.6876936525683876E-05    9.4196798967281296E-05
-1.0684992432033976E-04    1.8646989744582733E-05    1.1559201320281680E-04
 1.4417448581985933E-05   -6.8184237909110499E-05   -2.9525376715881833E-05
-6.5666000657506674E-05   -3.0423765193269675E-05    1.6165500094421202E-05
-1.2053884199283515E-04   -1.4117374312839358E-05    1.3093874159804891E-04
 5.3307761158844764E-05   -1.6607310233497297E-04   -1.5728562897308204E-04
-1.2568703950591341E-04    3.9591118508887531E-06   -2.8801737752282003E-04
-2.4680592507150064E-05    1.1830542831606724E-04    1.4765436355822033E-04
 1.0228980744741374E-04   -2.2373836738897859E-05    1.8200469719449006E-04
-4.6312360049778342E-05    6.9720307657846902E-05    4.2303393761077040E-04
 1.0778818062550646E-04    4.0480001497051058E-05   -9.6215598358763246E-07
 3.1289019788647958E-04   -2.6166686446991321E-04    1.2923083171764691E-04
 5.7989055969694262E-05   -1.0659364199285422E-04    1.9772700674934032E-04
-2.3745154664534372E-04   -1.0305794636537330E-04    8.6268311615153462E-05
 5.5406519787682665E-04   -4.2284576680874383E-07   -3.1369504842810138E-05
-2.3692145480981336E-04    1.1523431434447118E-04   -1.0440951837585110E-04
 1.8094780091796675E-04   -3.0529737607538942E-04    1.9461485875413504E-04
 2.7768931628797104E-04   -1.3041418285654258E-07   -2.7751395617034967E-04
 1.8990530574745891E-05    1.8028548320977615E-04   -1.9490446202972416E-04
-3.1945226164850794E-04    2.6076318755884124E-04    6.3232194558420177E-05
-1.0929478244937743E-04   -1.2173217252201403E-04   -6.7055193574009213E-05
-6.6123653422228538E-06    9.6556823471212553E-05    5.3436013755677511E-04
 1.1996445726575623E-04   -1.9934621540171753E-04   -2.7008861531462210E-04
-2.2125847716080008E-04    1.1781062791654505E-04   -7.2672556424108301E-04
 3.9850683039762987E-05    8.2323419597651003E-04   -1.0469175426699431E-03
 3.2126809746595972E-04    9.8435167892468867E-04    8.1659214079440835E-04
-3.6825765298899326E-05   -1.3737959091238536E-03    6.7785393172706320E-04
-1.1941110073405676E-04    2.7259218668460234E-04   -4.6442053060569990E-04
-2.1783796474183412E-05   -4.2850829677654992E-04   -4.8985111970552579E-04
-9.3785565467209323E-05    3.8625936729300516E-04    5.7783358670259765E-05
-1.2825859844126374E-04    1.1681545182047265E-03    1.0162591889208933E-03
 1.2476235133936165E-04   -2.9659088575768763E-04    1.8917820917042043E-04
 4.3979123388169772E-05   -6.9835480513326473E-05   -1.5220784455148529E-04
-1.5520378340192457E-04    4.5636509993415088E-04   -2.3265738212957052E-04
-4.1591964536162463E-05   -4.2693822725054261E-05    4.1752972361626983E-05
 9.4117924243464028E-04   -3.3789322094993410E-04   -4.6977233474273638E-04
 6.8580595749062899E-05   -4.4274006736792098E-04   -3.7535974792224570E-04
 2.7723568471954004E-04    3.1521660238616319E-04    2.8744359545053138E-05
-3.1868653219635325E-05   -3.9474441755710964E-04   -2.2415896425267528E-04
```

126

```
-1.0817738936804210E-03    1.7072216942995045E-04   -3.1962268060098701E-04
 5.3705459438443211E-04    4.9517472129014385E-04   -3.4309291553731640E-04
 1.2610211262774550E-03    3.1485737801901983E-04   -2.6727059814034477E-04
-7.0348320140906851E-05   -2.6241824671857121E-05    2.0757234003929614E-04
 2.5808755677644249E-04    1.1078574914294675E-03    3.1027010272723352E-05
      &END VELOCITY
      &KIND Fe_up
        BASIS_SET DZVP-MOLOPT-SR-GTH-q16
        BASIS_SET AUX_FIT cFIT11
        POTENTIAL GTH-BLYP-q16
        &POTENTIAL
4 6 6
0.3600000000000000E+00 2  0.7011025100000000E+01 -0.2227466700000000E+00
3
0.2762053300000000E+00 2  0.6114959800000001E+00  0.7992357330000000E+01
-0.1031808895000000E+02
0.2471300500000000E+00 2 -0.8710555919999999E+01  0.8684169239999999E+01
-0.1027524761000000E+02
0.2235339800000000E+00 1 -0.1241150401000000E+02
        &END POTENTIAL
        &DFT_PLUS_U  T
          L  2
          U_MINUS_J     1.4699730161045235E-01
        &END DFT_PLUS_U
        &BS   T
          &ALPHA
            NEL  4 -2
            L  2 0
            N  3 4
          &END ALPHA
          &BETA
            NEL  -6 -2
            L  2 0
            N  3 4
          &END BETA
        &END BS
      &END KIND
      &KIND Fe_down
        BASIS_SET DZVP-MOLOPT-SR-GTH-q16
        BASIS_SET AUX_FIT cFIT11
        POTENTIAL GTH-BLYP-q16
        &POTENTIAL
4 6 6
0.3600000000000000E+00 2  0.7011025100000000E+01 -0.2227466700000000E+00
3
0.2762053300000000E+00 2  0.6114959800000001E+00  0.7992357330000000E+01
-0.1031808895000000E+02
0.2471300500000000E+00 2 -0.8710555919999999E+01  0.8684169239999999E+01
-0.1027524761000000E+02
0.2235339800000000E+00 1 -0.1241150401000000E+02
        &END POTENTIAL
        &DFT_PLUS_U  T
          L  2
          U_MINUS_J     1.4699730161045235E-01
        &END DFT_PLUS_U
        &BS   T
          &ALPHA
            NEL  -6 -2
            L  2 0
            N  3 4
          &END ALPHA
          &BETA
            NEL  4 -2
            L  2 0
            N  3 4
          &END BETA
        &END BS
      &END KIND
      &KIND C
```

127

```
        BASIS_SET DZVP-MOLOPT-SR-GTH-q4
        BASIS_SET AUX_FIT cpFIT3
        POTENTIAL GTH-BLYP-q4
        &POTENTIAL
2 2
0.3380660900000000E+00 2 -0.9136268710000000E+01  0.1429259560000000E+01
2
0.3023222300000000E+00 1  0.9665512280000000E+01
0.2863791200000000E+00 0
        &END POTENTIAL
     &END KIND
     &KIND O
        BASIS_SET DZVP-MOLOPT-SR-GTH-q6
        BASIS_SET AUX_FIT cpFIT3
        POTENTIAL GTH-BLYP-q6
        &POTENTIAL
2 4
0.2434202600000000E+00 2 -0.1699189235000000E+02  0.2566142060000000E+01
2
0.2208314000000000E+00 1  0.1838885102000000E+02
0.2172007000000000E+00 0
        &END POTENTIAL
        &BS  T
          &ALPHA
            NEL  2
            L  1
            N  2
          &END ALPHA
          &BETA
            NEL  2
            L  1
            N  2
          &END BETA
        &END BS
     &END KIND
     &KIND Fe_surf_down
        BASIS_SET DZVP-MOLOPT-SR-GTH-q16
        BASIS_SET AUX_FIT cFIT11
        ELEMENT Fe
        POTENTIAL GTH-BLYP-q16
        &POTENTIAL
4 6 6
0.3600000000000000E+00 2  0.7011025100000000E+01 -0.2227466700000000E+00
3
0.2762053300000000E+00 2  0.6114959800000001E+00  0.7992357330000000E+01
-0.1031808895000000E+02
0.2471300500000000E+00 2 -0.8710555919999999E+01  0.8684169239999999E+01
-0.1027524761000000E+02
0.2235339800000000E+00 1 -0.1241150401000000E+02
        &END POTENTIAL
        &DFT_PLUS_U  T
          L  2
          U_MINUS_J     1.4699730161045235E-01
        &END DFT_PLUS_U
        &BS  T
          &ALPHA
            NEL  -4 -2
            L  2 0
            N  3 4
          &END ALPHA
          &BETA
            NEL  4 -2
            L  2 0
            N  3 4
          &END BETA
        &END BS
     &END KIND
     &KIND Fe_surf_up
        BASIS_SET DZVP-MOLOPT-SR-GTH-q16
```

```
        BASIS_SET AUX_FIT cFIT11
        ELEMENT Fe
        POTENTIAL GTH-BLYP-q16
        &POTENTIAL
4 6 6
0.3600000000000000E+00 2  0.7011025100000000E+01 -0.2227466700000000E+00
3
0.2762053300000000E+00 2  0.6114959800000001E+00  0.7992357330000000E+01
-0.1031808895000000E+02
0.2471300500000000E+00 2 -0.8710555919999999E+01  0.8684169239999999E+01
-0.1027524761000000E+02
0.2235339800000000E+00 1 -0.1241150401000000E+02
        &END POTENTIAL
        &DFT_PLUS_U  T
          L  2
          U_MINUS_J     1.4699730161045235E-01
        &END DFT_PLUS_U
        &BS  T
          &ALPHA
            NEL  4 -2
            L  2 0
            N  3 4
          &END ALPHA
          &BETA
            NEL  -4 -2
            L  2 0
            N  3 4
          &END BETA
        &END BS
      &END KIND
      &KIND O_chain
        BASIS_SET DZVP-MOLOPT-SR-GTH-q6
        BASIS_SET AUX_FIT cpFIT3
        POTENTIAL GTH-BLYP-q6
        &POTENTIAL
2 4
0.2434202600000000E+00 2 -0.1699189235000000E+02  0.2566142060000000E+01
2
0.2208314000000000E+00 1  0.1838885102000000E+02
0.2172007000000000E+00 0
        &END POTENTIAL
      &END KIND
      &KIND H
        BASIS_SET DZVP-MOLOPT-SR-GTH-q1
        BASIS_SET AUX_FIT cpFIT3
        POTENTIAL GTH-BLYP-q1
        &POTENTIAL
1
0.2000000000000000E+00 2 -0.4195961470000000E+01  0.7304982100000000E+00
0
        &END POTENTIAL
      &END KIND
      &TOPOLOGY
        NUMBER_OF_ATOMS  45
        MULTIPLE_UNIT_CELL  1 1 1
      &END TOPOLOGY
    &END SUBSYS
  &END FORCE_EVAL
```

A.3 LAMMPS input files

A.3.1 Input Data file - adsorbed hexanoic acid on hematite

```
45 atoms
 19 bonds
```

```
 33 angles
 42 dihedrals
 1 impropers
 7 atom types
 8 bond types
 11 angle types
 11 dihedral types
 1 improper types
 -1.411500 3.661310  xlo xhi
 0.580420 4.973640  ylo yhi
 -6.438855 23.561145  zlo zhi
 -2.535681 0.000000 0.000000 xy xz yz
Bond Coeffs
1 268 1.529 # C-C
2 268 1.529 # C-C2
3 317 1.522 # C-C3
4 340 1.090 # C-H
5 340 1.090 # C2-H
6 656 1.250 # C3-O2
7 553 0.960 # H-O
8 130.0 2.116 # Fe-O
Angle Coeffs
1 58.35 112.70 # C-C-C
2 58.35 112.70 # C-C-C2
3 63.00 111.10 # C-C-C3
4 37.50 110.70 # C-C-H
5 37.50 110.70 # C-C2-H
6 70.00 117.00 # C-C3-O2
7 37.50 110.70 # C2-C-H
8 35.00 109.50 # C3-C-H
9 33.00 107.80 # H-C-H
10 33.00 107.80 # H-C2-H
11 80.00 126.00 # O2-C3-O2
Dihedral Coeffs
1  1.740  0.157  0.279  0.000 # C-C-C-C
2  1.740  0.157  0.279  0.000 # C-C-C-C2
3 -3.185  0.825  0.493  0.000  # C-C-C-C3
4  0.000  0.000  0.366  0.000 # C-C-C-H
5  0.000  0.000  0.366  0.000 # C-C-C2-H
6  0.000 -0.820  0.000  0.000 # C-C-C3-O2
7  0.000  0.000  0.366  0.000 # C2-C-C-H
8  0.000  0.000 -0.225  0.000 # C3-C-C-H
9  0.000  0.000  0.318  0.000 # H-C-C-H
10  0.000  0.000  0.318  0.000 # H-C-C2-H
11  0.000  0.000  0.000  0.000 # H-C-C3-O2
 Improper Coeffs
1 10.500      -1      2  # C-O2-C3-O2
 Masses
 1 12.010700 # C
 2 12.010700 # C2
 3 12.010700 # C3
 4 55.845001 # Fe
 5 1.007940 # H
 6 15.999400 # O
 7 15.999400 # O2
```

```
 Atoms
1 1 4 3.000000 −1.658273 −2.929476 3.172149 # Fe
2 1 4 3.000000 −3.116549 −0.404919 7.293750 # Fe
3 1 4 3.000000 −1.653842 −2.938560 6.512067 # Fe
4 1 4 3.000000 −3.110206 −0.393480 11.222521 # Fe
5 1 4 3.000000 −0.252545 −0.288292 11.977078 # Fe
6 1 4 3.000000 −3.120737 −0.394024 4.080563 # Fe
7 1 4 3.000000 −0.191593 −0.399918 4.952095 # Fe
8 1 4 3.000000 −0.189537 −0.416337 8.842369 # Fe
9 1 4 3.000000 −1.676303 −2.942323 9.645297 # Fe
10 1 4 3.000000 −1.795989 −2.979748 13.465688 # Fe
11 1 6 −2.000000 −1.590148 0.379562 3.406489 # O
12 1 6 −2.000000 1.174639 −1.227929 10.376303 # O
13 1 6 −2.000000 −0.164676 −1.989973 3.409102 # O
14 1 6 −2.000000 −0.207371 1.213406 10.436533 # O
15 1 6 −2.000000 1.175304 0.430579 3.404874 # O
16 1 6 −2.000000 −1.600977 −1.208231 10.410455 # O
17 1 6 −2.000000 1.344681 0.406936 8.091213 # O
18 1 6 −2.000000 −1.656662 0.519385 8.086652 # O
19 1 6 −2.000000 −0.259247 −2.141663 8.073245 # O
20 1 6 −2.000000 −0.192296 −2.112421 12.775674 # O
21 1 6 −2.000000 −1.735790 −1.206915 5.728033 # O
22 1 6 −2.000000 1.222640 0.501063 12.729763 # O
23 1 6 −2.000000 1.277735 −1.332253 5.728045 # O
24 1 6 −2.000000 −1.789187 0.432847 12.717906 # O
25 1 6 −2.000000 −0.119093 1.336838 5.726348 # O
26 1 5 0.074000 0.617932 2.004364 19.150087 # H
27 1 5 0.074000 0.224958 0.554434 17.048847 # H
28 1 5 0.074000 −1.023191 2.688251 21.486464 # H
29 1 1 −0.148000 −0.322122 1.643089 19.656034 # C
30 1 7 −0.800000 0.158826 −1.012541 15.067466 # O2
31 1 5 0.074000 −0.485446 3.779944 20.207697 # H
32 1 2 −0.222000 −1.000622 2.824814 20.397917 # C2
33 1 5 0.900000 0.243496 −1.889198 13.671751 # H
34 1 5 0.074000 0.028839 0.877344 20.379169 # H
35 1 1 −0.148000 −0.512824 −0.001968 17.671101 # C
36 1 5 0.074000 −1.751354 1.718125 18.000111 # H
37 1 1 −0.148000 −1.235949 0.964457 18.624140 # C
38 1 5 0.074000 0.077742 −0.741332 18.239664 # H
39 1 3 0.700000 −0.826333 −1.522866 15.662167 # C3
40 1 5 0.074000 −2.078159 0.082843 16.179384 # H
41 1 1 −0.148000 −1.504783 −0.700533 16.729174 # C
42 1 5 0.074000 −2.048099 2.945862 20.058216 # H
43 1 5 0.074000 −2.055166 0.419944 19.166010 # H
44 1 7 −0.800000 −1.349213 −2.692109 15.332362 # O2
45 1 5 0.074000 −2.265601 −1.306231 17.275349 # H
 Bonds
1 7 20 33
2 4 26 29
3 4 27 35
4 5 28 32
5 1 29 37
6 4 29 34
7 2 29 32
8 6 30 39
```

```
9 5 31 32
10 5 32 42
11 1 35 41
12 4 35 38
13 1 35 37
14 4 36 37
15 4 37 43
16 3 39 41
17 6 39 44
18 4 40 41
19 4 41 45
 Angles
1 4 26 29 37
2 9 26 29 34
3 7 26 29 32
4 4 34 29 37
5 2 32 29 37
6 7 32 29 34
7 5 28 32 29
8 10 28 32 31
9 10 28 32 42
10 5 29 32 31
11 5 29 32 42
12 10 31 32 42
13 4 27 35 41
14 9 27 35 38
15 4 27 35 37
16 4 38 35 41
17 1 37 35 41
18 4 37 35 38
19 1 29 37 35
20 4 29 37 36
21 4 29 37 43
22 4 35 37 36
23 4 35 37 43
24 9 36 37 43
25 6 30 39 41
26 11 30 39 44
27 6 41 39 44
28 3 35 41 39
29 4 35 41 40
30 4 35 41 45
31 8 39 41 40
32 8 39 41 45
33 9 40 41 45
 Dihedrals
1 4 26 29 37 35
2 9 26 29 37 36
3 9 26 29 37 43
4 4 34 29 37 35
5 9 34 29 37 36
6 9 34 29 37 43
7 2 32 29 37 35
8 7 32 29 37 36
9 7 32 29 37 43
```

```
10 10 26 29 32 28
11 10 26 29 32 31
12 10 26 29 32 42
13 5 37 29 32 28
14 5 37 29 32 31
15 5 37 29 32 42
16 10 34 29 32 28
17 10 34 29 32 31
18 10 34 29 32 42
19 8 27 35 41 39
20 9 27 35 41 40
21 9 27 35 41 45
22 8 38 35 41 39
23 9 38 35 41 40
24 9 38 35 41 45
25 3 37 35 41 39
26 4 37 35 41 40
27 4 37 35 41 45
28 4 27 35 37 29
29 9 27 35 37 36
30 9 27 35 37 43
31 1 41 35 37 29
32 4 41 35 37 36
33 4 41 35 37 43
34 4 38 35 37 29
35 9 38 35 37 36
36 9 38 35 37 43
37 6 30 39 41 35
38 11 30 39 41 40
39 11 30 39 41 45
40 6 44 39 41 35
41 11 44 39 41 40
42 11 44 39 41 45
 Impropers
1 1 41 30 39 44
```

A.3.2   Input Data file - squalane

```
  92 atoms
 91 bonds
 180 angles
 261 dihedrals
 0 impropers
Coords
1 -7.757820 2.443920 -0.847260 # C
2 -6.289970 2.592200 -1.270420 # C
3 -8.416020 3.024920 -1.528200 # H
4 -7.907130 2.809400 0.191760 # H
5 -8.068210 1.378400 -0.898780 # H
6 -5.395500 1.732390 -0.346390 # C
7 -5.482720 2.093330 0.702590 # H
8 -3.915000 1.717640 -0.763190 # C
9 -5.769260 0.684880 -0.385150 # H
10 -3.509620 2.744190 -0.694150 # H
11 -3.836990 1.359770 -1.813080 # H
```

133

```
12 -3.100530 0.782880 0.148210 # C
13 -3.169140 1.137490 1.200730 # H
14 -1.611580 0.642800 -0.261140 # C
15 -3.568490 -0.225260 0.091760 # H
16 -0.951520 -0.434150 0.638170 # C
17 -0.977260 -0.103990 1.700520 # H
18 0.494900 -0.779900 0.242330 # C
19 -1.551120 -1.367690 0.551610 # H
20 1.130690 0.115840 0.365070 # H
21 0.512380 -1.103420 -0.821330 # H
22 1.044400 -1.916830 1.121940 # C
23 1.035420 -1.599160 2.188370 # H
24 2.468120 -2.387570 0.727630 # C
25 0.354430 -2.783240 1.013420 # H
26 2.834830 -3.624970 1.586460 # C
27 2.862380 -3.341020 2.662010 # H
28 4.168260 -4.284350 1.194340 # C
29 2.036050 -4.387870 1.450390 # H
30 5.009150 -3.580950 1.362970 # H
31 4.135640 -4.560070 0.117320 # H
32 4.421810 -5.546820 2.029600 # C
33 4.454640 -5.271180 3.106640 # H
34 5.754880 -6.206690 1.637080 # C
35 3.580720 -6.249970 1.861010 # H
36 6.554120 -5.444290 1.773140 # H
37 5.726840 -6.490330 0.561460 # H
38 6.121080 -7.444710 2.495300 # C
39 6.143420 -7.132270 3.563120 # H
40 7.544110 -7.916590 2.099800 # C
41 5.083300 -8.573170 2.331870 # C
42 8.235080 -7.050990 2.208410 # H
43 7.551990 -8.233570 1.033160 # H
44 8.092970 -9.054840 2.978110 # C
45 8.076850 -8.732160 4.042050 # H
46 9.538500 -9.402380 2.580620 # C
47 7.455910 -9.949630 2.855190 # H
48 10.139630 -8.469860 2.667500 # H
49 9.562670 -9.731560 1.517930 # H
50 10.197720 -10.481360 3.478140 # C
51 11.685940 -10.623660 3.066870 # C
52 12.155820 -9.616450 3.123920 # H
53 11.752620 -10.977180 2.013850 # H
54 12.499780 -11.561070 3.976130 # C
55 13.979700 -11.578250 3.557390 # C
56 14.355620 -10.531540 3.597000 # H
57 14.064830 -11.938020 2.507830 # H
58 14.873630 -12.441090 4.479120 # C
59 16.341221 -12.295270 4.054200 # C
60 16.653860 -11.230460 4.106690 # H
61 16.488400 -12.659710 3.014510 # H
62 16.999121 -12.878510 4.733510 # H
63 -5.901580 4.079300 -1.250400 # C
64 -6.196930 2.215580 -2.313210 # H
65 -5.974980 4.489880 -0.220450 # H
66 -6.579450 4.658120 -1.913590 # H
```

```
67 -4.871590 4.232880 -1.629390 # H
68 -0.869250 1.991070 -0.169050 # C
69 -1.573620 0.285810 -1.314450 # H
70 -0.888150 2.376770 0.872590 # H
71 -1.320020 2.746090 -0.842140 # H
72 0.183190 1.895210 -0.499880 # H
73 3.504790 -1.258160 0.891360 # C
74 2.446710 -2.700440 -0.340080 # H
75 3.550990 -0.920910 1.948840 # H
76 3.262220 -0.391600 0.245930 # H
77 4.512910 -1.588010 0.573200 # H
78 14.482180 -13.927370 4.457680 # C
79 14.782740 -12.065650 5.522520 # H
80 15.159760 -14.508450 5.119190 # H
81 14.553370 -14.336760 3.427100 # H
82 13.452390 -14.079370 4.837850 # H
83 9.452950 -11.828270 3.385590 # C
84 10.161590 -10.125380 4.531850 # H
85 9.469920 -12.212980 2.343560 # H
86 8.401070 -11.730960 3.717810 # H
87 9.903160 -12.584740 4.057420 # H
88 12.092340 -12.586750 3.906340 # H
89 12.423800 -11.204330 5.026550 # H
90 5.036070 -8.910010 1.274300 # H
91 4.075690 -8.242630 2.650900 # H
92 5.325470 -9.440160 2.976860 # H
Types
1 2
2 1
3 5
4 5
5 5
6 1
7 5
8 1
9 5
10 5
11 5
12 1
13 5
14 1
15 5
16 1
17 5
18 1
19 5
20 5
21 5
22 1
23 5
24 1
25 5
26 1
27 5
28 1
```

135

```
29 5
30 5
31 5
32 1
33 5
34 1
35 5
36 5
37 5
38 1
39 5
40 1
41 2
42 5
43 5
44 1
45 5
46 1
47 5
48 5
49 5
50 1
51 1
52 5
53 5
54 1
55 1
56 5
57 5
58 1
59 2
60 5
61 5
62 5
63 2
64 5
65 5
66 5
67 5
68 2
69 5
70 5
71 5
72 5
73 2
74 5
75 5
76 5
77 5
78 2
79 5
80 5
81 5
82 5
83 2
```

```
84 5
85 5
86 5
87 5
88 5
89 5
90 5
91 5
92 5
Charges
1 -0.222000
2 -0.074000
3 0.074000
4 0.074000
5 0.074000
6 -0.148000
7 0.074000
8 -0.148000
9 0.074000
10 0.074000
11 0.074000
12 -0.148000
13 0.074000
14 -0.074000
15 0.074000
16 -0.148000
17 0.074000
18 -0.148000
19 0.074000
20 0.074000
21 0.074000
22 -0.148000
23 0.074000
24 -0.074000
25 0.074000
26 -0.148000
27 0.074000
28 -0.148000
29 0.074000
30 0.074000
31 0.074000
32 -0.148000
33 0.074000
34 -0.148000
35 0.074000
36 0.074000
37 0.074000
38 -0.074000
39 0.074000
40 -0.148000
41 -0.222000
42 0.074000
43 0.074000
44 -0.148000
45 0.074000
```

```
46 −0.148000
47 0.074000
48 0.074000
49 0.074000
50 −0.074000
51 −0.148000
52 0.074000
53 0.074000
54 −0.148000
55 −0.148000
56 0.074000
57 0.074000
58 −0.074000
59 −0.222000
60 0.074000
61 0.074000
62 0.074000
63 −0.222000
64 0.074000
65 0.074000
66 0.074000
67 0.074000
68 −0.222000
69 0.074000
70 0.074000
71 0.074000
72 0.074000
73 −0.222000
74 0.074000
75 0.074000
76 0.074000
77 0.074000
78 −0.222000
79 0.074000
80 0.074000
81 0.074000
82 0.074000
83 −0.222000
84 0.074000
85 0.074000
86 0.074000
87 0.074000
88 0.074000
89 0.074000
90 0.074000
91 0.074000
92 0.074000
 Bonds
1 4 1 5
2 4 1 3
3 1 1 2
4 4 1 4
5 1 2 6
6 4 2 64
7 2 2 63
```

```
 8  4  6  9
 9  1  6  8
10  4  6  7
11  4  8  11
12  4  8  10
13  1  8  12
14  4  12  13
15  4  12  15
16  1  12  14
17  4  14  69
18  1  14  16
19  2  14  68
20  4  16  19
21  1  16  18
22  4  16  17
23  1  18  22
24  4  18  20
25  4  18  21
26  4  22  25
27  4  22  23
28  1  22  24
29  4  24  74
30  1  24  26
31  2  24  73
32  4  26  29
33  1  26  28
34  4  26  27
35  4  28  31
36  4  28  30
37  1  28  32
38  4  32  33
39  4  32  35
40  1  32  34
41  4  34  37
42  4  34  36
43  1  34  38
44  2  38  41
45  4  38  39
46  1  38  40
47  4  40  43
48  4  40  42
49  1  40  44
50  7  41  92
51  7  41  91
52  7  41  90
53  1  44  46
54  4  44  45
55  4  44  47
56  4  46  48
57  1  46  50
58  4  46  49
59  1  50  51
60  4  50  84
61  2  50  83
62  4  51  53
```

```
63  4  51  52
64  1  51  54
65  4  54  89
66  1  54  55
67  4  54  88
68  4  55  56
69  4  55  57
70  1  55  58
71  4  58  79
72  1  58  59
73  2  58  78
74  4  59  60
75  4  59  61
76  4  59  62
77  7  63  67
78  7  63  65
79  7  63  66
80  7  68  70
81  7  68  72
82  7  68  71
83  7  73  76
84  7  73  77
85  7  73  75
86  7  78  81
87  7  78  80
88  7  78  82
89  7  83  85
90  7  83  86
91  7  83  87
 Angles
1  9  3  1  5
2  4  2  1  5
3  9  4  1  5
4  4  2  1  3
5  9  3  1  4
6  4  2  1  4
7  1  1  2  6
8  4  1  2  64
9  2  1  2  63
10  4  6  2  64
11  2  6  2  63
12  7  63  2  64
13  4  2  6  9
14  1  2  6  8
15  4  2  6  7
16  4  8  6  9
17  9  7  6  9
18  4  7  6  8
19  4  6  8  11
20  4  6  8  10
21  1  6  8  12
22  9  10  8  11
23  4  11  8  12
24  4  10  8  12
25  4  8  12  13
```

```
26  4  8  12  15
27  1  8  12  14
28  9  13  12  15
29  4  13  12  14
30  4  14  12  15
31  4  12  14  69
32  1  12  14  16
33  2  12  14  68
34  4  16  14  69
35  7  68  14  69
36  2  16  14  68
37  4  14  16  19
38  1  14  16  18
39  4  14  16  17
40  4  18  16  19
41  9  17  16  19
42  4  17  16  18
43  1  16  18  22
44  4  16  18  20
45  4  16  18  21
46  4  20  18  22
47  4  21  18  22
48  9  20  18  21
49  4  18  22  25
50  4  18  22  23
51  1  18  22  24
52  9  23  22  25
53  4  24  22  25
54  4  23  22  24
55  4  22  24  74
56  1  22  24  26
57  2  22  24  73
58  4  26  24  74
59  7  73  24  74
60  2  26  24  73
61  4  24  26  29
62  1  24  26  28
63  4  24  26  27
64  4  28  26  29
65  9  27  26  29
66  4  27  26  28
67  4  26  28  31
68  4  26  28  30
69  1  26  28  32
70  9  30  28  31
71  4  31  28  32
72  4  30  28  32
73  4  28  32  33
74  4  28  32  35
75  1  28  32  34
76  9  33  32  35
77  4  33  32  34
78  4  34  32  35
79  4  32  34  37
80  4  32  34  36
```

```
81  1  32  34  38
82  9  36  34  37
83  4  37  34  38
84  4  36  34  38
85  2  34  38  41
86  4  34  38  39
87  1  34  38  40
88  7  39  38  41
89  2  40  38  41
90  4  39  38  40
91  4  38  40  43
92  4  38  40  42
93  1  38  40  44
94  9  42  40  43
95  4  43  40  44
96  4  42  40  44
97  5  38  41  92
98  5  38  41  91
99  5  38  41  90
100  10  91  41  92
101  10  90  41  92
102  10  90  41  91
103  1  40  44  46
104  4  40  44  45
105  4  40  44  47
106  4  45  44  46
107  4  46  44  47
108  9  45  44  47
109  4  44  46  48
110  1  44  46  50
111  4  44  46  49
112  4  48  46  50
113  9  48  46  49
114  4  49  46  50
115  1  46  50  51
116  4  46  50  84
117  2  46  50  83
118  4  51  50  84
119  2  51  50  83
120  7  83  50  84
121  4  50  51  53
122  4  50  51  52
123  1  50  51  54
124  9  52  51  53
125  4  53  51  54
126  4  52  51  54
127  4  51  54  89
128  1  51  54  55
129  4  51  54  88
130  4  55  54  89
131  9  88  54  89
132  4  55  54  88
133  4  54  55  56
134  4  54  55  57
135  1  54  55  58
```

```
136 9 56 55 57
137 4 56 55 58
138 4 57 55 58
139 4 55 58 79
140 1 55 58 59
141 2 55 58 78
142 4 59 58 79
143 7 78 58 79
144 2 59 58 78
145 4 58 59 60
146 4 58 59 61
147 4 58 59 62
148 9 60 59 61
149 9 60 59 62
150 9 61 59 62
151 5 2 63 67
152 5 2 63 65
153 5 2 63 66
154 10 65 63 67
155 10 66 63 67
156 10 65 63 66
157 5 14 68 70
158 5 14 68 72
159 5 14 68 71
160 10 70 68 72
161 10 70 68 71
162 10 71 68 72
163 5 24 73 76
164 5 24 73 77
165 5 24 73 75
166 10 76 73 77
167 10 75 73 76
168 10 75 73 77
169 5 58 78 81
170 5 58 78 80
171 5 58 78 82
172 10 80 78 81
173 10 81 78 82
174 10 80 78 82
175 5 50 83 85
176 5 50 83 86
177 5 50 83 87
178 10 85 83 86
179 10 85 83 87
180 10 86 83 87
 Dihedrals
1 4 5 1 2 6
2 9 5 1 2 64
3 7 5 1 2 63
4 4 3 1 2 6
5 9 3 1 2 64
6 7 3 1 2 63
7 4 4 1 2 6
8 9 4 1 2 64
9 7 4 1 2 63
```

```
10 4 1 2 6 9
11 1 1 2 6 8
12 4 1 2 6 7
13 9 64 2 6 9
14 4 64 2 6 8
15 9 64 2 6 7
16 7 63 2 6 9
17 2 63 2 6 8
18 7 63 2 6 7
19 5 1 2 63 67
20 5 1 2 63 65
21 5 1 2 63 66
22 5 6 2 63 67
23 5 6 2 63 65
24 5 6 2 63 66
25 10 64 2 63 67
26 10 64 2 63 65
27 10 64 2 63 66
28 4 2 6 8 11
29 4 2 6 8 10
30 1 2 6 8 12
31 9 9 6 8 11
32 9 9 6 8 10
33 4 9 6 8 12
34 9 7 6 8 11
35 9 7 6 8 10
36 4 7 6 8 12
37 4 6 8 12 13
38 4 6 8 12 15
39 1 6 8 12 14
40 9 11 8 12 13
41 9 11 8 12 15
42 4 11 8 12 14
43 9 10 8 12 13
44 9 10 8 12 15
```

A.3.3   MD simulation - 1 m/s | 300K | 2 inversions of motion

Note: here only the input file for the simulation at 1 m/s relative velocity and 300 K temperature is shown. The other input files are simply obtained by changing the relative parameters in the provided input file.

```
units real
processors 4 4 1
atom_style full
bond_style      harmonic
angle_style     harmonic
dihedral_style  opls
pair_style  hybrid lj/cut/coul/long 10.0 buck/coul/long 10.0
special_bonds lj 0.0 0.0 0.5 coul 0.0 0.0 0.5
improper_style cvff
pair_modify shift yes mix geometric table 0
boundary p p p
box tilt large
```

```
read_restart ../restart10x10_pressure
#----------------------------
kspace_style    pppm 1e-5
pair_coeff 1 1 lj/cut/coul/long 0.060 3.50 # C C2
pair_coeff 2 2 lj/cut/coul/long 0.060 3.50 # C2
pair_coeff 3 3 lj/cut/coul/long 0.015 3.75 # C3
pair_coeff 5 5 lj/cut/coul/long 0.030 2.50 # H
pair_coeff 7 7 lj/cut/coul/long 0.210 2.96 # O2
pair_coeff 1 4 lj/cut/coul/long 0.159640    2.774887
pair_coeff 2 4 lj/cut/coul/long 0.159640    2.774887
pair_coeff 3 4 lj/cut/coul/long 0.079820    2.872281
pair_coeff 4 5 lj/cut/coul/long 0.112883    2.345208
pair_coeff 4 7 lj/cut/coul/long 0.298660    2.551862
pair_coeff 1 6 lj/cut/coul/long 0.100965    3.218695
pair_coeff 2 6 lj/cut/coul/long 0.100965    3.218695
pair_coeff 3 6 lj/cut/coul/long 0.050483    3.331666
pair_coeff 5 6 lj/cut/coul/long 0.071393    2.720294
pair_coeff 6 7 lj/cut/coul/long 0.188889    2.960000
pair_coeff 4 4 buck/coul/long 0.0 1.0 0.0
pair_coeff 4 6 buck/coul/long 2.5422e+04 0.3299 0.0
pair_coeff 6 6 buck/coul/long 5.2495e+05 0.149 6.4293e+02
#-------------------------------
timestep 0.5
thermo_style custom #args
thermo 1000
change_box all z final 0 90
group top id
1:9000:90 6:9000:90 7:9000:90 11:9000:90 15:9000:90 25:9000:90
group bottom id
46:9000:90 51:9000:90 52:9000:90 56:9000:90 60:9000:90 70:9000:90
group rest subtract all top bottom
reset_timestep 0
fix 1 rest nvt temp 300 300 40
fix 2 top move linear 0.000005 0.0 0.0
fix 3 bottom move linear -0.000005 0.0 0.0
dump 1 all custom 1000 move.lammpstrj id element q xu yu zu
dump_modify 1 element C1 C2 C3 Fe H O O2 sort id
run 1000000
write_restart restartforward
unfix 2
unfix 3
fix 2 top move linear -0.000005 0.0 0.0
fix 3 bottom move linear 0.000005 0.0 0.0
run 2000000
write_restart restartbackward
unfix 2
unfix 3
fix 2 top move linear 0.000005 0.0 0.0
fix 3 bottom move linear -0.000005 0.0 0.0
run 2000000
write_restart restartforward2
```

A.3.4   Input Data file - adsorbed stearic acid on hematite

```
 81 atoms
```

```
 55 bonds
 105 angles
 150 dihedrals
 1 impropers
 7 atom types
 5 bond types
 7 angle types
 7 dihedral types
 1 improper types
-6.898112 -1.798028  xlo xhi
 0.795297 5.189173  ylo yhi
-8.031564 41.968436  zlo zhi
-2.583940 0.000000 0.000000 xy xz yz
Bond Coeffs
1 268 1.529 # C-C
2 317 1.522 # C-C3
3 340 1.090 # C-H
4 656 1.250 # C3-O2
5 553 0.960 # H-O
Angle Coeffs
1 58.35 112.70 # C-C-C
2 63.00 111.10 # C-C-C3
3 37.50 110.70 # C-C-H
4 35.00 109.50 # C3-C-H
5 70.00 117.00 # C-C3-O2
6 33.00 107.80 # H-C-H
7 80.00 126.00 # O2-C3-O2
Dihedral Coeffs
1  1.740  0.157  0.279  0.000 # C-C-C-C
2 -3.185  0.825  0.493  0.000  # C-C-C-C3
3  0.000  0.000  0.366  0.000 # C-C-C-H
4  0.000 -0.820  0.000  0.000 # C-C-C3-O2
5  0.000  0.000 -0.225  0.000 # C3-C-C-H
6  0.000  0.000  0.318  0.000 # H-C-C-H
7  0.000  0.000  0.000  0.000 # H-C-C3-O2
Improper Coeffs
1 10.500       -1       2  # C-O2-C3-O2
 Masses
 1 12.010700 # C
 2 12.010700 # C2
 3 12.010700 # C3
 4 55.845001 # Fe
 5 1.007940 # H
 6 15.999400 # O
 7 15.999400 # O2
 Atoms # full
1 1 4 3.000000 3.838640 1.460410 3.538320 # Fe
2 1 4 3.000000 1.288080 2.924420 7.537580 # Fe
3 1 4 3.000000 3.842910 1.468040 6.941190 # Fe
4 1 4 3.000000 1.297790 2.896980 11.589360 # Fe
5 1 4 3.000000 1.402810 0.000750 12.009110 # Fe
6 1 4 3.000000 1.278240 2.930030 4.702650 # Fe
7 1 4 3.000000 1.305690 0.000800 5.112500 # Fe
8 1 4 3.000000 -1.286750 4.389080 9.174760 # Fe
9 1 4 3.000000 3.855470 1.472020 9.824600 # Fe
```

```
10 1 4 3.000000 3.842740 1.541040 13.560470 # Fe
11 1 6 −2.000000 2.215370 4.358510 3.820930 # O
12 1 6 −2.000000 0.339350 4.370840 10.644750 # O
13 1 6 −2.000000 −0.431830 3.030930 3.822550 # O
14 1 6 −2.000000 0.522750 1.344470 10.658550 # O
15 1 6 −2.000000 2.062480 1.407960 3.822400 # O
16 1 6 −2.000000 3.051660 3.066300 10.636720 # O
17 1 6 −2.000000 2.290040 1.469030 8.374600 # O
18 1 6 −2.000000 4.635350 0.126000 8.361190 # O
19 1 6 −2.000000 −0.477580 2.807240 8.369220 # O
20 1 6 −2.000000 −0.296960 2.958920 12.902110 # O
21 1 6 −2.000000 2.864730 2.933730 6.080150 # O
22 1 6 −2.000000 2.157590 1.557770 12.815850 # O
23 1 6 −2.000000 0.479190 4.294720 6.073740 # O
24 1 6 −2.000000 2.171170 4.308720 13.023180 # O
25 1 6 −2.000000 0.504480 1.566430 6.079080 # O
26 1 5 0.074000 −10.052510 3.668330 26.746269 # H
27 1 1 −0.148000 −11.298490 5.052500 28.816380 # C
28 1 5 0.074000 −11.865210 4.171810 28.485270 # H
29 1 1 −0.148000 −12.263450 6.099640 29.370939 # C
30 1 5 0.074000 −10.638060 4.698110 29.616699 # H
31 1 5 0.074000 −12.920220 6.442850 28.564180 # H
32 1 2 −0.222000 −13.103380 5.576820 30.536039 # C2
33 1 5 0.074000 −13.637390 4.664500 30.247061 # H
34 1 5 0.074000 −13.851490 6.309040 30.860609 # H
35 1 5 0.074000 −12.474050 5.327880 31.398550 # H
36 1 5 0.074000 −4.634160 2.207800 21.555531 # H
37 1 1 −0.148000 −5.054160 4.119630 22.458599 # C
38 1 5 0.074000 −5.718820 4.470620 21.661880 # H
39 1 1 −0.148000 −5.884620 3.580480 23.619049 # C
40 1 5 0.074000 −6.438370 2.692900 23.286921 # H
41 1 1 −0.148000 −6.861880 4.606510 24.185471 # C
42 1 5 0.074000 −5.219880 3.230910 24.416370 # H
43 1 5 0.074000 −7.527420 4.955300 23.388580 # H
44 1 5 0.074000 −6.308360 5.494590 24.516661 # H
45 1 1 −0.148000 −7.690750 4.067310 25.347040 # C
46 1 5 0.074000 −8.244260 3.179200 25.015829 # H
47 1 1 −0.148000 −8.667740 5.092990 25.914730 # C
48 1 5 0.074000 −7.024830 3.718310 26.143629 # H
49 1 5 0.074000 −9.334690 5.441700 25.118860 # H
50 1 5 0.074000 −8.113700 5.981220 26.244829 # H
51 1 1 −0.148000 −9.494520 4.553380 27.078091 # C
52 1 1 −0.148000 −10.464280 5.582320 27.651390 # C
53 1 5 0.074000 −8.826650 4.199700 27.870550 # H
54 1 5 0.074000 −11.130460 5.935400 26.856119 # H
55 1 5 0.074000 −9.904090 6.467120 27.980400 # H
56 1 5 0.074000 −11.694880 6.983720 29.685181 # H
57 1 1 −0.148000 1.406590 1.649990 16.812481 # C
58 1 1 −0.148000 −0.455980 2.119740 18.445860 # C
59 1 5 0.074000 −1.003950 1.256300 18.050751 # H
60 1 5 0.074000 0.166080 1.731840 19.260250 # H
61 1 5 0.074000 −2.836740 1.725370 19.817341 # H
62 1 5 0.074000 0.865270 0.839340 16.304600 # H
63 1 1 −0.148000 0.432520 2.692620 17.347530 # C
64 1 1 −0.148000 −1.434660 3.146760 19.006510 # C
```

```
65 1 1 −0.148000 −2.276680 2.605520 20.157560 # C
66 1 5 0.074000 −0.878750 4.027530 19.353741 # H
67 1 5 0.074000 −2.084440 3.509140 18.202869 # H
68 1 1 −0.148000 −3.246050 3.634100 20.732700 # C
69 1 5 0.074000 −1.616590 2.242260 20.952749 # H
70 1 5 0.074000 −0.170800 3.079880 16.522310 # H
71 1 5 0.074000 −3.908770 3.994950 19.939480 # H
72 1 5 0.074000 −2.685300 4.514990 21.070629 # H
73 1 1 −0.148000 −4.078480 3.092910 21.890711 # C
74 1 5 0.074000 −3.415270 2.739400 22.687580 # H
75 1 5 0.074000 −4.499370 5.006430 22.791140 # H
76 1 7 −0.800000 3.331240 1.408170 15.404590 # O2
77 1 3 0.700000 2.371000 2.193460 15.811720 # C3
78 1 5 0.074000 1.973030 1.164370 17.611170 # H
79 1 7 −0.800000 2.229000 3.351880 15.348060 # O2
80 1 5 0.074000 2.252720 3.807600 13.920670 # H
81 1 5 0.074000 0.988950 3.553630 17.731649 # H
 Bonds
1 5 24 80
2 3 26 51
3 1 27 52
4 1 27 29
5 3 27 30
6 3 27 28
7 3 29 31
8 3 29 56
9 1 29 32
10 3 32 33
11 3 32 34
12 3 32 35
13 3 36 73
14 3 37 38
15 1 37 73
16 1 37 39
17 3 37 75
18 3 39 40
19 3 39 42
20 1 39 41
21 3 41 43
22 1 41 45
23 3 41 44
24 3 45 48
25 1 45 47
26 3 45 46
27 3 47 50
28 3 47 49
29 1 47 51
30 3 51 53
31 1 51 52
32 3 52 55
33 3 52 54
34 1 57 63
35 3 57 62
36 2 57 77
37 3 57 78
```

```
38 1 58 63
39 3 58 59
40 3 58 60
41 1 58 64
42 3 61 65
43 3 63 70
44 3 63 81
45 3 64 66
46 1 64 65
47 3 64 67
48 1 65 68
49 3 65 69
50 3 68 71
51 3 68 72
52 1 68 73
53 3 73 74
54 4 76 77
55 4 77 79
 Angles
1 1 29 27 52
2 3 30 27 52
3 3 28 27 52
4 3 29 27 30
5 3 28 27 29
6 6 28 27 30
7 3 27 29 31
8 3 27 29 56
9 1 27 29 32
10 6 31 29 56
11 3 31 29 32
12 3 32 29 56
13 3 29 32 33
14 3 29 32 34
15 3 29 32 35
16 6 33 32 34
17 6 33 32 35
18 6 34 32 35
19 3 38 37 73
20 3 38 37 39
21 6 38 37 75
22 1 39 37 73
23 3 73 37 75
24 3 39 37 75
25 3 37 39 40
26 3 37 39 42
27 1 37 39 41
28 6 40 39 42
29 3 40 39 41
30 3 41 39 42
31 3 39 41 43
32 1 39 41 45
33 3 39 41 44
34 3 43 41 45
35 6 43 41 44
36 3 44 41 45
```

```
37  3  41  45  48
38  1  41  45  47
39  3  41  45  46
40  3  47  45  48
41  6  46  45  48
42  3  46  45  47
43  3  45  47  50
44  3  45  47  49
45  1  45  47  51
46  6  49  47  50
47  3  50  47  51
48  3  49  47  51
49  3  26  51  47
50  6  26  51  53
51  3  26  51  52
52  3  47  51  53
53  1  47  51  52
54  3  52  51  53
55  1  27  52  51
56  3  27  52  55
57  3  27  52  54
58  3  51  52  55
59  3  51  52  54
60  6  54  52  55
61  3  62  57  63
62  2  63  57  77
63  3  63  57  78
64  4  62  57  77
65  6  62  57  78
66  4  77  57  78
67  3  59  58  63
68  3  60  58  63
69  1  63  58  64
70  6  59  58  60
71  3  59  58  64
72  3  60  58  64
73  1  57  63  58
74  3  57  63  70
75  3  57  63  81
76  3  58  63  70
77  3  58  63  81
78  6  70  63  81
79  3  58  64  66
80  1  58  64  65
81  3  58  64  67
82  3  65  64  66
83  6  66  64  67
84  3  65  64  67
85  3  61  65  64
86  3  61  65  68
87  6  61  65  69
88  1  64  65  68
89  3  64  65  69
90  3  68  65  69
91  3  65  68  71
```

```
92  3 65 68 72
93  1 65 68 73
94  6 71 68 72
95  3 71 68 73
96  3 72 68 73
97  3 36 73 37
98  3 36 73 68
99  6 36 73 74
100 1 37 73 68
101 3 37 73 74
102 3 68 73 74
103 5 57 77 76
104 5 57 77 79
105 7 76 77 79
 Dihedrals
1  1 29 27 52 51
2  3 29 27 52 55
3  3 29 27 52 54
4  3 30 27 52 51
5  6 30 27 52 55
6  6 30 27 52 54
7  3 28 27 52 51
8  6 28 27 52 55
9  6 28 27 52 54
10 3 52 27 29 31
11 3 52 27 29 56
12 1 52 27 29 32
13 6 30 27 29 31
14 6 30 27 29 56
15 3 30 27 29 32
16 6 28 27 29 31
17 6 28 27 29 56
18 3 28 27 29 32
19 3 27 29 32 33
20 3 27 29 32 34
21 3 27 29 32 35
22 6 31 29 32 33
23 6 31 29 32 34
24 6 31 29 32 35
25 6 56 29 32 33
26 6 56 29 32 34
27 6 56 29 32 35
28 6 38 37 73 36
29 3 38 37 73 68
30 6 38 37 73 74
31 3 39 37 73 36
32 1 39 37 73 68
33 3 39 37 73 74
34 6 75 37 73 36
35 3 75 37 73 68
36 6 75 37 73 74
37 6 38 37 39 40
38 6 38 37 39 42
39 3 38 37 39 41
40 3 73 37 39 40
```

```
41  3  73  37  39  42
42  1  73  37  39  41
43  6  75  37  39  40
44  6  75  37  39  42
45  3  75  37  39  41
46  3  37  39  41  43
47  1  37  39  41  45
48  3  37  39  41  44
49  6  40  39  41  43
50  3  40  39  41  45
51  6  40  39  41  44
52  6  42  39  41  43
53  3  42  39  41  45
54  6  42  39  41  44
55  3  39  41  45  48
56  1  39  41  45  47
57  3  39  41  45  46
58  6  43  41  45  48
59  3  43  41  45  47
60  6  43  41  45  46
61  6  44  41  45  48
62  3  44  41  45  47
63  6  44  41  45  46
64  3  41  45  47  50
65  3  41  45  47  49
66  1  41  45  47  51
67  6  48  45  47  50
68  6  48  45  47  49
69  3  48  45  47  51
70  6  46  45  47  50
71  6  46  45  47  49
72  3  46  45  47  51
73  3  45  47  51  26
74  3  45  47  51  53
75  1  45  47  51  52
76  6  50  47  51  26
77  6  50  47  51  53
78  3  50  47  51  52
79  6  49  47  51  26
80  6  49  47  51  53
81  3  49  47  51  52
82  3  26  51  52  27
83  6  26  51  52  55
84  6  26  51  52  54
85  1  47  51  52  27
86  3  47  51  52  55
87  3  47  51  52  54
88  3  53  51  52  27
89  6  53  51  52  55
90  6  53  51  52  54
91  3  62  57  63  58
92  6  62  57  63  70
93  6  62  57  63  81
94  2  77  57  63  58
95  5  77  57  63  70
```

```
96  5  77 57 63 81
97  3  78 57 63 58
98  6  78 57 63 70
99  6  78 57 63 81
100 4  63 57 77 76
101 4  63 57 77 79
102 7  62 57 77 76
103 7  62 57 77 79
104 7  78 57 77 76
105 7  78 57 77 79
106 3  59 58 63 57
107 6  59 58 63 70
108 6  59 58 63 81
109 3  60 58 63 57
110 6  60 58 63 70
111 6  60 58 63 81
112 1  64 58 63 57
113 3  64 58 63 70
114 3  64 58 63 81
115 3  63 58 64 66
116 1  63 58 64 65
117 3  63 58 64 67
118 6  59 58 64 66
119 3  59 58 64 65
120 6  59 58 64 67
121 6  60 58 64 66
122 3  60 58 64 65
123 6  60 58 64 67
124 3  58 64 65 61
125 1  58 64 65 68
126 3  58 64 65 69
127 6  66 64 65 61
128 3  66 64 65 68
129 6  66 64 65 69
130 6  67 64 65 61
131 3  67 64 65 68
132 6  67 64 65 69
133 6  61 65 68 71
134 6  61 65 68 72
135 3  61 65 68 73
136 3  64 65 68 71
137 3  64 65 68 72
138 1  64 65 68 73
139 6  69 65 68 71
140 6  69 65 68 72
141 3  69 65 68 73
142 3  65 68 73 36
143 1  65 68 73 37
144 3  65 68 73 74
145 6  71 68 73 36
146 3  71 68 73 37
147 6  71 68 73 74
148 6  72 68 73 36
149 3  72 68 73 37
150 6  72 68 73 74
```

Appendix A. Computational Details

```
 Impropers
1 1 57 76 77 79
```

List of Figures

List of Tables

Bibliography

[1] K. Holmberg and A. Erdemir. Influence of tribology on global energy consumption, costs and emissions. *Friction*, 5:263–284, 09 2017.

[2] H. Spikes. Friction modifier additives. *Tribology Letters*, 60, 10 2015.

[3] A. Schilling, G. Brace, and E.V. Paterson. *Automobile Engine Lubrication Vol. 2 of 'Motor Oils and Engine Lubrication'*. Scientific Publications (G.B.) Limited, 1972.

[4] L.R. Rudnick. *Lubricant Additives: Chemistry and Applications, Third Edition (3rd ed.)*. CRC Press, 2017.

[5] G.W. Stachowiak and A.W. Batchelor. 3 lubricants and their composition. In *Engineering TriBology*, volume 24 of *Tribology Series*, pages 59–119. Elsevier, 1993.

[6] S. Q. Abbas Rizvi. A comprehensive review of lubricant chemistry, technology, selection, and design. 2009.

[7] G. Tsagkaropoulou, C. P. Warrens, and P. J. Camp. Interactions between friction modifiers and dispersants in lubricants: The case of glycerol monooleate and polyisobutylsuccinimide-polyamine. *ACS Applied Materials & Interfaces*, 11(31):28359–28369, 2019. PMID: 31287656.

[8] I. Minami. Molecular science of lubricant additives. *Applied Sciences*, 7(5), 2017.

[9] O. Reynolds. Iv. on the theory of lubrication and its application to mr. beauchamp towers̀ experiments, including an experimental determination of the viscosity of olive oil. *Philosophical Transactions of the Royal Society of London*, 177:157–234, 1886.

[10] D. Zhu. *Elastohydrodynamic Lubrication (EHL)*, pages 874–889. Springer US, 2013.

[11] H. A. Spikes. Mixed lubrication – an overview. *Lubrication Science*, 9(3):221–253, 1997.

[12] H.A. Spikes. Boundary lubrication and boundary films. In D. Dowson, C.M. Taylor, T.H.C. Childs, M. Godet, and G. Dalmaz, editors, *Thin Films in Tribology*, volume 25 of *Tribology Series*, pages 331–346. Elsevier, 1993.

[13] BL Papke. Mineral oil base fluids. *Encyclopedia of Tribology; Wang, QJ, Chung, YW, Eds.; Springer: New York, NY, USA*, 4, 2013.

[14] R. L.. Stambaugh. *Viscosity index improvers and thickeners*, pages 144–180. Springer Netherlands, 1997.

[15] A. J Bridgewater and M. D Sexton. Mechanism of antioxidant action: reactions of alkyl and aryl sulphides with hydroperoxides. *Journal of the Chemical Society, Perkin Transactions 2*, (6):530–536, 1978.

[16] G.Scott. Developments in the photo-oxidation and photo-stabilisation of polymers. *Polymer Degradation and Stability*, 10(2):97–125, 1985.

[17] Jan Pospíšil. Aromatic and heterocyclic amines in polymer stabilization. 1995.

[18] M. Rasberger. *Oxidative degradation and stabilisation of mineral oil based lubricants*, pages 98–143. Springer Netherlands, 1997.

[19] C. C. Colyer and W. C. Gergel. *Detergents and dispersants*, pages 75–97. Springer Netherlands, 1997.

[20] M. Lattuada and M. Manni. Evolution of the additive technology for top tier lubricating oils: Use of calixarene detergents for fuel economy improvement. In *SAE Powertrains, Fuels & Lubricants Digital Summit*. SAE International, 2021.

[21] Z. Tang and S. Li. A review of recent developments of friction modifiers for liquid lubricants (2007–present). *Current Opinion in Solid State and Materials Science*, 18(3):119–139, 2014.

[22] R. Mountford Deeley. Discussion on lubrication. *Proceedings of the Physical Society of London*, 32(1):1s, dec 1919.

[23] I. Langmuir. The mechanism of the surface phenomena of flotation. *Trans. Faraday Soc.*, 15:62–74, 1920.

[24] W.B. Hardy and I Doubleday. Boundary lubrication. the paraffin series. *Proceedings of the Royal Society of London Series A*, 100(707):550–574, mar 1922.

[25] C.M. Allen and E. Drauglis. Boundary layer lubrication: monolayer or multilayer. *Wear*, 14(5):363–384, 1969.

[26] R. F.G. Apòstolo, G. Tsagkaropoulou, and P. J. Camp. Molecular adsorption, self-assembly, and friction in lubricants. *Journal of Molecular Liquids*, 277:606–612, 2019.

[27] V Anghel, P M Cann, and H A Spikes. Direct measurement of boundary lubricating films. In D. Dowson, C.M. Taylor, T.H.C. Childs, G. Dalmaz, Y. Berthier, L. Flamand, J.-M. Georges, and A.A. Lubrecht, editors, *Elastohydrodynamics - '96 Fundamentals and Applications in Lubrication and Traction*, volume 32 of *Tribology Series*, pages 459–466. Elsevier, 1997.

[28] B. M. Fry, G. Moody, H. A. Spikes, and J. S. S. Wong. Adsorption of organic friction modifier additives. *Langmuir*, 36(5):1147–1155, 2020. PMID: 31941274.

[29] M T. L. Casford and P. B. Davies. The structure of oleamide films at the aluminum/oil interface and aluminum/air interface studied by sum frequency generation (sfg) vibrational spectroscopy and reflection absorption infrared spectroscopy (rairs). *ACS Applied Materials & Interfaces*, 1(8):1672–1681, 2009. PMID: 20355782.

[30] R. Simič and M. Kalin. Adsorption mechanisms for fatty acids on dlc and steel studied by afm and tribological experiments. *Applied Surface Science*, 283:460–470, 2013.

[31] M. S. Lim, K. Feng, X. Chen, N. Wu, A. Raman, J. Nightingale, E. S. Gawalt, D. Korakakis, L. A. Hornak, and A. T. Timperman. Adsorption and desorption of stearic acid self-assembled monolayers on aluminum oxide. *Langmuir*, 23(5):2444–2452, 2007. PMID: 17261036.

[32] FP Bowden, JN Gregory, and D Tabor. Lubrication of metal surfaces by fatty acids. *Nature*, 156(3952):97–101, 1945.

[33] Mary H Wood, MT Casford, R Steitz, A Zarbakhsh, RJL Welbourn, and Stuart M Clarke. Comparative adsorption of saturated and unsaturated fatty acids at the iron oxide/oil interface. *Langmuir*, 32(2):534–540, 2016.

[34] S Loehlé, C Matta, C Minfray, T.Le Mogne, R Iovine, Y Obara, A Miyamoto, and J M Martin. Mixed lubrication of steel by c18 fatty acids revisited. part i: Toward the formation of carboxylate. *Tribology International*, 82:218–227, 2015.

[35] JJ Frewing. The influence of temperature on boundary lubrication. *Proceedings of the Royal Society of London. Series A. Mathematical and Physical Sciences*, 181(984):23–42, 1942.

[36] H. Koshima, H. Kamano, Y. Hisaeda, H. Liu, and S. Ye. Analyses of the adsorption structures of friction modifiers by means of quantitative structure-property relationship method and sum frequency generation spectroscopy. *Tribology Online*, 5(3):165–172, 2010.

[37] N.S. Villa, G. Serra, L. Bonoldi, G. Assanelli, M. Notari, A. Lucotti, and M. Tommasini. Combining micro-infrared reflection absorption spectroscopy with density functional theory for investigating the adsorption of organic friction modifiers on steel surfaces. *Vibrational Spectroscopy*, 121:103403, 2022.

[38] A. H Kycia, K. Koczkur, J. J. Leitch, J. Lipkowski, V. Zamlynny, and M.W.P. Petryk. Application of pm-irras to study thin films on industrial and environmental samples. *Analytical and bioanalytical chemistry*, 405:1537–1546, 2013.

[39] D Blaudez, T Buffeteau, JC Cornut, B Desbat, N Escafre, M Pezolet, and JM Turlet. Polarization-modulated ft-ir spectroscopy of a spread monolayer at the air/water interface. *Applied spectroscopy*, 47(7):869–874, 1993.

[40] Julie Gèan, Thierry Buffeteau, B Desbat, and Daniel Blaudez. Increasing detectivity of polarization modulation infrared reflection-absorption spectroscopy for the study of ultrathin films deposited on various substrates. *Applied spectroscopy*, 57:1260–5, 11 2003.

[41] Daniel Blaudez, Jean-Marie Turlet, Jean Dufourcq, Delphine Bard, Thierry Buffeteau, and Bernard Desbat. Investigations at the air/water interface using polarization modulation ir spectroscopy. *Journal of the Chemical Society, Faraday Transactions*, 92(4):525–530, 1996.

[42] Robert G Greenler. Infrared study of adsorbed molecules on metal surfaces by reflection techniques. *The Journal of Chemical Physics*, 44(1):310–315, 1966.

[43] Yijun Gu, Zheming Shi, and Chong-Shi Nie. Infrared transmission and reflection absorption spectroscopy study on molecular orientation of long-chain n-alkane amide and 2-n-alkylimidazole multilayers on silver and krs-5 surfaces. *Applied spectroscopy*, 52(6):855–862, 1998.

[44] PM Cann and HA Spikes. In-contact ir spectroscopy of hydrocarbon lubricants. *Tribology Letters*, 19:289–297, 2005.

[45] David Himmel, JL Mansot, Y Bercion, and AA Lubrecht. In situ raman microspectrometry of lubricated tribologic contacts. part two: Simultaneous measurements of pressure, lubricant film thickness and temperature distributions in a running ehd contact. *Tribology letters*, 41:131–144, 2011.

[46] Manimunda Praveena, Kaustav Guha, Abhilash Ravishankar, Sanjay K Biswas, Colin D Bain, and Vikram Jayaram. Total internal reflection raman spectroscopy of poly (alpha-olefin) oils in a lubricated contact. *Rsc Advances*, 4(42):22205–22213, 2014.

[47] Kun Zhang, Zongwei Xu, Andreas Rosenkranz, Ying Song, Tao Xue, and Fengzhou Fang. Surface-and tip-enhanced raman scattering in tribology and lubricant detection–a prospective. *Lubricants*, 7(9):81, 2019.

[48] Wenhsi Chua and Gwidon W Stachowiak. The growth of thin lubricating films of plant oils. *Tribology letters*, 41:451–462, 2011.

[49] Li Shenghua, Yang He, and Jin Yuansheng. Lubrication chemistry viewed from dft-based concepts and electronic structural principles. *International Journal of Molecular Sciences*, 5(1):13–34, 2003.

[50] JP Ewen, DM Heyes, and Daniele Dini. Advances in nonequilibrium molecular dynamics simulations of lubricants and additives. *Friction*, 6:349–386, 2018.

[51] James P Ewen, Sebastián Echeverri Restrepo, Neal Morgan, and Daniele Dini. Nonequilibrium molecular dynamics simulations of stearic acid adsorbed on iron surfaces with nanoscale roughness. *Tribology International*, 107:264–273, 2017.

[52] James P Ewen, Chiara Gattinoni, Neal Morgan, Hugh A Spikes, and Daniele Dini. Nonequilibrium molecular dynamics simulations of organic friction modifiers adsorbed on iron oxide surfaces. *Langmuir*, 32(18):4450–4463, 2016.

[53] Joshua L Bradley-Shaw, Philip J Camp, Peter J Dowding, and Ken Lewtas. Molecular dynamics simulations of glycerol monooleate confined between mica surfaces. *Langmuir*, 32(31):7707–7718, 2016.

[54] Aditya Jaishankar, Arben Jusufi, Jessica L Vreeland, Shane Deighton, Joseph Pellettiere, and Alan M Schilowitz. Adsorption of stearic acid at the iron oxide/oil interface: theory, experiments, and modeling. *Langmuir*, 35(6):2033–2046, 2019.

[55] Michael Doig, Chris P Warrens, and Philip J Camp. Structure and friction of stearic acid and oleic acid films adsorbed on iron oxide surfaces in squalane. *Langmuir*, 30(1):186–195, 2014.

[56] Xuan Zheng, Hongtao Zhu, Buyung Kosasih, and A Kiet Tieu. A molecular dynamics simulation of boundary lubrication: The effect of n-alkanes chain length and normal load. *Wear*, 301(1-2):62–69, 2013.

[57] James P Ewen, Chiara Gattinoni, Foram M Thakkar, Neal Morgan, Hugh A Spikes, and Daniele Dini. A comparison of classical force-fields for molecular dynamics simulations of lubricants. *Materials*, 9(8):651, 2016.

[58] A. C. T. van Duin, S. Dasgupta, F. Lorant, and W. A. Goddard. Reaxff: A reactive force field for hydrocarbons. *The Journal of Physical Chemistry A*, 105(41):9396–9409, 2001.

[59] S. Loehle. Understanding of adsorption mechanism and tribological behaviors of c18 fatty acids on iron-based surfaces : a molecular simulation approach. 02 2014.

[60] S. Loehle, C. Matta, C. Minfray, T. Le-Mogne, R. Iovine, Y. Obara, A. Miyamoto, and J. Martin. Mixed lubrication of steel by c18 fatty acids revisited part ii: Influence of some key parameters. *Tribology International*, 94, 08 2015.

[61] C. Gattinoni, J. P. Ewen, and D. Dini. Adsorption of surfactants on α-fe$_2$o$_3$(0001): A density functional theory study. *The Journal of Physical Chemistry C*, 122(36):20817–20826, 2018.

[62] G. Socrates. *Infrared and Raman Characteristic Group Frequencies: Tables and Charts*. Wiley, 2004.

[63] Yuemin Wang and Christof Wöll. Ir spectroscopic investigations of chemical and photochemical reactions on metal oxides: bridging the materials gap. *Chemical Society Reviews*, 46(7):1875–1932, 2017.

[64] R. Dovesi, A. Erba, R. Orlando, C. M. Zicovich-Wilson, B. Civalleri, L. Maschio, M. Rérat, S. Casassa, J. Baima, S. Salustro, and B. Kirtman. Quantum-mechanical condensed matter simulations with crystal. *WIREs Computational Molecular Science*, 8(4):e1360, 2018.

[65] A. D. Becke. Density-functional exchange-energy approximation with correct asymptotic behavior. *Phys. Rev. A*, 38:3098–3100, Sep 1988.

[66] C. Lee, W. Yang, and R. G. Parr. Development of the colle-salvetti correlation-energy formula into a functional of the electron density. *Phys. Rev. B*, 37:785–789, Jan 1988.

[67] S. H. Vosko, L. Wilk, and M. Nusair. Accurate spin-dependent electron liquid correlation energies for local spin density calculations: a critical analysis. *Canadian Journal of Physics*, 58(8):1200–1211, 1980.

[68] D. Vilela Oliveira, J. Laun, M. F. Peintinger, and T. Bredow. Bsse-correction scheme for consistent gaussian basis sets of double- and triple-zeta valence with polarization quality for solid-state calculations. *Journal of Computational Chemistry*, 40(27):2364–2376, 2019.

[69] S. Grimme, J. Antony, S. Ehrlich, and H. Krieg. A consistent and accurate ab initio parametrization of density functional dispersion correction (dft-d) for the 94 elements h-pu. *The Journal of Chemical Physics*, 132(15):154104, 2010.

[70] S. Grimme, S. Ehrlich, and L. Goerigk. Effect of the damping function in dispersion corrected density functional theory. *Journal of Computational Chemistry*, 32(7):1456–1465, 2011.

[71] S. Grimme, A. Hansen, J. G. Brandenburg, and C. Bannwarth. Dispersion-corrected mean-field electronic structure methods. *Chemical Reviews*, 116(9):5105–5154, 2016. PMID: 27077966.

[72] S. Rayne and K. Forest. Theoretical studies on the pka values of perfluoroalkyl carboxylic acids. *Journal of Molecular Structure: THEOCHEM*, 949(1):60–69, 2010.

[73] L. Schöttner, R. Ovcharenko, A. Nefedov, E. Voloshina, Y. Wang, J. Sauer, and C. Wöll. Interaction of water molecules with the α-fe$_2$o$_3$(0001) surface: A combined experimental and computational study. *The Journal of Physical Chemistry C*, 123(13):8324–8335, 2019.

[74] G. S. Parkinson. Iron oxide surfaces. *Surface Science Reports*, 71(1):272–365, 2016.

[75] D. Dwivedi, K Lepková, and T. Becker. Carbon steel corrosion: a review of key surface properties and characterization methods. *RSC Adv.*, 7:4580–4610, 2017.

[76] G. J. Martin, R. S. Cutting, D. J. Vaughan, and M. C. Warren. Bulk and key surface structures of hematite, magnetite, and goethite: A density functional theory study. *American Mineralogist*, 94(10):1341–1350, 2009.

[77] M. Ferrero, M. Rérat, B Kirtman, and R Dovesi. Calculation of first and second static hyperpolarizabilities of one- to three-dimensional periodic compounds. implementation in the crystal code. *The Journal of Chemical Physics*, 129(24):244110, 2008.

[78] M. Ferrero, M. Rérat, R. Orlando, and R. Dovesi. Coupled perturbed hartree-fock for periodic systems: The role of symmetry and related computational aspects. *The Journal of Chemical Physics*, 128(1):014110, 2008.

[79] M. Ferrero, M. Rérat, R. Orlando, and R. Dovesi. The calculation of static polarizabilities of 1-3d periodic compounds. the implementation in the crystal code. *Journal of Computational Chemistry*, 29(9):1450–1459, 2008.

[80] C. M. Zicovich-Wilson, F. Pascale, C. Roetti, V. R. Saunders, R. Orlando, and R. Dovesi. Calculation of the vibration frequencies of α-quartz: The effect of hamiltonian and basis set. *Journal of Computational Chemistry*, 25(15):1873–1881, 2004.

[81] F. Pascale, C. M. Zicovich-Wilson, F. López Gejo, B. Civalleri, R. Orlando, and R. Dovesi. The calculation of the vibrational frequencies of crystalline compounds and its implementation in the crystal code. *Journal of Computational Chemistry*, 25(6):888–897, 2004.

[82] L. Maschio, B. Kirtman, R. Orlando, and M. Rérat. Ab initio analytical infrared intensities for periodic systems through a coupled perturbed hartree-fock/kohn-sham method. *The Journal of Chemical Physics*, 137(20):204113, 2012.

[83] J. Hutter, M. Iannuzzi, F. Schiffmann, and J. VandeVondele. cp2k: atomistic simulations of condensed matter systems. *WIREs Computational Molecular Science*, 4(1):15–25, 2014.

[84] J. VandeVondele, M. Krack, F. Mohamed, M. Parrinello, T. Chassaing, and J. Hutter. Quickstep: Fast and accurate density functional calculations using a mixed gaussian and plane waves approach. *Computer Physics Communications*, 167(2):103–128, 2005.

[85] T. D. Kühne, M. Iannuzzi, M. Del Ben, V. V. Rybkin, P. Seewald, F. Stein, T. Laino, R. Z. Khaliullin, O. Schütt, F. Schiffmann, D. Golze, J. Wilhelm, S. Chulkov, M. H. Bani-Hashemian, V. Weber, U. Borštnik, M. Taillefumier, A. S. Jakobovits, A. Lazzaro, H. Pabst, T. Müller, R. Schade, M. Guidon, S. Andermatt, N. Holmberg, G. K. Schenter, A. Hehn, A. Bussy, F. Belleflamme, G. Tabacchi, A. Glöß, M. Lass, I. Bethune, C. J. Mundy, C. Plessl, M. Watkins, J. VandeVondele, M. Krack, and J. Hutter. Cp2k: An electronic structure and molecular dynamics software package - quickstep: Efficient and accurate electronic structure calculations. *The Journal of Chemical Physics*, 152(19):194103, 2020.

[86] S. Goedecker, M. Teter, and J. Hutter. Separable dual-space gaussian pseudopotentials. *Phys. Rev. B*, 54:1703–1710, Jul 1996.

[87] M Guidon, J. Hutter, and J. VandeVondele. Auxiliary density matrix methods for hartree-fock exchange calculations. *Journal of Chemical Theory and Computation*, 6(8):2348–2364, 2010. PMID: 26613491.

[88] S. L. Dudarev, G. A. Botton, S. Y. Savrasov, C. J. Humphreys, and A. P. Sutton. Electron-energy-loss spectra and the structural stability of nickel oxide: An lsda+u study. *Phys. Rev. B*, 57:1505–1509, Jan 1998.

[89] Giovanni Bussi, Davide Donadio, and Michele Parrinello. Canonical sampling through velocity rescaling. *The Journal of chemical physics*, 126(1):014101, 2007.

[90] D. R. Galimberti, A. Milani, M. Tommasini, C. Castiglioni, and M. P. Gaigeot. Combining static and dynamical approaches for infrared spectra calculations of gas phase molecules and clusters. *Journal of Chemical Theory and Computation*, 13(8):3802–3813, 2017.

Bibliography

[91] R. D. King-Smith and David Vanderbilt. Theory of polarization of crystalline solids. *Phys. Rev. B*, 47:1651–1654, Jan 1993.

[92] D. Vanderbilt and R. D. King-Smith. Electric polarization as a bulk quantity and its relation to surface charge. *Phys. Rev. B*, 48:4442–4455, Aug 1993.

[93] Daria Ruth Galimberti. Vibrational circular dichroism from dft molecular dynamics: The awv method. *Journal of Chemical Theory and Computation*, 18(10):6217–6230, 2022.

[94] A. P. Thompson, H. M. Aktulga, R. Berger, D. S. Bolintineanu, W. M. Brown, P. S. Crozier, P. J. in 't Veld, A. Kohlmeyer, S. G. Moore, T. D. Nguyen, R. Shan, M. J. Stevens, J. Tranchida, C. Trott, and S. J. Plimpton. Lammps - a flexible simulation tool for particle-based materials modeling at the atomic, meso, and continuum scales. *Comp. Phys. Comm.*, 271:108171, 2022.

[95] S. W. I. Siu, K. Pluhackova, and R. A. Böckmann. Optimization of the opls-aa force field for long hydrocarbons. *Journal of Chemical Theory and Computation*, 8(4):1459–1470, 2012. PMID: 26596756.

[96] W. L. Jorgensen, D. S. Maxwell, and J. Tirado-Rives. Development and testing of the opls all-atom force field on conformational energetics and properties of organic liquids. *Journal of the American Chemical Society*, 118(45):11225–11236, 1996.

[97] J. P. Ewen, C. Gattinoni, F. M. Thakkar, N. Morgan, H. A. Spikes, and D. Dini. A comparison of classical force-fields for molecular dynamics simulations of lubricants. *Materials*, 9(8), 2016.

[98] E. B. Tadmor, R. S. Elliott, J. P. Sethna, R. E. Miller, and C. A. Becker. The potential of atomistic simulations and the knowledgebase of interatomic models. *JOM*, 63(7):17, 2011.

[99] Jukka Vaari. Molecular dynamics simulations of vacancy diffusion in chromium (iii) oxide, hematite, magnetite and chromite. *Solid State Ionics*, 270:10–17, 2015.

[100] E.L. Pollock and Jim Glosli. Comments on p3m, fmm, and the ewald method for large periodic coulombic systems. *Computer Physics Communications*, 95(2):93–110, 1996.

[101] R. W. Hockney and J. W. Eastwood. *Computer simulation using particles*. Bristol: Hilger, 1988, 1988.

[102] W. Humphrey, A. Dalke, and K. Schulten. Vmd - visual molecular dynamics. *Journal of Molecular Graphics*, 14:33–38, 1996.

[103] D. R. Galimberti and J. Sauer. Chemically accurate vibrational free energies of adsorption from density functional theory molecular dynamics: Alkanes in zeolites. *Journal of Chemical Theory and Computation*, 17(9):5849–5862, 2021. PMID: 34459582.

[104] Douglas Poland. Statistical mechanics, 1977.

[105] Jonas Amsler, Philipp N. Plessow, Felix Studt, and Tomáčš Bučko. Anharmonic correction to adsorption free energy from dft-based md using thermodynamic integration. *Journal of Chemical Theory and Computation*, 17(2):1155–1169, 2021. PMID: 33482059.

[106] N. B. Colthup, L. H. Daly, and S. E. Wiberley. *Introduction to Infrared and Raman Spectroscopy (Second Edition)*. Academic Press, second edition edition, 1975.

[107] K. Nakamoto. *Applications in Coordination Chemistry*, chapter 1, pages 1–273. John Wiley & Sons, Ltd, 2008.

[108] S. Mishra, D. Chaturvedi, N. Kumar, P. Tandon, and H.W. Siesler. An ab initio and dft study of structure and vibrational spectra of γ form of oleic acid: Comparison to experimental data. *Chemistry and Physics of Lipids*, 163(2):207–217, 2010.

[109] Johan Guegan, Mark Southby, and Hugh Spikes. Friction modifier additives, synergies and antagonisms. *Tribology Letters*, 67, 06 2019.

[110] J. E. Crowell, J. G. Chen, and J. T. Yates. A vibrational study of the adsorption and decomposition of formic acid and surface formate on al(111). *The Journal of Chemical Physics*, 85(5):3111–3122, 1986.

[111] C-OA Olsson and Dieter Landolt. Passive films on stainless steels-chemistry, structure and growth. *Electrochimica acta*, 48(9):1093–1104, 2003.

[112] Carlos Ayestarán Latorre, James P Ewen, Chiara Gattinoni, and Daniele Dini. Simulating surfactant–iron oxide interfaces: from density functional theory to molecular dynamics. *The Journal of Physical Chemistry B*, 123(31):6870–6881, 2019.

[113] Kerstin Falk, Thomas Reichenbach, Konstantinos Gkagkas, Michael Moseler, and Gianpietro Moras. Relating dry friction to interdigitation of surface passivation species: A molecular dynamics study on amorphous carbon. *Materials*, 15(9), 2022.